TÉCNICO LISBOA

Impact of Quark-Gluon Plasma in Extensive Air Showers

Beatriz Franco Faustino Artur

Thesis to obtain the Master of Science Degree in

Engineering Physics

Supervisor(s): Prof. Ruben Maurício da Silva Conceição
Prof. Liliana Marisa Cunha Apolinário

Examination Committee

Chairperson: Prof. Mário João Martins Pimenta
Supervisor: Prof. Ruben Maurício da Silva Conceição
Member of the Committee: Prof. Pedro Jorge Dos Santos de Assis

December 2022

Acknowledgments

I start by thanking both of my supervisors, Dr. Ruben Conceição and Dr. Liliana Apolinário, for their guidance, the insightful discussions and the advice given along the development of this dissertation. Thank you for trusting me with this project and for believing in my work.

I would also like to thank Dr. Tanguy Pierog for providing the CONEX code with the EPOS-QGP version, which has been extensively used to produce the results found in this thesis.

Finally, I would like to thank my family for the support they gave me along the way and for allowing me to pursue my studies. Finally, I thank all of my colleagues at LIP for the companionship and all the fruitful discussions.

Resumo

Os raios cósmicos de ultra-alta energia interagem com a atmosfera terrestre produzindo cascatas atmosféricas de alta energia, cujos valores não são atingíveis nos aceleradores atuais, como no Large Hadron Collider (LHC). O número de muões na superfície da Terra é um observável essencial para inferir a composição dos raios cósmicos. No entanto, os dados que têm sido recolhidos ao longo dos anos mostram que os modelos de interações hadrónicas utilizados para simular cascatas atmosféricas produzem um número de muões inferior àquele que se observa nas medidas experimentais. Este déficit é conhecido como o *Puzzle Muónico* e a sua origem deveria ser observável nas colisões de alta energia no LHC. De facto, experiências recentes de iões pesados revelaram a existência de um novo estado de matéria: o plasma de quarks e gluões, o qual tem sido estudado através de modelos de interações hadrónicas como o EPOS-LHC. Contudo, este revelou-se insuficiente e foi por isso modificado para explicar fenomenologicamente o déficit de muões observado, originando o modelo EPOS-QGP. O principal objetivo desta dissertação é estudar este novo modelo de forma a avaliar se o plasma de quarks e gluões consegue explicar tanto os dados obtidos no LHC como os dados provenientes dos raios cósmicos de ultra-alta energia.

Palavras-chave: Raios Cósmicos de Ultra-Alta Energia, Cascatas Atmosféricas, Puzzle Muónico, Plasma de Quarks e Gluões, EPOS-QGP

Abstract

Ultra-High Energy Cosmic Rays (UHECRs) interact with the Earth's atmosphere producing *Extensive Air Showers* (EAS) at very high energies, which are not accessible at the Large Hadron Collider (LHC). The number of muons at the ground is a key observable to infer the mass composition of cosmic rays. But the data that has been collected along the years shows that the hadronic interaction models used to simulate EAS produce a muon deficit in regard to the experimental measurements. This is known as the *Muon Puzzle* and its source should be observable in high-energy collisions at the LHC. Incidentally, recent experiments with heavy-ions at the LHC have unraveled a new state of matter, called *Quark-Gluon Plasma*, which has been studied through models like the EPOS-LHC. However, this model was insufficient and so it was modified in order to phenomenologically explain the muon deficit that had been observed, originating the *EPOS-QGP*. The goal of this dissertation is to use this new model to assess if quark-gluon plasma can explain the measurements performed at the LHC and on UHECRs.

Keywords: Ultra-High Energy Cosmic Rays, Extensive Air Showers, Muon Puzzle, Quark-Gluon Plasma, EPOS-QGP

Contents

List of Tables

List of Figures

List of Abbreviations

A − A nucleus-nucleus

ALICE A Large Ion Collider Experiment (at LHC)

AMIGA Auger Muons and Infill for the Ground Array

AMS Alpha Magnetic Spectrometer

ATLAS A Toroidal LHC Apparatus (at LHC)

Au Gold (Chemical Element)

CERN European Organization for Nuclear Research

CMS Compact Muon Solenoid (at LHC)

CORSIKA COsmic Ray SImulations for KAscade

CREAM Cosmic Ray Energetics And Mass

EAS Extensive Air Shower

EAS − MU Extensive Air Shower - Moscow State University

EPOS Energy conserving quantum mechanical multiple scattering approach, based on Partons, Off-shell remnants and Splitting of partons ladders

He Helium (Chemical Element)

HiRES High Resolution Fly's Eye

KASCADE KArlsruhe Shower Core and Array DEtector

LHC Large Hadron Collider (at CERN)

LHCb Large Hadron Collider beauty (at CERN)

MIA Michigan Muon Array

NEVOD − DECOR Neutrino Water Detector on the Earth's Surface - Coordinate Detector

O Oxygen (Chemical Element)

$\mathbf{p-A}$ proton-nucleus

$\mathbf{p_T}$ Transverse Momentum

$\mathbf{Pb}$ Lead (Chemical Element)

PHENIX Pioneering High Energy Nuclear Interaction eXperiment (at RHIC)

pp proton-proton

QCD Quantum Chromodynamics

QGP Quark-Gluon Plasma

QGSJET Quark-Gluon String model with JETs

RHIC Relativistic Heavy Ion Collider

STAR Solenoidal Tracker (at RHIC)

SUGAR Sydney University Giant Air-shower Recorder

UHECR Ultra-High Energy Cosmic Ray

USP Universal Shower Profile

WHISP Working group on Hadronic Interactions and Shower Physics

Xe Xenon (Chemical Element)

Chapter 1

Introduction

Particles with energies greater than 10^{18} eV known as Ultra-High Energy Cosmic Rays (UHECRs) are constantly reaching the Earth, interacting with its atmospheric particles and producing Extensive Air Showers (EAS). One of the main products of these interactions that reach the surface of the Earth are muons, which can be used to infer the mass composition of cosmic rays and study the hadronic interactions in the air showers. However, for some time now, when the experimental measurements are compared with the predictions from hadronic interaction models, such as the EPOS-LHC, one observes that the different models consistently predict a lower number of muons. This is known as the Muon Puzzle, which has been studied for many years. Finally, the conclusion was that its origin should be observable at the LHC, since it already shows itself for energies reachable by this experiment [1]. This is a very interesting observation, since there is a new state of matter that has been detected at the LHC: the Quark-Gluon Plasma (QGP). We know this plasma forms in heavy-ion collisions for dense-dense systems, such as Pb-Pb, since all of its more visible experimental signatures have been observed for such systems. However, the possible formation of QGP in smaller systems, such as in p-Pb or even pp is still an open question.

Hence, the question arises: how do these two phenomena relate to each other? Can the quark-gluon plasma help solve the Muon Puzzle? In fact, one of the most visible experimental signatures of the quark-gluon plasma is baryon and strangeness enhancement. According to the physics of the shower cascades, this would lead to an increase in the number of muons produced along the shower. Thus, if a QGP medium was formed along the extensive air showers of UHECRs, the Muon Puzzle could be potentially solved. To test this hypothesis, a new hadronic interaction model was developed: the EPOS-QGP, which is supposed to account for more QGP effects than its predecessors [2]. The main goal of this dissertation is to assess the behaviour of this model and to observe how it affects the development of the shower cascade, in order to see if it is successful in the creation of a QGP medium compatible with a healthy shower development.

Therefore, this dissertation is divided in several chapters. Chapters 2 through 4 constitute a theoretical introduction to the work developed in this dissertation. Chapter 2 introduces the reader to the ultra-high energy cosmic rays and their extensive air showers, explaining the physics behind them and

describing the most important air shower observables that were also studied in this work. It ends with an overview of the Muon Puzzle, presenting the most recent results on the matter. Chapter 3 deals with the other half of the theoretical framework: the quark-gluon plasma. It starts by defining and describing the process of formation of this state of matter, relating it to the centrality of heavy-ion collisions, and presenting its more visible experimental signatures. It ends with a brief explanation of the connection between the Muon Puzzle introduced in the previous chapter and this new state of matter. Chapter 4 follows with an introduction to the different hadronic interaction models used in conjunction with the air shower simulators, with an emphasis on EPOS-LHC and its modified version EPOS-QGP. Chapters 5 and 6 present the results of the simulations performed for this dissertation in order to assess the impact of the model EPOS-QGP. The former deals with the first interaction, characterizing it and its products, and studies its behaviour in the center-of-mass frame. The later presents the results for the air shower observables, comparing them to the existing measurements. Finally, Chapter 7 presents the final remarks and a summary of the conclusions achieved in this dissertation.

Chapter 2

Theoretical Overview of Cosmic Rays

2.1 UHECRs

The Earth is continuously bombarded by fully-ionised nuclei with relativistic kinetic energies, which are known as Cosmic Rays (CRs). The mass composition of these particles ranges from proton to iron, with a negligible fraction of heavier nuclei, while their energy can range from less than 1 GeV up to a few 10^{20} eV. They are labelled Ultra High-Energy (UHE) when their energy is greater than 10^{18} eV. The energy spectrum of cosmic rays follows a power law $dN/dE \propto E^{\gamma}$, where γ is the spectral index, and it is rather featureless [3]. In order to emphasize the deviations from the overall power-law, Figure 2.1 shows a compilation of measurements of the cosmic ray energy flux scaled by $E^{2.5}$. The break at $E \approx 3 \times 10^{15}$ eV is known as the *knee* and the energy range $10^{18} - 10^{19}$ eV, which corresponds to a hardening of the spectrum, is known as the *ankle*. Above 7×10^{19} eV the flux is suppressed [4].

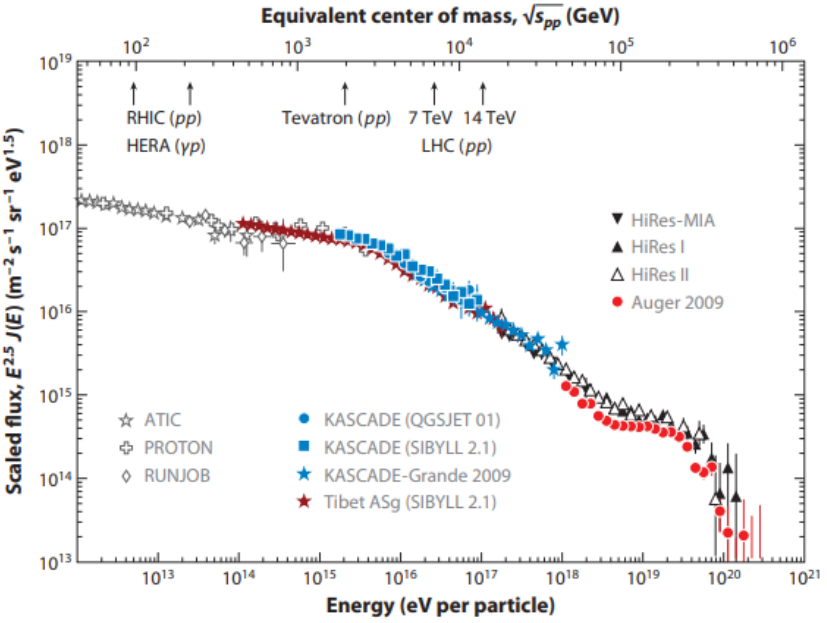

Figure 2.1: Compilation of measurements of the cosmic-ray energy flux scaled by $E^{2.5}$. Taken from [4].

When cosmic rays propagate through the Universe, they interact with galactic and extra-galactic magnetic fields which bend their trajectories, making their arrival directions at Earth essentially random. This means that, although cosmic rays are likely produced in well-identifiable point-sources, we have a hard time identifying them. It is known that cosmic rays with energies up to 10^{18} eV are produced by shock acceleration in super-nova remnants [5, 6] and the primary mass composition is light and tends to get heavier towards intermediate mass states with increasing energy [7]. However, the extra-galactic origin of UHECRs is still an open question in astroparticle physics [8].

While cosmic rays with energies up to 10^{14} eV can be directly observed using space-based experiments, like AMS-02 [9], and high-altitude balloons like CREAM [10], for higher energies, their flux drops below one particle per square meter per year [4] and we can only observe them indirectly through ground-based experiments with huge apertures, like the Pierre Auger Observatory [11] and the Telescope Array [12]. In fact, when UHECRs reach the Earth's atmosphere and interact with air nuclei, they produce hundreds to thousands of particles, which themselves interact, triggering macroscopic cascades of secondary particles, known as Extensive Air Showers (EAS). These can be observed in the ground-based experiments through the measurement of fluorescence light emitted by air molecules and through particle detection in scintillators or water-Cherenkov tanks. Energy and composition information must be derived indirectly by simulating these cascades of secondary particles that cosmic rays produce in the atmosphere and comparing the predictions with measurements. Hence, these air shower simulations are essential in the interpretation of cosmic-ray data.

2.2 Extensive Air Showers

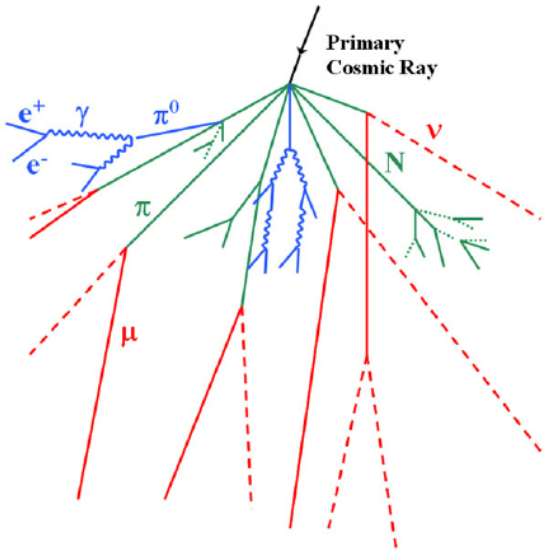

Figure 2.2: Schematics of an extensive air shower with its components: the electromagnetic in blue and the hadronic in green. The produced muons are shown in red. Taken from [13].

When a hadronic high-energy particle enters the Earth's atmosphere, it interacts with a nucleus from the air (mainly nitrogen, oxygen and argon) at a typical height of 15 to 35 km above sea level, producing

a shower of secondary particles that can be separated in two different components: electromagnetic and hadronic (see Figure 2.2). The electromagnetic component is mostly due to the immediate decay of neutral pions into photons ($\pi^0 \rightarrow \gamma\gamma$) and then develops independently via electron pair-production and bremsstrahlung. The hadronic core is composed by the long-lived secondary hadrons, such as baryons, charged pions and kaons. Although a small fraction of muons is produced electromagnetically by direct pair-production, 90% of the muons come from the hadronic cascade, due to the decay of pions and kaons. Muons propagate through the atmosphere with small energy losses, reaching the surface of the Earth. Incidentally, in showers with high zenith angles, typically greater than $60°$, these muons and the electromagnetic particles produced in their decay are the only particles that can be observed at the ground. Note that the neutrinos from muonic decay are very unlikely to re-interact, making their energy undetectable.

2.2.1 Heitler Model

The electromagnetic component carries more than 90% of the shower energy [14]. Its two dominant processes are, as already mentioned, $e^{\pm}$ pair-production by photons and bremsstrahlung by $e^{\pm}$. The basic features of the shower can be understood within a simplified analytical model: the Heitler model [15]. In this model (see Figure 2.3 (left)), the cascade starts with only one particle of energy E_0, which interacts after having traversed a depth $d = \lambda \ln(2)$ (where λ is its mean interaction length), originating two new particles with energy $E_0/2$ each. These particles will themselves interact and produce two more particles each, such that at a given depth $X = n \times d$, where n is the number of generations (consecutive interactions), there are 2^n particles with energy $E_0/2^n$ each. This particle-doubling process continues until the particles reach a critical energy E_c, when the ionization energy losses equal the radiative losses. This means that the shower has a maximum where the number of particles is

$$N_{\max} = 2^{n_{max}} = \frac{E_0}{E_c} \tag{2.1}$$

and its corresponding traversed column density is

$$X_{\max}(E_0) = n_{max} d = \frac{\ln(N_{max})}{\ln(2)} \lambda \ln(2) = \lambda \ln\left(\frac{E_0}{E_c}\right). \tag{2.2}$$

2.2.2 Heitler-Matthews Model

The Heitler model was generalized to a hadron induced shower by J. Matthews [16]. In this so called Heitler-Matthews model (see Figure 2.3 (right)), the shower is approximated by a pure pion shower. This means that, after having travelled a depth corresponding to the mean interaction length λ_{int}, the initial hadron with energy E_0 produces N_π pions with energy E_0/N_π each. One-third of these particles are neutral pions, which decay immediately into photons, yielding electromagnetic subshowers, and two-thirds are charged pions $N_{\pi^\pm}$, the only ones that feed the hadronic cascade. Each interaction produces a fixed number of pions N_π, allowing for a total of $(N_\pi)^n$ pions with energy $E_0/(N_\pi)^n$ at level n. The cascade ends when the charged particles reach a critical energy $E_{c\pi}$, i.e. when the decay probability

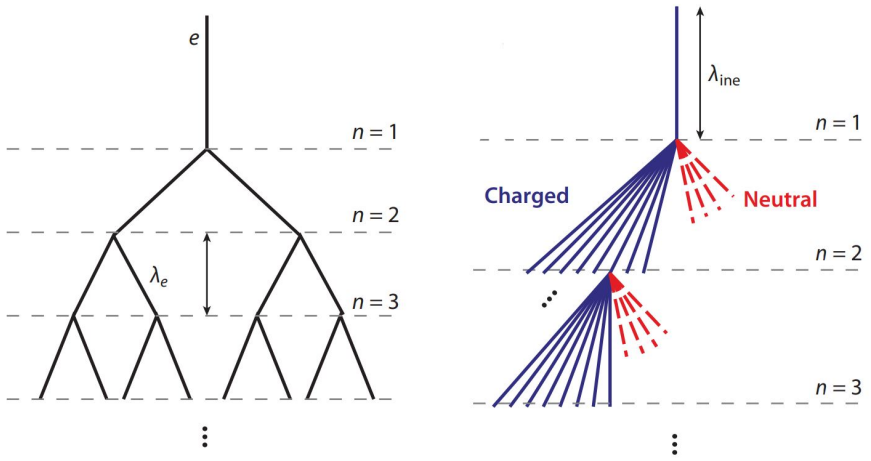

Figure 2.3: **Left**: Simplified electromagnetic cascade, according to the Heitler Model. The parameters n and d represent the generations and the transversed slant depth, respectively. **Right**: Simplified hadronic cascade, according to the Heitler-Mathews Model. The parameter n represents the generations and λ_{int} the mean interaction length. Charged pions are represented in full lines, while neutral ones are in dashed lines. Both figures taken from [4].

equals the interaction probability, and starts to decay into muons. Thus, the number of muons in a shower N_μ is directly related to the number of charged pions in the critical generation n_c:

$$E_{c\pi} = \frac{E_0}{(N_\pi)^{n_c}} \iff n_c = \frac{\ln\left(E_0/E_{c\pi}\right)}{\ln(N_\pi)}, \tag{2.3}$$

$$N_\mu = (N_{\pi^\pm})^{n_c} \iff \ln(N_\mu) = \frac{\ln\left(E_0/E_{c\pi}\right)}{\ln(N_\pi)} \ln\left(N_{\pi^\pm}\right) \iff N_\mu = \left(\frac{E_0}{E_{c\pi}}\right)^\beta, \tag{2.4}$$

where $\beta = \ln(N_{\pi^\pm})/\ln(N_\pi)$, assuming that muons themselves do not decay. The depth of the shower maximum $X_{\max}$ is determined by the electromagnetic subshowers produced in the first hadronic interactions:

$$X_{\max}(E_0) = \lambda_{int} + \lambda \ln\left(\frac{E_0}{N_\pi E_c}\right). \tag{2.5}$$

Furthermore, considering that the binding energy per nucleon is much smaller than the typical interaction energies, the above results can be generalized to a primary of mass A, which, by the superposition model, can be thought of as A independent nucleons with energy E_0/A each, yielding the following results:

$$N_\mu = A\left(\frac{E_0}{AE_{c\pi}}\right)^\beta = A^{1-\beta}\left(\frac{E_0}{E_{c\pi}}\right)^\beta, \tag{2.6}$$

$$X_{\max}(E_0) = \lambda_{int} + \lambda \ln\left(\frac{E_0}{AN_\pi E_c}\right). \tag{2.7}$$

This means that the heavier the shower-initiating hadron, the more muons are expected for a given primary energy and the shallower the depth of the shower maximum. These are the two main air shower features used to estimate the mass composition of cosmic rays [1].

2.3 Measured shower observables

The shower observables assessed in this work are the depth of the shower maximum X_{max}, the number of muons at the ground N_μ, the shape parameters of the Universal Shower Profile (USP) R and L and the muon production depth X^{μ}_{max}. They are evaluated for proton- and iron-induced showers, characterized by a certain zenith angle θ, which measures the shower inclination with $0°$ corresponding to a vertical down-going shower, and a certain azimuthal angle ϕ, with $0°$ being East.

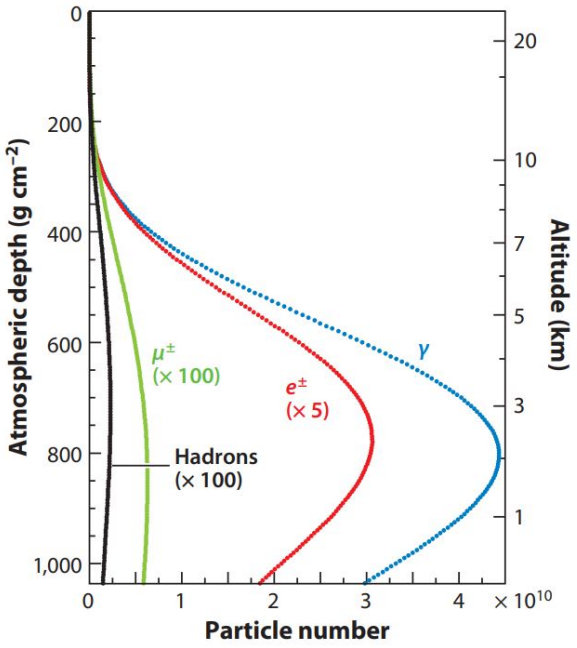

Figure 2.4: Average longitudinal shower profile for vertical, proton-induced showers at 10^{19} eV simuated with CORSIKA. Taken from [4].

As the shower develops, the traversed column density, or slant depth $X = \int \rho(l)dl$ (where ρ is the density of air and the integral must be taken along the shower trajectory), increases and it reaches a point X_{max} where the electromagnetic particle number is maximum. Figure 2.4 shows how this atmospheric slant depth (and its equivalent altitude) varies with the particle number, and we can see that different particles reach their maximum at different altitudes. It also illustrates the relative abundance of different types of particles, namely of photons, $e^{\pm}$ pairs, muons and hadrons. The energy dependence of the mean depth of the shower maximum, as measured by the Pierre Auger Observatory, is shown in Figure 2.5 (left). As expected from equation 2.2, X_{max} seems to increase with energy and the Pierre Auger Observatory data is well contained by the predictions from the different hadronic interaction models. The same happens in Figure 2.5, which presents the energy dependence of the dispersion of X_{max}. The distribution of the measured X_{max} in comparison to the predictions by the hadronic interaction model EPOS-LHC is presented in Figure 2.6 for proton- and iron-induced showers with energies between 10^{19} and $10^{19.1}$ eV. The model does not describe the Pierre Auger Observatory data well in the peak, but adding intermediate components in the mass composition, like nitrogen or helium, improves this [17].

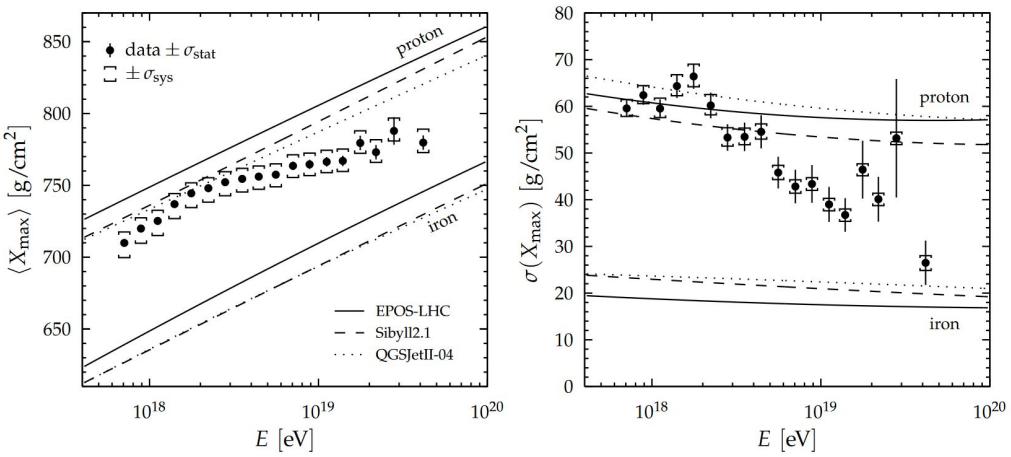

Figure 2.5: Energy evolution of the measured mean depth of the shower maximum (**left**) and of its dispersion (**right**), obtained by the Pierre Auger Observatory [18]. In both cases, the measured values are compared with the predictions from different hadronic interaction models for proton- and iron-induced showers with energy above $10^{17.8}$ eV. Taken from [19].

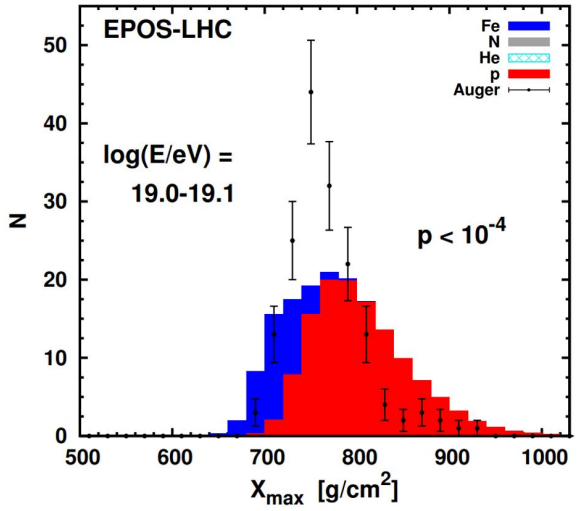

Figure 2.6: Distribution of the depth of the shower maximum for showers with energy between 10^{19} and $10^{19.1}$ eV. The data collected by the Pierre Auger Observatory is shown in gray and the predictions from the hadronic interaction model EPOS-LHC are in red (for proton-induced showers) and blue (for iron-induced showers). The p-value measures the fit quality by defining the probability of obtaining a worse fit. Taken from [17].

Another key shower observable is the number of muons at the ground, N_μ. The Pierre Auger Collaboration [20] has introduced a new parameter R_μ given by the integrated number of muons at the ground divided by a reference related to the average number of muons in simulated proton-induced showers at 10^{19} eV. On one hand, Figure 2.7 (left) shows the energy dependence of the measured average value of R_μ in comparison to hadronic interaction model simulations for proton- and iron-initiated showers. The average value of R_μ is higher for heavier nuclei and decreases with energy. However, the hadronic interaction models predict a lower number of muons than the Pierre Auger Observatory data. This is an on-going unsolved problem in the cosmic ray field, and will be further discussed in section 2.4. On

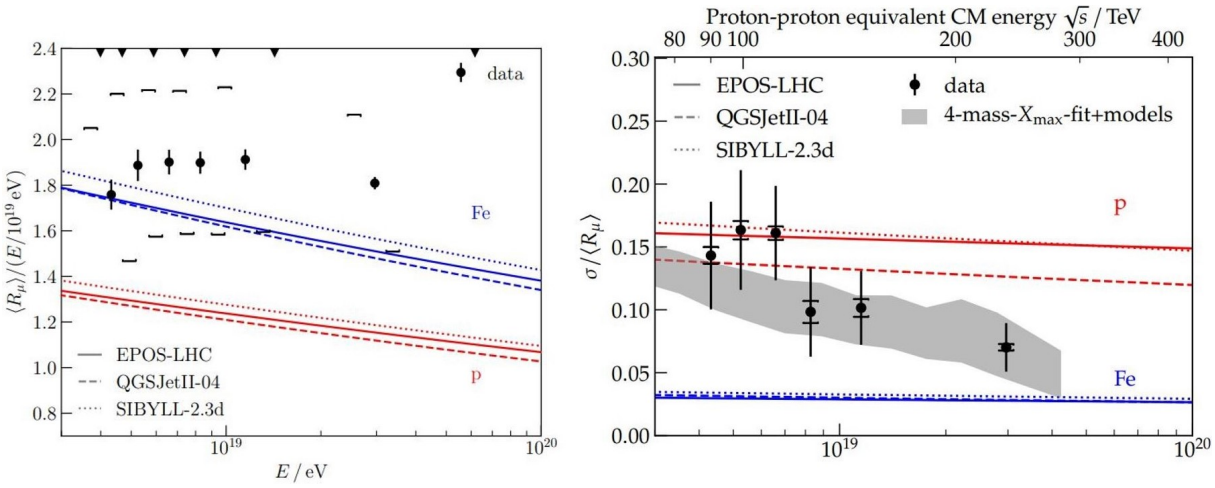

Figure 2.7: **Left**: Measured average value of R_μ as a function of the energy, compared with the predictions from hadronic interaction models EPOS-LHC, QGSJET II-04 and SIBYLL-2.3d for pure proton- (red) and pure iron-induced (blue) showers. **Right**: Relative fluctuations in the number of muons measured as a function of the energy, compared with the predictions from EPOS-LHC, QGSJET II-04 and SIBYLL-2.3d for proton- (red) and iron-induced (blue) showers. The gray band represents the expectations from the measured mass composition interpreted with the hadronic interaction models. The statistical uncertainty in the measurement is represented by the error bars and the total systematic uncertainty by the square brackets. Both figures taken from [20].

the other hand, Figure 2.7 (right) presents the energy dependence of the measured relative fluctuations in the number of muons at the ground and compares it with the predictions from different hadronic interaction models and from the measured mass composition. Within the current uncertainties, there is no discrepancy between the measured fluctuations and the ones predicted from the hadronic interaction models or from mass composition. Furthermore, Figure 2.8 shows the average logarithmic muon content as a function of the mean value of X_{max}, comparing the data collected by the Pierre Auger Observatory with the predictions from different hadronic interaction models. Notice that $\langle \ln R_\mu \rangle$ decreases with increasing $\langle X_{max} \rangle$, going from heavier primary particles to lighter ones.

Moreover, since the number of particles of (N) and the energy deposited by (dE/dX) the air shower are proportional, the longitudinal electromagnetic profile of the shower can be shown as one of these variables as a function of the slant depth and can be measured by the detection of fluorescent light at the ground [20]. However, it is mostly determined by the maximum number of particles reached (N_{max}) and the corresponding depth (X_{max}) and has a characteristic universal shape when normalized ($N' = N/N_{max}$) and translated ($X' = X - X_{max}$) to the shower maximum [21]. This universal shape is shown in Figure 2.9 for 100 simulated proton- and iron-induced showers. The Gaisser-Hillas parametrization [22] is an accurate functional form to describe the central part (-300 to +200 g/cm^2) of these longitudinal profiles for showers with energies above $10^{17.8}$ eV at 1% accuracy [23]. It expresses the number of particles N as a function of the traversed atmospheric depth X as follows:

$$N(X) = N_{max} \left(\frac{X - X_0}{X_{max} - X_0} \right)^{\frac{X_{max} - X_0}{\lambda}} exp\left(\frac{X_{max} - X}{\lambda} \right), \tag{2.8}$$

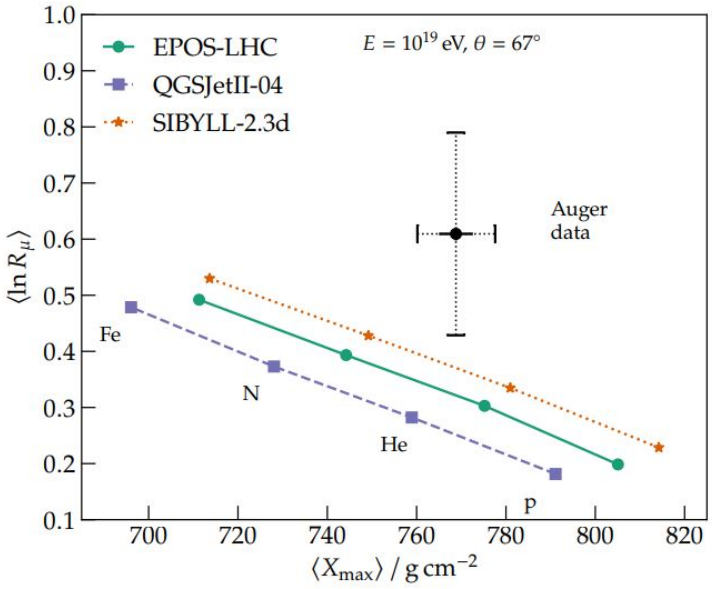

Figure 2.8: Average logarithmic value of the muon content ratio R_μ as a function of the average value of the depth of the shower maximum. Data collected by the Pierre Auger Observatory is shown in black and compared with different hadronic interaction model predictions for showers with an energy of 10^{19} eV and an inclination of $67°$. The showers have primaries with different mass compositions, from pure iron (on the far left) to pure proton (on the far right). Taken from [20].

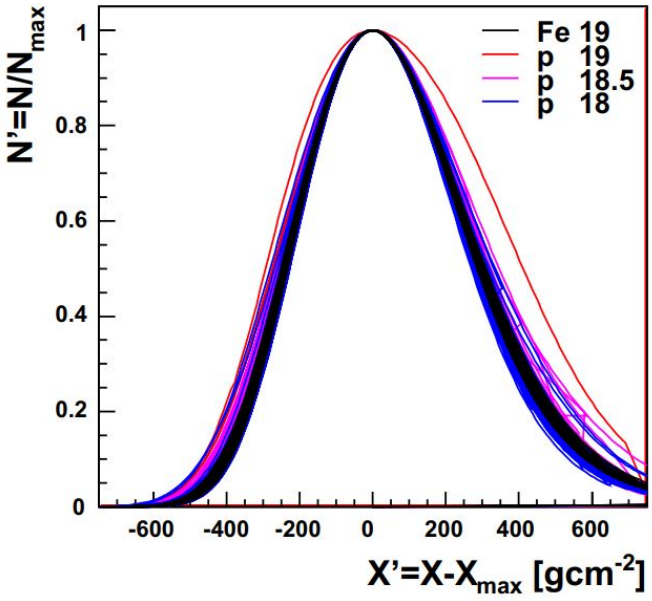

Figure 2.9: Longitudinal profiles for 100 simulated proton- and iron-induced showers, with energies between $10^{17.5}$ eV and 10^{20} eV, using hadronic interaction models QGSJet-II.03 and EPOS 1.99 with the EAS simulator CONEX. Taken from [21].

where λ and X_0 are primary mass and energy dependent parameters, with the first being identified with an effective interaction length and the second with the point of the first interaction. Manipulating equation 2.8 [21], we can write it in terms of the USP shape parameters $L = \sqrt{|X_0'\lambda|}$ and $R = \sqrt{\lambda/|X_0'|}$, with $X_0' = X_0 - X_{max}$, as:

$$N' = \left(1 + \frac{RX'}{L}\right)^{R^{-2}} exp\left(-\frac{X'}{LR}\right). \tag{2.9}$$

The Gaisser-Hillas function assumes a Gaussian shape with a standard deviation L and asymmetry governed by non-zero R. These parameters are less correlated and more stable than λ and X_0 [24]. While L is a characteristic shower length with a small dependence on the primary particle type and event-by-event fluctuations of the order of a few percent [21], R has a small impact on the full integral of the profile (which can be approximated to $\sqrt{2\pi}L$) but is sensitive to primary particle types, both in its mean value and in its fluctuations [25]. In fact, R measures both the growing rate of the number of particles from the first interaction to X_{max} and the distance between this variable and the depth of the first interaction X_1, while being experimentally independent from X_{max}. Both USP shape parameters can be used to derive information on the mass composition of the primary particle and to evaluate the tunings of hadronic interaction models [24]. The evolution of L and R with energy is shown in Figure 2.10. From Figure 2.10 (left), we see that R decreases with energy and so the showers get less asymmetrical and more Gaussian with increasing energy. From Figure 2.10 (right), we see a linear increase of L with energy, which makes sense since L is the width of the Gaussian and therefore is related to its integral and thus to the shower energy. Figure 2.11 presents the L and R values for each of the three different hadronic interaction models compared and possible composition combination, from pure proton to pure iron primaries. One can observe that the phase space spanned by each model partially overlaps the data collected by the Pierre Auger Observatory, within its systematic uncertainties.

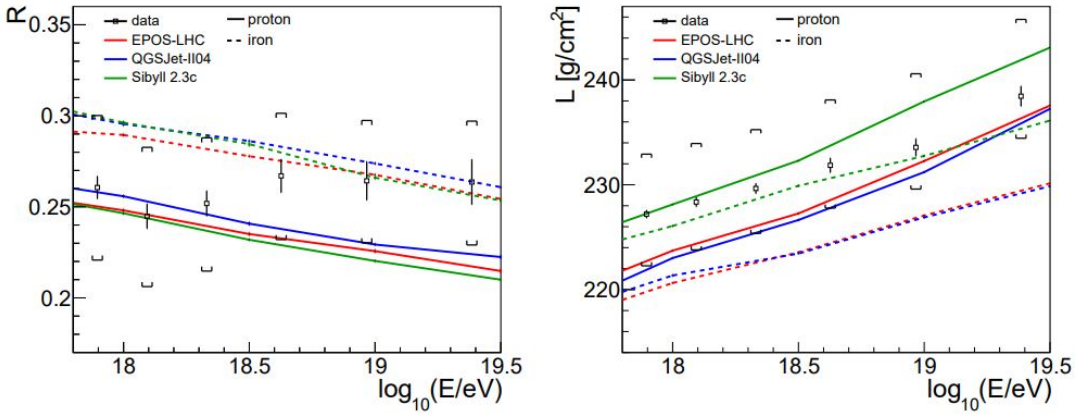

Figure 2.10: The USP shape parameters R (**left**) and L (**right**) as a function of the shower energy. Data collected by the Pierre Auger Observatory is shown in black, with the vertical lines representing the statistical errors and the brackets the systematic uncertainties. The full lines and the dashed lines are the predictions from the hadronic interaction models simulated with CORSIKA for proton and iron primaries, respectively. Taken from [23].

While X_{max} refers to the slant depth where the number of electromagnetic particles is maximum, X^{μ}_{max} is the muon production depth maximum, i.e. the slant depth at which the number of produced muons per slant depth unit is maximum. Comparing the electromagnetic and muonic profiles, X^{μ}_{max} is always reached before X_{max} (around 200 g cm^{-2} earlier). Figure 2.12 (right) shows the distribution of X^{μ}_{max} for proton- and iron-induced showers simulated with hadronic interaction model EPOS-LHC. The

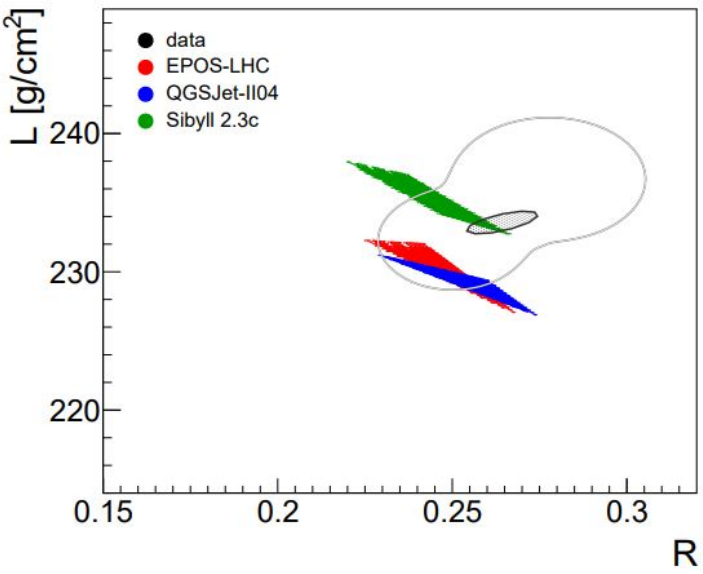

Figure 2.11: The USP shape parameter L in function of the USP shape parameter R for proton-, helium-, nitrogen- and iron-induced showers with energies between $10^{18.8}$ and $10^{19.2}$ eV. Each of the coloured points represents the values of R and L for a given hadronic interaction model and composition combination, with pure proton being in the upper left side and pure iron in the lower right side. The inner dark gray ellipse shows the fitted value for the Pierre Auger Observatory data and its statistical uncertainty, and the outer light gray line the systematic uncertainty. Taken from [23].

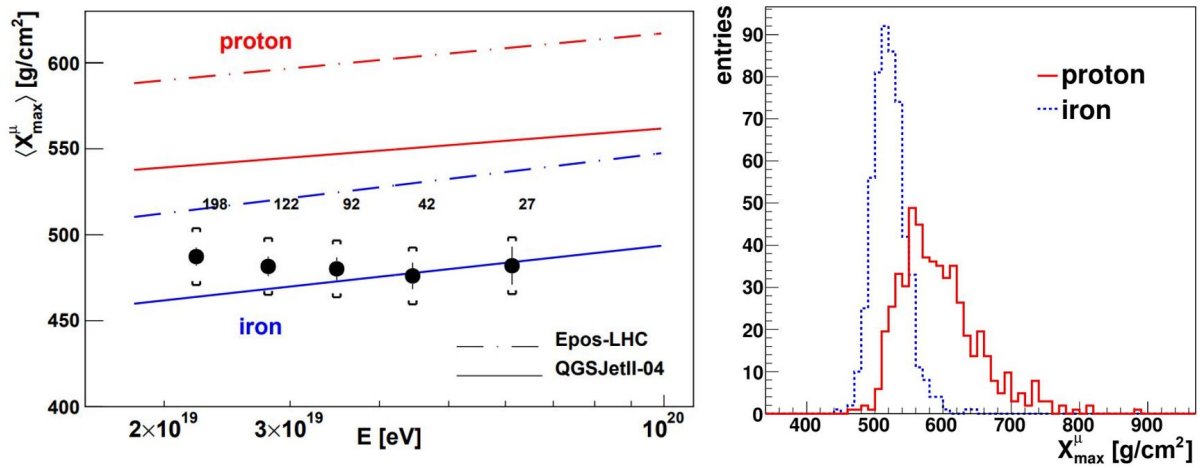

Figure 2.12: **Left**: Energy dependence of the mean value of the muon production depth maximum. Data collected by the Pierre Auger Observatory is shown in black and compared with different hadronic interaction model predictions for proton- and iron-induced showers. The numbers close to the data indicate the number of events in each energy bin. The brackets represent the systematic uncertainty while the error bars represent the standard deviation of the mean. **Right**: Distribution of the muon production depth maximum for proton- (red) and iron-induced (blue) showers simulated at $3\text{x}10^{18}$ eV with EPOS-LHC at zenith angles between $55°$ and $65°$. Both figures taken from [26].

iron-induced showers have a narrower distribution, covering the low-end values of X^{μ}_{max}, while proton-induced showers have a broader distribution that covers higher values of X^{μ}_{max}. Aditionally, Figure 2.12 (left) displays the energy evolution of the mean value of X^{μ}_{max}, comparing data from the Pierre Auger

Observatory with the predictions from different hadronic interaction models. The data is well bracketed by the QGSJetII-04 model, but not by EPOS-LHC, since this model predicts deeper showers than the experimental measurements. However, note that both models estimate a similar muonic elongation rate (i.e. the evolution of X^{μ}_{max} with energy).

2.4 Muon Puzzle

Comparing the data obtained from measurements of extensive air showers with the predictions from LHC-tuned hadronic interaction model simulations, we find that these models consistently predict a lower muon production. This discrepancy, know as the Muon Puzzle, had already been noticed in the year 2000 by the HiRes/MIA collaboration [27] and has since triggered several more measurements, namely by the NEVOD-DECOR [28, 29], KASCADE-Grande [30], EAS-MU [31], IceCube Neutrino Observatory [32], SUGAR [33], Pierre Auger Observatory [34] and AMIGA [35], Telescope Array [36] and Yakutsk [31] experiments. However, a direct comparison of these measurements is not possible, since the lateral muon density at the ground depends on many parameters that differ from experiment to experiment, like the cosmic ray energy, the zenith angle, the shower age, the lateral distance from the shower axis and the energy threshold of the muon detectors. Thus, each experiment compares its data to air shower simulations, producing a data/simulation ratio that is comparable between different analyses and experiments if simulations with the same hadronic interaction model are available for all measurements. So we are no longer interested in the lateral muon density in itself, but on the ratio between the lateral muon density measured experimentally and the lateral muon density obtained via air shower simulations. Nevertheless, although most air shower parameters can be easily matched in simulation and experiment, the cosmic ray energy is quite difficult and has a large impact, with a 20% energy-scale offset producing a 18% offset in the data/simulation ratios [37]. To solve this issue, the Working group on Hadronic Interactions and Shower Physics (WHISP) [31] used the isotropic quality of cosmic ray fluxes up to $10^{19.2}$ eV to employ them as a universal reference to compute a relative energy-scale ratio E_{data}/E for each experiment such that the all-particle fluxes overlap. It is important to note that this cross-calibration cannot eliminate a global offset of all experiments to the true energy scale, which translates into corresponding shifts in the data/simulation ratios, with the reference energy-scale having an uncertainty of at least 10%. To compare all the measurements, the WHISP introduced the abstract muon scale parameter z defined as

$$z = \frac{\ln(N_{\mu}^{det}) - \ln({N_{\mu_p}}^{det})}{\ln({N_{\mu_{Fe}}}^{det}) - \ln({N_{\mu_p}}^{det})}, \tag{2.10}$$

where N_{μ}^{det} is the muon density estimate as seen in the detector, and ${N_{\mu_p}}^{det}$ and ${N_{\mu_{Fe}}}^{det}$ are the simulated muon density estimates for proton- and iron-induced showers, accounting for detector effects, respectively [31]. This means that each experiment has its own z and the conversion to z is only possible when ${N_{\mu_p}}^{det}$ and ${N_{\mu_{Fe}}}^{det}$ are available in the hadronic interaction model used under the specific experimental conditions applied. The z-scale ranges from 0 (pure proton-induced showers) to 1 (pure iron-induced

showers), if there is no discrepancy between real and simulated air showers. Note that because of the uncertainty on the reference energy-scale after cross-calibration, the z-values can be collectively varied by about ± 0.25. Figure 2.13 shows the muon density measurements converted to the z-scale for the EPOS-LHC hadronic interaction model, after energy-scale cross-calibration. As we can see, muon measurements seem to be consistent with simulations up to 4×10^7 GeV, which corresponds to a center-of-mass energy of $\sqrt{s_{NN}} \approx 8$ TeV, within the reach of the LHC. From these energies up, there is a growing muon deficit in the simulations with a slope in z per decade in energy of 0.22, with 8σ significance. This significance is higher than that of any individual measurement, where the significance for a muon deficit does not exceed 3σ [1]. Figure 2.13 (a)-bottom and (b) deal with the expected value $z_{mass} = \frac{\langle lnA \rangle}{ln56}$, with $\langle lnA \rangle$ being converted from X_{max} based on air shower simulations with EPOS-LHC. The model would describe the muon density at the ground consistently if the measured z values followed z_{mass}, which is not the case. In fact, the difference $\Delta z = z - z_{mass}$ (Figure 2.13 (b)) should remove the effect of the changing mass composition, but we still see an energy-dependent trend in Δz. This quantity can be interpreted as the relative muon deficit in units of proton-iron difference, with $\Delta z \approx 1$ at 20 EeV corresponding to a muon deficit in simulations of about 40% [1].

$J_{sim}\left(\frac{N_{\mu data}}{R}\right)\frac{1}{R}$

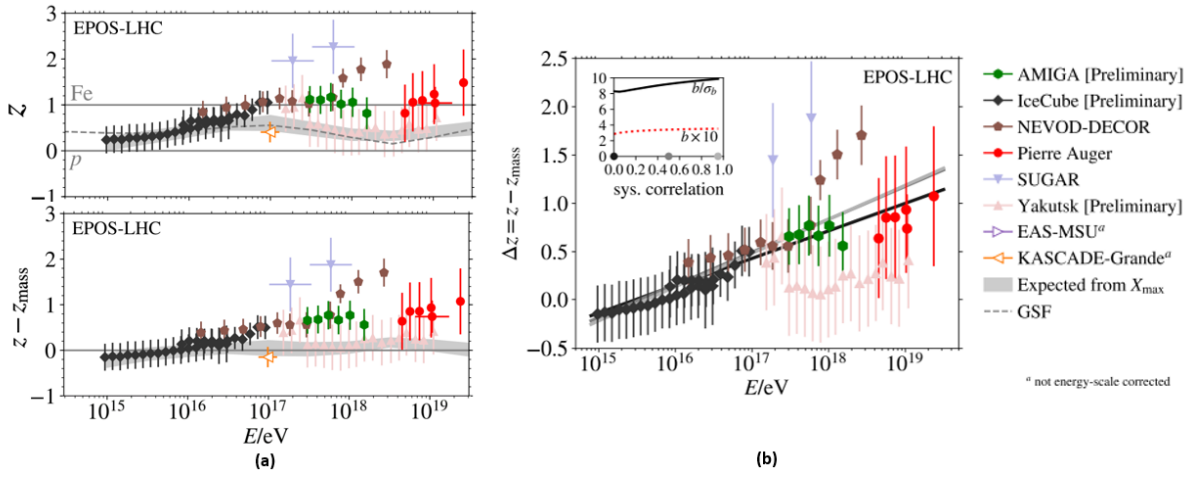

Figure 2.13: Muon density measurements from various experiments converted to the z scale for the EPOS-LHC hadronic interaction model, after energy-scale cross-calibration using the isotropic all-particle flux of cosmic rays as a reference. The gray band represents the expected muon-value inferred from X_{max}, while the dashed line represents the muon-value computed from the Global Spline Fit (GSF) model. **(a)** presents these measurements both for the z scale as for the $z - z_{mass}$ scale, with z_{mass} being the expected variation in z due to changes in the cosmic ray composition, inferred from X_{max} measurements. **(b)** shows fits of the line-model $\Delta z = a + b \log_{10}(E/10^{16}\,\mathrm{eV})$ to the data points, assuming a correlation coefficient $\alpha = 0.5$, resulting in $b = 0.34 \pm 0.04$ (increase in δz per decade in energy). Displayed in the inset are the slope b and its deviation from zero in standard deviations for an assumed correlation of the point-wise uncertainties within each experiment. Examples of the fitted lines are shown for a correlation of 0, 0.5, and 0.95 in varying shades of gray. The z-values from KASCADE-Grande and EAS-MSU are not included in the fit of Δz because they are not energy-scale corrected and thus not directly comparable to the other values. Based on [31, 37].

Note that the results of Figure 2.7 (right), which shows the energy dependence of the relative fluctuations in the number of muons at the ground, as was already mentioned in section 2.3, besides disfavouring some exotic explanations for the Muon Puzzle, also suggests that the adjustments made to the hadronic interaction models in order to correct this muon deficit must not alter the predicted relative fluctuations. Additionally, Figure 2.12 (left), which exhibits the energy dependence of the muon production depth, indicates that these corrections must also produce shallower muon production depths. The Pierre Auger Collaboration results suggest that the muon deficit in the simulations of the hadronic interaction models comes from a small deficit at every stage of the shower that accumulates along its development, rather than a discrepancy in the first interaction. The approximately linear increase of the relative muon deficit above 4x10^7 GeV, when the number of shower stages above this energy also increases linearly, points towards this compounding effect as well [1].

Other measured muon related observables have shown discrepancies with hadronic interaction model simulations, namely the muon production depth, the muon attenuation with zenith angle and mass overburden, the high-energy atmospheric muon flux, the lateral separation of TeV muons and the seasonal variations of atmospheric muon and neutrino fluxes (see [1] for a review).

Many attempts have been made to address the Muon Puzzle and a comprehensive summary of the rejected ones can be found in [38]. However, most attempts have focused on altering some characteristics of the hadronic interaction models in order to force them to increase their muon production without compromising their consistency [39]. For example, the presence of string percolation [40–42] at energies around $\sqrt{s} \sim$ 30-40 TeV has been one of the suggestions [43]. The idea behind this theory is that string percolation would reduce the number of particles that feed the electromagnetic component of the shower (such as electromagnetic particles and neutral pions) while increasing the production of baryons and strange mesons, which would lead to an increase of the muon production. However, this approach, as many others, increases X_{max}, the air shower observable that is the least sensitive to hadronic interaction properties and relatively well-described by simulations with current post-LHC models. Furthermore, it has been proven that baryon and anti-baryon production is a very efficient mechanism to affect the muon numbers in simulations without changing X_{max} [44]. Indeed, the number of muons at the ground is very sensitive to the ratio between the total number of particles in the hadronic component of the shower and the total number of particles of the shower, such that the muon number increases with this ratio. And despite the fact that baryons and anti-baryons represent only 1% of all hadrons, a slight increase in the baryon number decreases considerably the number of fast neutral pions in the next generations, leaving more contributors to the hadronic cascade and thus providing more muons. Nevertheless, parameter tuning of the hadronic interaction models has been unsuccessful, mainly because the required changes to the existing models would imply violating data constraints or the consistency between air shower simulations and the other air shower features.

A promising approach would thus be the introduction of new phenomena at high energy that could preserve the main features of the interaction while increasing the strangeness production. Such a mechanism has indeed been observed at the LHC in heavy-ion collisions - the formation of Quark Gluon Plasma.

Chapter 3

Theoretical Overview of Quark-Gluon Plasma

3.1 QGP and Heavy-Ion Collisions

Quark-Gluon Plasma (QGP) is a dense, energetic 'soup' made of asymptotically free quarks and gluons that manifest colour degrees of freedom on nuclear scales, but that are always very strongly coupled to each other [45, 46]. In fact, QGP exhibits a relativistic hydrodynamic fluid-like behavior with an extremely low viscosity to entropy ratio [47]. Besides being the earliest complex state of matter to form in the Universe, it can be produced in heavy-ion collisions, like the ones performed at the RHIC [48–51] and at the LHC [46, 52–55]. Figure 3.1 shows the space-time evolution of QGP, with the left side showing snapshots of the first fm/c of a central Pb-Pb collision and the right side a schematic view of the different phases of a heavy-ion collision, from the formation of QGP until the freeze-out after hadronization. This evolution can be qualitatively described as follows. A thin cylindrical volume of QGP liquid is formed very early in the collision (as we can see from the red colouring in Figure 3.1 (left)), with a high entropy that is determined very quickly before the fluid hydrodynamizes. Initially, it has a non-uniform high energy density and temperature distribution determined by the lumpiness of the colliding nuclei. While QGP is being produced between the two receding Lorentz-contracted discs and expanding and cooling, new hot and high baryon-density QGP is continually and simultaneously being formed in the high-rapidity regions close to the outgoing remnants of the nuclei (again, see Figure 3.1 (left)). QGP is thus formed at various pseudo-rapidities, with the low baryon-density QGP being produced in the most central regions. Each elemental volume of QGP expands in all directions and cools, eventually allowing for the hadronization process to begin. The produced hadrons scatter off each other for a while, forming a hadron gas. As the gas expands and the density drops, inelastic and elastic interactions eventually stop, producing a chemical and a kinetic freeze-out. Afterwards, the hadrons stream outwards freely, reaching its final-state measured experimentally in the detectors.

The scenario thus described so far corresponds to the core part of the core-corona model, which will be discussed in section 4.1, and deals with the soft interacting partons. But a small fraction of the

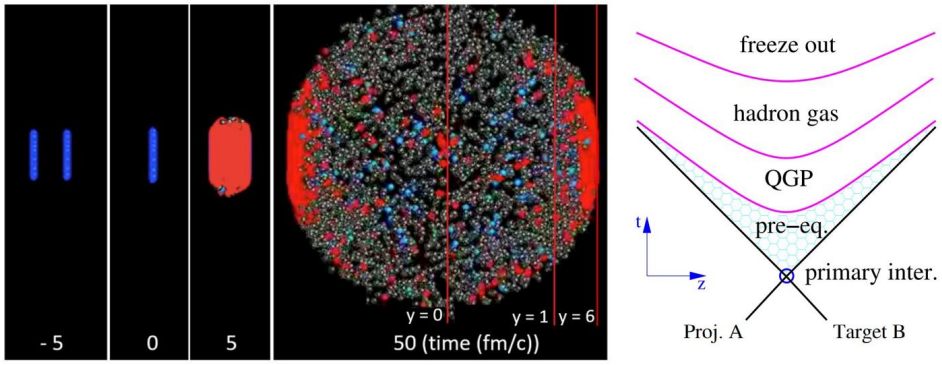

Figure 3.1: **Left**: Snapshots of a central 2.76 TeV Pb-Pb collision at different times with hadrons (in blue and grey) and QGP (in red). The red lines indicate the approximate longitudinal location of particles with rapidity $y = 0$, $y = 1$ and $y = 6$. Taken from [47]. **Right**: Schematic view of the general space-time evolution of QGP, from the heavy-ion collision to the final freeze-out. This also corresponds to the core part of the core-corona model. Taken from [2].

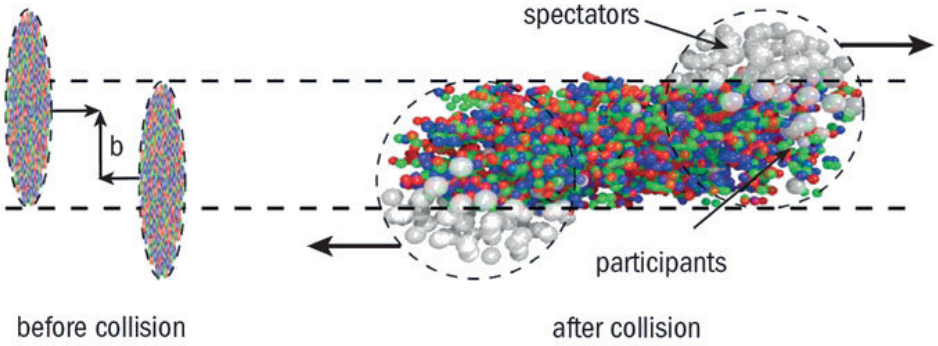

Figure 3.2: Scheme for an off-central heavy-ion collision, which produces an approximately elliptical collision region (participants). The parameter b is the collision impact parameter. Taken from [56].

incident partons suffer large-angle scattering and thus hard perturbative interactions, producing early-on particles with high-transverse momentum. Traversing through the QGP formation and evolution region, the partons evolve, decay, radiate and form jets of hadrons and/or heavy $q\bar{q}$ pairs. Since the lifetime of QGP is very short (around 10 fm/c), its properties have to be extracted indirectly from detecting the particles (soft and hard) emitted from the collision point at much later time scales [46]. The behaviour and the characteristics of these particles act as experimental signatures of QGP, as will be discussed in section 3.2, and are highly dependent on the centrality of the collision. In fact, the collision of the two nuclei can be of two types: either central, meaning the ions collide head-on (see Figure 3.1 (left)), or off-central if the ions only partially overlap (see Figure 3.2). In this last case, the QGP medium is formed with an initial approximately lenticular shape in the transverse plane, whereas in central collisions the shape is more circular. However, there are different classes of centrality, as is shown in Figure 3.3. This Figure presents the relation between the cross-section of the participating nucleons, their number, the number of produced charged particles, the impact parameter b and the different centrality classes. The more central the collision, or, in other words, the bigger the overlap region of the two incident nuclei, the

more visible are the QGP effects.

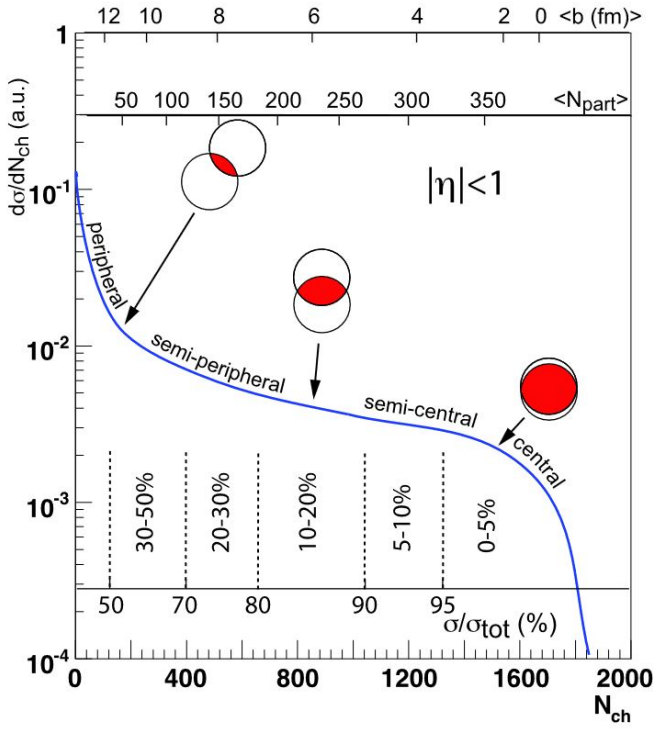

Figure 3.3: The cross-section σ of the participating nucleons of a heavy-ion collision in function of the number of produced charged particles N_{ch}, of the average number of participating nucleons N_{part} and of the average impact parameter b. These relations define different centrality classes, from peripheral to central. The values presented are merely illustrative and do not constitute actual measurements. Taken from [57].

3.2 Experimental Signatures

As mentioned in section 3.1, in order to recreate QGP, powerful accelerators, like the LHC and the RHIC, make head-on collisions between massive ions, such as gold or lead nuclei, searching for signals induced by this new state of matter. Indeed, QGP-like phenomena appears to have been observed in various experiments spanning a wide range of densities, from dense-dense collisions (such as Pb-Pb, Au-Au and Xe-Xe) to dense-dilute (like p-Pb and He-Au) and even to dilute-dilute (namely high multiplicity pp) [46, 58]. So far, the most visible effects of the presence of QGP are strangeness and baryon enhancement, anisotropic and transverse collective flow and jet-quenching. Each of these signatures will be discussed in this section.

Strange quarks are not present as valence quarks in the incident nuclei of heavy-ion collisions, but they are abundantly created during the collision as $s\bar{s}$ pairs [59]. In the initial stages of the collision, strangeness is produced in hard partonic scattering processes by flavour creation ($gg \to s\bar{s}$ and $q\bar{q} \to s\bar{s}$) and flavour excitation ($gs \to gs$ and $qs \to qs$), whereas during the evolution of the partons, it is created via gluon splittings ($g \to s\bar{s}$) [60]. When the quark matter hadronizes, the numerous $\bar{s}$ quarks may, instead of being bound into a $q\bar{s}$ kaon, form $q\bar{q}s$ or $q\bar{s}s$ anti-baryons such as $\bar{\Lambda}$, $\bar{\Sigma}$ or $\bar{\Xi}$. In fact,

strange quarks reach chemical equilibrium quickly in the QGP medium, allowing for strange hadrons to be produced in equilibrium abundances [61]. This strangeness and baryon enhancement has been observed at the RHIC and LHC [48, 50, 51, 62]. Figure 3.4 presents the multiplicity dependence of the transverse momentum (p_T) integrated yields of strange and multi-strange particles, relative to pions, measured at mid-rapidity for pp, p-Pb and Pb-Pb collisions. The particle ratio increases significantly with the event multiplicity until it reaches a plateau. If this universal strangeness and baryon enhancement that only depends on the multiplicity of the event at mid-rapidity holds, it allows us to extrapolate the data of measurements in central Pb-Pb collisions at current LHC energies to predict the hadron composition in average collisions of p-A at $\sqrt{s} \approx 10$ TeV. It is important to note that most of this data was obtained with particles emitted at mid-rapidity, but extensive air showers are mostly dominated by particles produced in the forward region, from $\eta > 2$ and up. Theoretical calculations suggest that hadrons produced from QGP decay in pp collisions at $\sqrt{s} \approx 13$ TeV can be found in the forward region up to $\eta \simeq 6.5$ [47, 63].

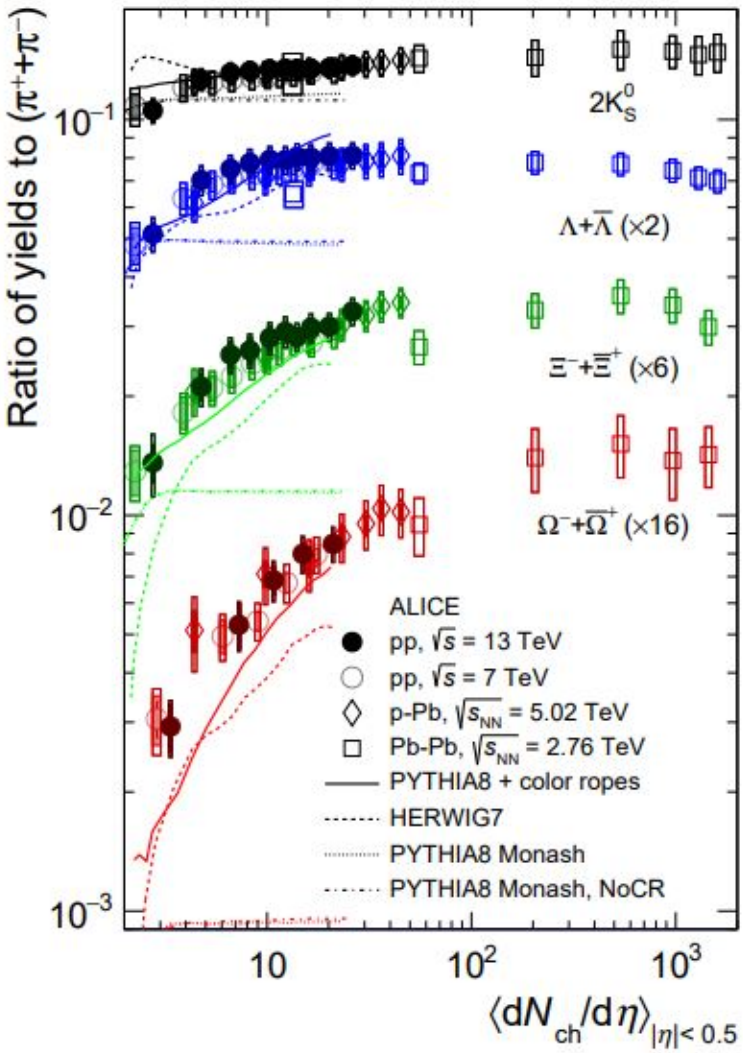

Figure 3.4: p_T-integrated strange hadron-to-pion ratios as a function of the mean charged-particle multiplicity density measured at mid-rapidity ($|\eta| < 0.5$) for pp, p-Pb and Pb-Pb collisions. The open shaded boxes around the markers represent full systematic uncertainties (multiplicity uncorrelated). Also, different lines represent different Monte Carlo generators for pp collisions at $\sqrt{s}$ = 13 TeV. Taken from [64].

As already mentioned in section 3.1, the lumpiness of the colliding nuclei is responsible for an anisotropic distribution of energy density, which is expected to increase with less central collisions. Since QGP forms at this stage, its rapid hydrodynamization produces significant first order gradients (initially mostly in the longitudinal direction) in such a way that it expands faster in the directions of larger gradients, which means that the hydrodynamical behaviour of QGP translates spatial anisotropies into momentum anisotropy. And because of the incredibly low viscosity to entropy ratio of QGP, the anisotropies persist and the isotropization and complete thermalization of QGP only happen at a substantially later time (after a proper time of roughly τ = 6 fm/c [65]). This means that the hadrons formed by recombination inherit the flow pattern of their constituents quarks (in other words, they inherit the momentum anisotropy of QGP), forming the phenomenon know as collective elliptic flow. In fact, the characterization of particle azimuthal momentum anisotropies is made through the Fourier transform on the angular distribution of charged hadrons in the final state of the collision [66]:

$$\frac{dn}{d\phi} \propto 1 + \sum_{n} 2v_n(p_T)cos[n(\phi - \psi_n)]. \tag{3.1}$$

Among the several coefficients of equation 3.1, elliptic flow (the second Fourier coefficient v_2) is the largest and most studied observable, since it is closely related to the initial spatial anisotropy induced by the nuclear overlap region in the transverse plane of a non-central heavy-ion collision. Also, it is the dominant coefficient for semi-central collisions near mid-rapidity [67].

As seen in section 3.1, in occasional heavy-ion collisions, partons from the incident nuclei scatter off each other at very large angles and momentum transfer, creating parton pairs or gauge bosons with very high transverse momentum. Each produced parton then showers into a spray of softer partons within some irregular cone in momentum space, called a jet. As these particles travel trough the QGP medium, they lose energy to it [68]. Thus, the number of jets with a given high transverse momentum is suppressed in heavy-ion collision relative to what would be seen in the number of binary collisions (N_{coll}) of pp collisions, especially for the central ones in which the QGP area that the jets traverse is the largest. This is known as jet-quenching and the modification of high-p_T particle production is quantified by the nuclear modification factor R_{AA}, which is given by the expression:

$$R_{AA} = \frac{dN^{AA}/dp_T}{\langle N_{coll}\rangle dN^{pp}/dp_T}, \tag{3.2}$$

where N^{AA} and N_{pp} are the charged-particle yields in A-A and pp collisions, respectively, and $\langle N_{coll}\rangle$ is the average number of binary nucleon-nucleon collisions. This factor has been measured by the PHENIX and STAR experiments at the RHIC for central Au-Au collisions at $\sqrt{s_{NN}}$ = 130 and 200 GeV [69, 70] and by the ALICE, CMS and ATLAS experiments at the LHC for central Pb-Pb collisions at $\sqrt{s_{NN}}$ = 2.76 and 5.02 TeV [71–75]. Figure 3.5 shows the results of these LHC measurements, specifically the nuclear modification factor dependence on transverse momentum for different centrality classes. Being very similar in magnitude for the two collision energies, the R_{PbPb} has a strong centrality dependence, reaching higher values for more peripheral collisions. The more central collisions show more visible QGP effects, namely jet-quenching, which leads to lower values of R_{PbPb}. Also note that the particle

suppression is in general higher for low-p_T, especially in the more central collisions. Nevertheless, jet-quenching is the only QGP signature that we have not been able to observe in lighter systems, such as p-A collisions. This is one of the big questions in the field, because the evidence with which we see the other QGP signatures (see [60, 76–79]), especially in different systems with the same final state particle density, suggests that we should also be able to observe jet-quenching. Therefore, although QGP models enjoy great success in describing heavy-ion collisions, there is still controversy whether it also forms in small systems. However, the similarities found seem to indicate that proton-sized droplets of QGP could be found in pp and p-A collisions with sufficiently large final state particle density [59, 80]. Some simulations of O-O collisions suggest that even though a formation of a large QGP medium is not likely in small systems, local droplets of QGP are probable, which could explain the lack of jet-quenching [81]. Moreover, signatures of fluid-like behavior have also been reported in p-Pb collisions at $\sqrt{s} = 2.76$ TeV at the LHC [82, 83], and evidence of a small QGP formation in ^{3}He-Au collisions has been recorded at RHIC at $\sqrt{s} = 200$ GeV [84]. Table 3.1 sums up the most visible experimental signatures of QGP for each colliding system.

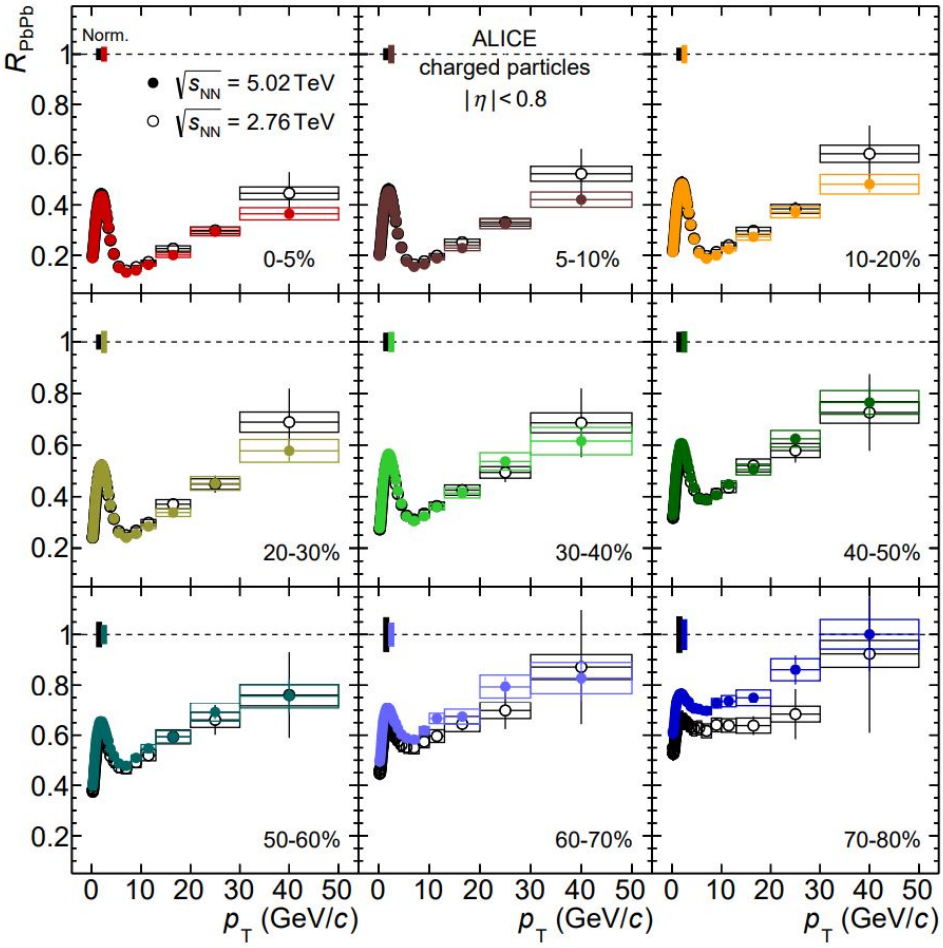

Figure 3.5: The nuclear modification factor dependence on the transverse momentum measured by the ALICE collaboration in Pb-Pb collisions at $\sqrt{s} = 2.76$ (open symbols) and 5.02 TeV (full symbols), for charged particles in the pseudo-rapidity region $-0.8 < \eta < 0.8$ and for different centrality classes. The boxes around unity show the normalization uncertainties. Taken from [75].

	Strangeness and baryon enhancement	Collectivity effects (flow)	Jet-quenching
pp	no (except high-multiplicity)	no (except high-multiplicity)	no
p-Pb	yes	yes	no
Pb-Pb	yes	yes	yes

Table 3.1: Correspondence between each experimental signature of QGP and the possible colliding systems in which they have been observed, from dilute-dilute (pp) to dense-dilute (p-Pb) and dense-dense (Pb-Pb).

3.3 QGP and the Muon Puzzle

Among the many proposals to solve the Muon Puzzle, the formation of a deconfined thermal fireball that undergoes a sudden hadronization in the first interaction of EAS was proposed by [85]. Besides assuming that cosmic rays at the highest energies have heavy or medium mass primaries, they argue that the high baryochemical potential of this fireball enhances the production of strange hadrons. This would suppress the fraction of energy deployed in the electromagnetic subshowers of the cascade by about 20%, which would lead to an increase of the muon content by 40%. However, this proposal would require an extreme combination of temperature and baryochemical potencial not reproduced in heavy-ion collisions at the LHC [45] and was thus disfavoured. Nevertheless, the source of the muon deficit should be observed in high-energy collisions at the LHC, and the most likely explanation consistent with all the available data is, indeed, the presence of a phenomenon that reduces the energy fraction carried by the electromagnetic component of the shower. But the effects of this phenomenon should be softer than the ones proposed by [85] and more distributed along the several generations of the hadronic cascade, as discussed in section 2.4. This compounding effect on the hadronic cascade would cause large changes in the number of muons over several shower stages, while leaving X_{max} and the relative muon fluctuations intact. The strangeness and baryon enhancement found by the ALICE collaboration fits into the picture quite well, although its results were achieved at mid-rapidity. This means that measurements of forward hadron production at pseudo-rapidities $\eta > 2$ are needed, namely with LHCb and future data on oxygen beams at the LHC at the end of Run 3 to study p-O and O-O collisions at $\sqrt{s} = 10$ and 7 TeV.

Chapter 4

Hadronic Interaction Models

Quantum Chromodynamics (QCD) governs hadronic multiparticle production, but only hard interactions are calculable by perturbative methods. Since the majority of particle production in high-energy hadronic collisions is dominated by forward and soft QCD interactions with low momentum transfer, phenomenological models are often combined with perturbative QCD predictions for high-p_T processes to obtain an almost complete description of the final states [86]. Hadronic interaction models are essentially attempts to calculate hadronic multiparticle production with parameters constrained by the existing collider data and in such a consistent way that allows for a theory-guided extrapolation to ultra-high energies and to different phase-space regions than the ones explored in accelerators [4]. Tests and measurements of hadronic interaction properties with air showers can reduce uncertainties in modeling the shower development and can be used to test the Standard Model of particle physics under extreme conditions [37]. The leading hadronic interaction models used for air shower simulations are EPOS-LHC [87], QGSJet-II.04 [88] and SIBYLL-2.3d [89], which are all post-LHC models, but are not describing correctly all aspects of hadronic physics in air showers, as was already seen in section 2.4 [37]. In this work, we use EPOS-LHC and EPOS-QGP, which will be introduced in section 4.2, along with CONEX [90, 91], an EAS simulation code that combines Monte Carlo simulations for the most energetic interactions with the solving of cascade equations at lower energies to simulate the longitudinal development of the shower along its axis. This hybrid approach makes it an extremely fast code, allowing for the simulation of large statistical samples of EAS.

4.1 EPOS-LHC

EPOS-LHC is a Monte Carlo hadronic interaction generator focused on minimum-bias pp and heavy-ion collisions that can be used for extensive air showers. It is tuned to the latest CERN's LHC data, which has allowed us to access the energy region above the cosmic ray spectral *knee* in the laboratory reference frame, namely $\sqrt{s} = 14$ TeV. This data has mostly been taken with detectors covering the central phase space region in pseudorapidity ($|\eta| < 2.5$), which is the region with the bulk of produced particles. However, the most important particles to understand air showers are the most energetic

outgoing ones, emitted in the very forward region of the collider [92]. EPOS is the only model used both for EAS simulations and accelerator physics which is able to reproduce consistently almost all data from 100 GeV in the laboratory reference frame to 1.8 TeV center-of-mass energy, including antibaryons, multi-strange particles, ratios and p_T distributions [44].

EPOS was the first generator to combine Parton-Based Gribov-Regge theory [93], perturbative QCD and string fragmentation with quark-gluon plasma formation to describe both small and large collision systems [1], through the use of the core-corona model [63, 94], in which an event can be divided into two parts:

- The high-multiplicity and high-energy-density core. When the string density surpasses a certain threshold, strings merge to form QGP, which then hadronizes statistically. Figure 3.1 (right) presents the space-time evolution of the core in EPOS, which basically corresponds to the collective hadronization phase. This phase goes from the primary interaction, in which the initial conditions are created, up to the freeze out, after which the particles do not re-interact. In practice, there is no real phase boundary between the QGP medium and the hadron gas. Although the initial conditions may vary, according to energy, impact parameter, number of multiple scatterings and geometry, the same rules apply from pp to heavy-ion collisions. In fact, the core dominates at mid-rapidity but also extends into the forward region, which is crucial for air shower simulations [63].
- The low-multiplicity and low-energy-density corona. If the string density stays below the threshold, the strings hadronize classically through string fragmentation, with no formation of QGP.

4.2 EPOS-QGP

While QGP effects are included in EPOS-LHC, it has been shown that these appear only for very high-multiplicity events and mostly at mid-rapidity [2]. The core is produced too late compared to what is observed at the LHC and so a modified version of EPOS-LHC that accounts for an extended core, allowing for more visible QGP effects, was created and its called EPOS-QGP. In the phenomenological core-corona model, the particle yield N_i for particle species i is the sum of both contributions:

$$N_i = \omega_{core} N_i^{core} + (1 - \omega_{core}) N_i^{corona}, \tag{4.1}$$

where ω_{core} is the core weight, N_i^{core} is the particle yield if there was only core and N_i^{corona} is the particle yield if there was only corona. It is expected to increase logarithmically with energy and its energy-dependent factor is defined as:

$$F(E_{lab}; E_{th}, E_{scale}) = \frac{\log_{10}(E_{lab}/E_{th})}{\log_{10}(E_{scale}/E_{th})} \tag{4.2}$$

for $E_{lab} > E_{th}$, where E_{lab} is the energy in the laboratory reference frame, E_{th} is the threshold energy above which we have core effects and E_{scale} is a reference energy scale that allows us to play with

the size of the core relative to the size of the corona, marking the energy above which the core weight saturates. The energy dependence is thus modelled by:

$$\omega_{core}(E_{lab}) = f_{\omega} F(E_{lab}; E_{th}, E_{scale}), \tag{4.3}$$

where f_{ω} is a normalization factor that regulates the energy density of the core and its maximum weight. Figure 4.1 (left) presents different possible energy evolutions of the core weight by varying f_{ω} and E_{scale}. Relating this energy-dependence with multiplicity, in order to explain LHC data [60], ω_{core} needs to increase monotonically with the multiplicity, starting from zero for low multiplicity pp scattering, up to 0.5 or more for very high multiplicity pp and reaching unity for central heavy-ion collisions (Pb-Pb). Note that the core and corona yeilds do not depend on the multiplicity itself, but on the fraction of particles produced by the core and the corona, which leads to a smooth transition from corona yield to core yield with multiplicity. Figure 4.1 (right) shows how this energy-dependence of the core weight influences the relation between two shower observables: the number of muons at the ground and the depth of the shower maximum. The EPOS-LHC predicted lines are not encompassed by the experimental data systematic uncertainty area, thus expressing the Muon Puzzle discussed in section 2.4. But we can see from the two panels that a higher core contribution describes the data well.

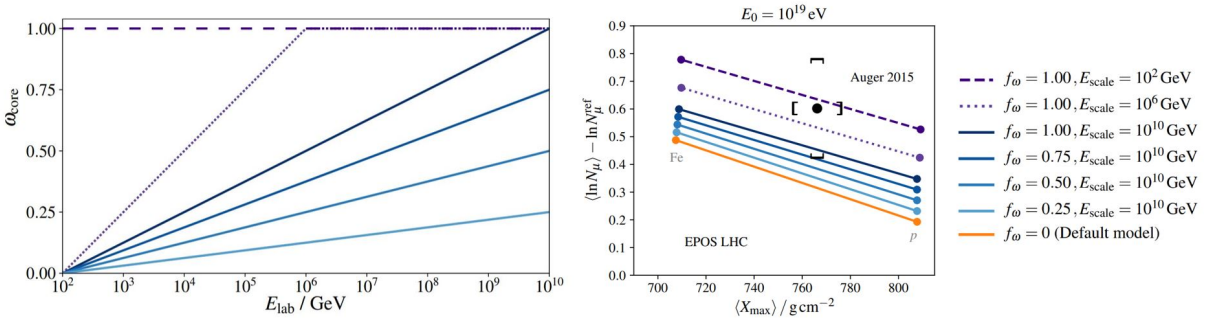

Figure 4.1: **Left**: Energy dependence of the core weight, following equations 4.2 and 4.3, with $E_{th} = 100$ GeV and $F(E_{lab}) = 0$. E_{scale} is changed from 100 GeV to 10^6 GeV and 10^{10} GeV, and f_{ω} is varied by 0.25, 0.5, 0.75 and 1.0. In addition, $F(E_{lab}; E_{th}, E_{scale}) = 1$ is required for all $E_{lab} \geq E_{scale}$. Based on [95]. **Right**: The average logarithm of the number of muons at the ground scaled by a reference $\ln N_{\mu}^{ref}$ as a function of the mean depth of the shower maximum. Different coloured lines show how the energy-dependency of the core weight explored in the left panel affects the relation between the two observables. Each line shows all possible values for any mass composition of 10^{19} eV cosmic rays, between pure proton (bottom right) and pure iron (top left), simulated by hadronic interaction model EPOS-LHC. Data obtained by the Pierre Auger Observatory is shown in black. Based on [63].

Figure 4.2 shows the fraction of particles produced in the core as a function of multiplicity for the two hadronic interaction models, and we can see that in EPOS-QGP more core particles are produced in comparison to corona ones, reaching higher values already in the low-multiplicity region. As seen in section 3.2, the existence of a QGP medium in hadronic interactions leads to an enhancement of strange baryons, effectively deviating energy from the shower electromagnetic sector, i.e. neutral pions. It is easy to see, using the Heitler-Matthews model introduced in section 2.2, that such would effectively

enhance the number of muons produced during the shower development.

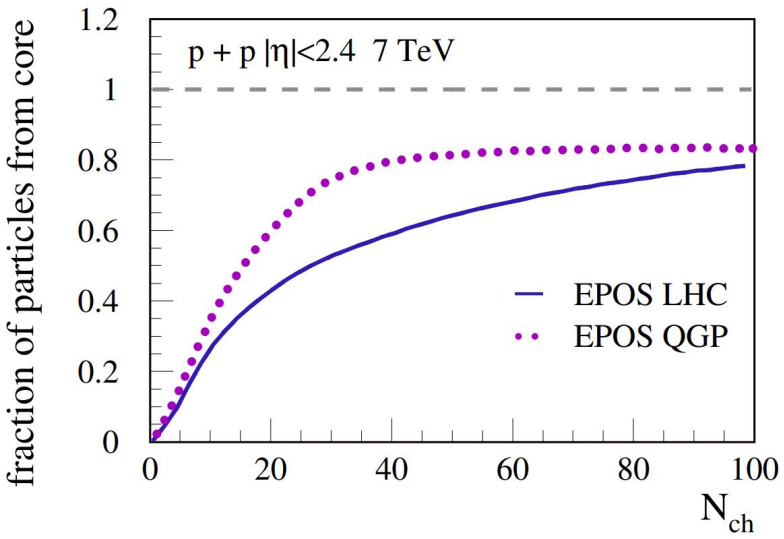

Figure 4.2: Fraction of particles produced by statistical hadronization in the core in function of the charged-particle multiplicity, for a pp collision at $\sqrt{s} = 7$ TeV. The predictions from the hadronic interaction model EPOS-QGP (dotted line) are compared with the ones from EPOS-LHC (full line). Taken from [2].

Chapter 5

QGP impact in hadron interaction quantities

In order to assess the behaviour of the hadronic interaction model EPOS-QGP, we started by looking at the first interaction, which will be explored in this Chapter. Various proton- and iron-induced showers at 10^{19} eV were simulated with this model, along with proton- and iron-induced showers at the same energy using EPOS-LHC for comparison. From here onward, we denominate the proton-induced showers simulated with the hadronic interaction model EPOS-LHC as *EPOS-LHC proton*, the proton-induced showers simulated with hadronic interaction model EPOS-QGP as *EPOS-QGP proton*, the iron-induced showers simulated with hadronic interaction model EPOS-LHC as *EPOS-LHC iron*, and the iron-induced showers simulated with hadronic interaction model EPOS-QGP as *EPOS-QGP iron*. The number of simulated showers is 19800, 100000, 9800 and 10000, and the color code used is green (in dashed lines), magenta (in full lines), orange (in dotted lines) and blue (in mixed lines) for EPOS-LHC proton, EPOS-QGP proton, EPOS-LHC iron and EPOS-QGP iron, respectively.

Figure 5.1 presents the distribution of the total multiplicity of the secondary particles of the first interaction. As discussed in section 2.2, the heavier the primary, the greater the multiplicity, which is what we observe here, with the iron-induced showers showing higher multiplicity values than the proton-induced ones. The EPOS-QGP curves follow the EPOS-LHC ones quite closely, almost overlapping, both for proton- and iron-induced showers. Thus, EPOS-QGP does not seem to alter the multiplicity of the first interaction significantly. Furthermore, looking at the mean abundances of the different particle-types presented in Figure 5.2, all models predict very similar values, as seen in the ratio of their distributions in the lower plot, with neutral and charged pions being the most abundant particles. Other particles are already present in the products of the first interaction, such as photons, neutral and charged kaons, neutrons, protons, electrons, muons, Λ-baryons and their respective antiparticles. Nuclei with a varying number of protons are also present. The lower plot of Figure 5.2 shows that EPOS-QGP proton produces more neutral pions, neutrons, protons, Λ-baryons, antiprotons, $\bar{\Lambda}$-baryons and antineutrons than EPOS-LHC proton, with this increase being always lower than 20$\%$. However, EPOS-QGP proton produces about twice more muons than EPOS-LHC proton. As for the iron-induced showers, EPOS-

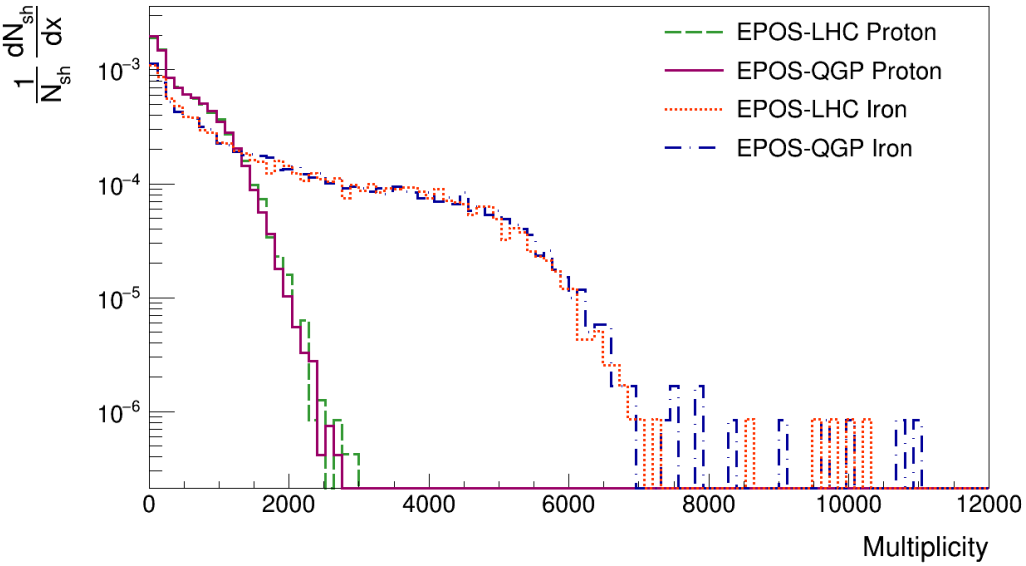

Figure 5.1: Distribution of the multiplicity of the first interaction, normalized by the number of simulated showers N_{sh} for EPOS-LHC iron (orange, dotted line), EPOS-LHC proton (green, dashed line), EPOS-QGP proton (magenta, full line) and EPOS-QGP iron (blue, mixed line) primaries at fixed energy $\log(E/\mathrm{eV}) = 19$.

QGP iron produces more neutrons, protons, antiprotons and antineutrons than EPOS-LHC iron, with this increase being always lower than than 20%. Notwithstanding, EPOS-QGP iron produces approximately 2.5 times more muons than EPOS-LHC iron. Thus, we conclude that EPOS-QGP produces more baryons and antibaryons in the first interaction than EPOS-LHC, which is aligned with the baryon enhancement effect of QGP discussed in section 3.2, and already at least twice more muons, which is aligned with a possible solution to solve the Muon Puzzle introduced in section 2.4.

Since we aimed to move to the centre-of-mass frame of the interaction, we looked at a crucial quantity: momentum. We studied the secondary particles momentum along x, y and z, with their distributions normalized by the total number of secondary particles from all simulated showers being presented in Figures 5.3 (left) and (right) and 5.4 for p_x, p_y and p_z, respectively. One can see that practically all of the particles' momentum is positive and along z, which confirms that the shower develops along this direction. In fact, the distributions of the momentum along the x- and y-directions for all models peak at zero and mostly vary between -2 and 2 GeV/c, which are negligible values compared to the 10^{10} GeV of the incoming particle. Furthermore, we can see from Figure 5.4 that the z-momentum of the secondary particles ranges from 0 to 10^{10} GeV/c, confirming that all their momentum is indeed in the z-direction. Both for iron- and proton-induced showers, EPOS-QGP presents a very similar distribution to EPOS-LHC, with their curves overlapping, apart the small fluctuations. Hence, EPOS-QGP does not seem to significantly alter the momentum distribution of the secondary particles.

One important aspect of an interaction is the conservation of momentum. As a matter of fact, as already mentioned, the incoming particle has an energy of 10^{10} GeV and its momentum can be calculated through the following equation:

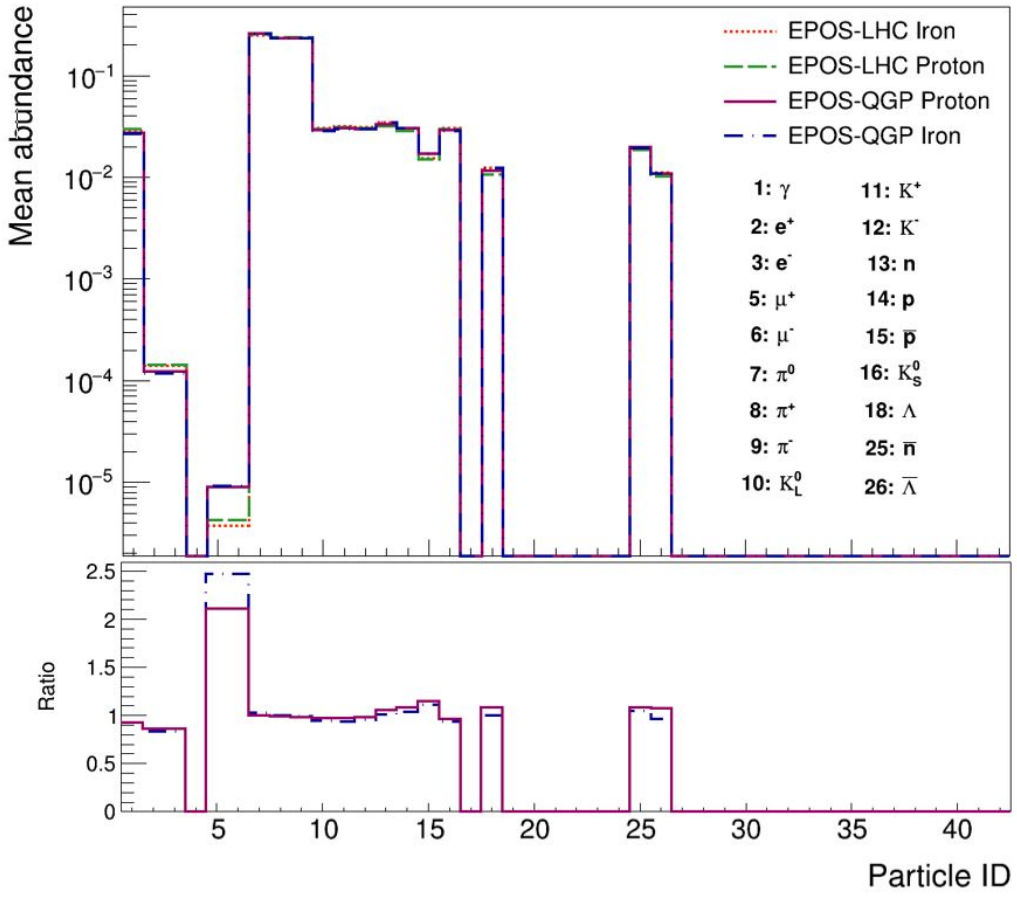

Figure 5.2: Mean abundance of the particles produced in the first interaction for EPOS-LHC iron (orange, dotted line), EPOS-LHC proton (green, dashed line), EPOS-QGP proton (magenta, full line) and EPOS-QGP iron (blue, mixed line) primaries at fixed energy $\log(E/\mathrm{eV}) = 19$. The CORSIKA numbering system is presented for an easier reading. The lower plot presents the ratios of EPOS-QGP proton (magenta, full line) with respect to EPOS-LHC proton and of EPOS-QGP iron (blue, mixed line) with respect to EPOS-LHC iron.

$$E^2 = P^2 + m^2, \tag{5.1}$$

where E is the energy of the particle, P is its momentum and m is its mass, all in natural units. Since the mass of the incoming particle is approximately 0.938272 GeV/c^2 for a proton primary or 52.019288 GeV/c^2 for an iron primary, its momentum can be well approximated by the value of its energy. Therefore one can say its momentum is 10^{10} GeV/c. By momentum conservation, the sum of the momentum of the secondary particles, for each event, should be 10^{10} GeV/c along the z direction and zero along the x and y directions. From Figures 5.3 (left) and (right) one can see that this is the case for the x- and y-momenta, since both distributions are symmetrical and centered around zero. However, Figure 5.5 shows the relative difference between the incoming particle's momentum along z and the sum of the secondary particles momentum also along z, normalized by the number of simulated showers, and one can see that it is not always zero. It varies mostly between -0.0001 and 0.0001 GeV/c with respect to the momentum of the incoming particle along z for the iron-induced showers and between -0.0002 and

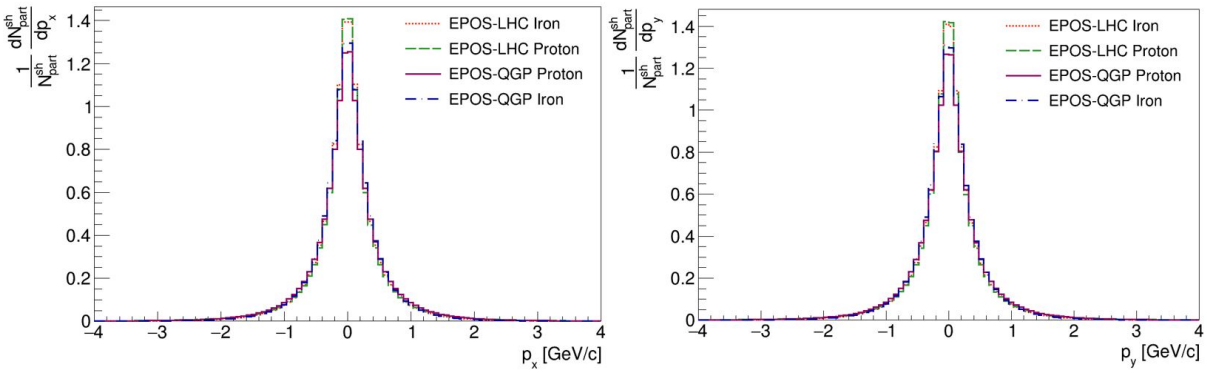

Figure 5.3: Distribution of the x-momentum (**left**) and of the y-momentum (**right**) of the secondary particles in the laboratory reference frame, normalized by the total number of secondary particles from all simulated showers N_{part}^{sh} for EPOS-LHC iron (orange, dotted line), EPOS-LHC proton (green, dashed line), EPOS-QGP proton (magenta, full line) and EPOS-QGP iron (blue, mixed line) primaries at fixed energy $\log(E/\mathrm{eV}) = 19$.

0.0002 GeV/c for the proton-induced showers, peaking at zero for all models. This energy violation is not relevant in the cosmic ray first interaction picture, or in other words, in the laboratory reference frame, since the incoming particle is an ultra-high energy one with an energy of four orders of magnitude higher than the discrepancy values. However, when we turn to the centre-of-mass frame of the interaction, where both the incoming particle and the air nucleus are colliding along the z-direction with equal but opposite momenta, it becomes a problem, since this energy violation is all along the boost direction.

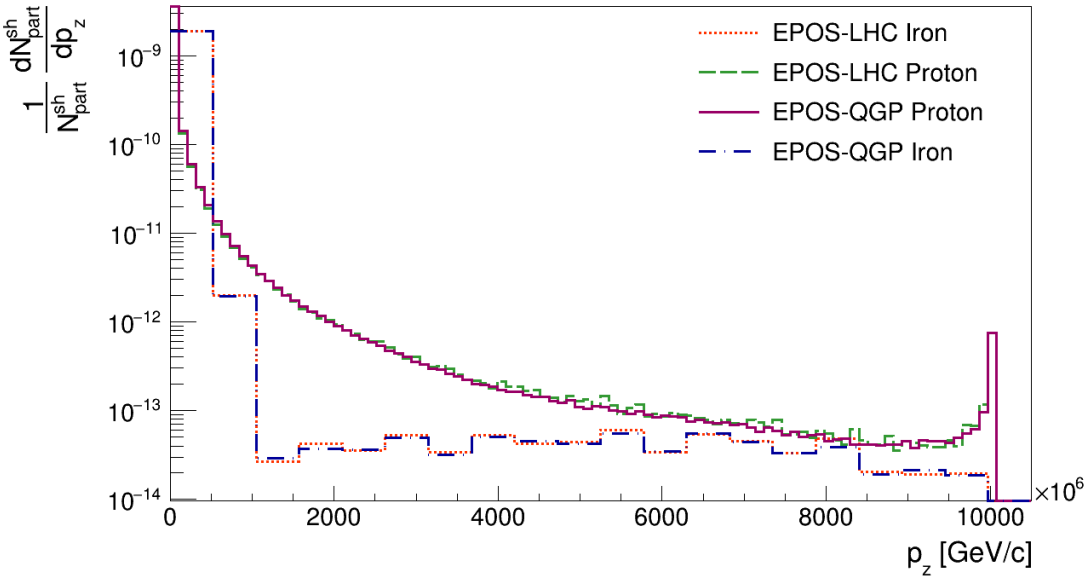

Figure 5.4: Distribution of the z-momentum of the secondary particles in the laboratory reference frame, normalized by the total number of secondary particles from all simulated showers N_{part}^{sh} for EPOS-LHC iron (orange, dotted line), EPOS-LHC proton (green, dashed line), EPOS-QGP proton (magenta, full line) and EPOS-QGP iron (blue, mixed line) primaries at fixed energy $\log(E/\mathrm{eV}) = 19$.

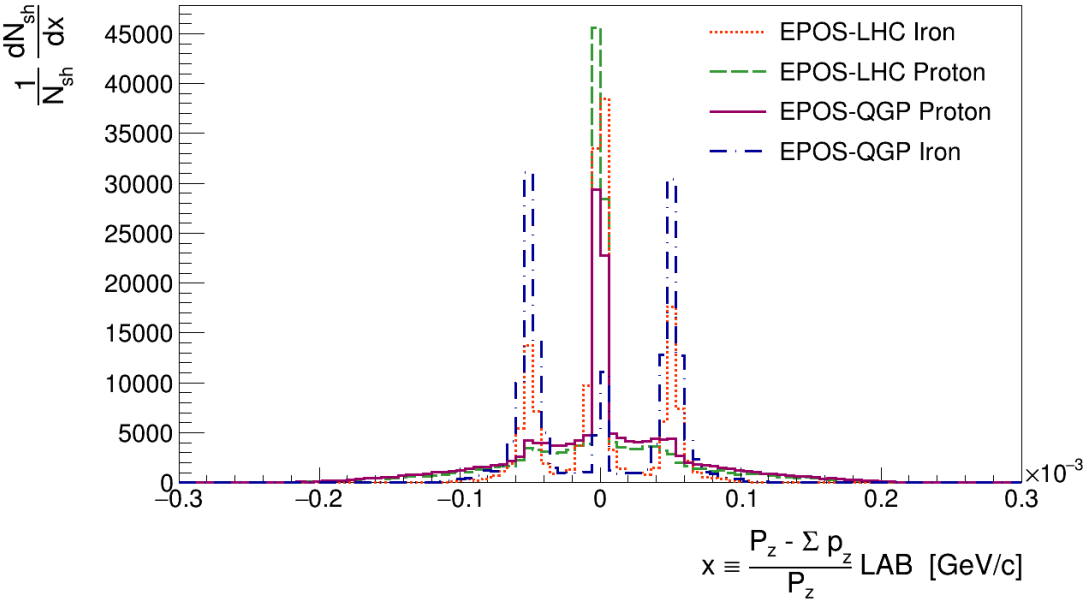

Figure 5.5: Distribution of the difference between the z-momentum of the incoming particle P_z and the sum of the z-momentum of the secondary particles produced in the first interaction Σp_z, normalized by the number of simulated showers N_{sh} for EPOS-LHC iron (orange, dotted line), EPOS-LHC proton (green, dashed line), EPOS-QGP proton (magenta, full line) and EPOS-QGP iron (blue, mixed line) primaries at fixed energy $\log(E/\mathrm{eV}) = 19$.

The change of frames is performed via a Lorentz transformation in the z-direction, according to the following equations:

$$E^{CM} = \gamma E^{LAB} - \gamma\beta P_z^{LAB}, \tag{5.2}$$

$$P_z^{CM} = \gamma P_z^{LAB} - \gamma\beta E^{LAB}, \tag{5.3}$$

with

$$\beta = \frac{P_p}{E_p + m_{air}}, \tag{5.4}$$

$$\gamma = \frac{E_p + m_{air}}{\sqrt{s}}, \tag{5.5}$$

in which E is the energy of the particle and P_z is its z-momentum. E_p is the energy of the incoming particle, P_p is its momentum and m_{air} is the mass of the air nucleus (nitrogen). $\sqrt{s}$ is the centre-of-mass energy of the interaction. Knowing that equations 5.2 and 5.3 apply to each secondary particle i, in order to overcome the energy violation found in the laboratory reference frame, we must force energy conservation in the centre-of-mass frame by rewriting equations 5.4 and 5.5 in terms of the secondary particles:

$$\sum_i P_{z,i}^{CM} = 0 \Longleftrightarrow \beta = \frac{\sum_i P_{z,i}^{LAB}}{\sum_i E_i^{LAB}} \tag{5.6}$$

$$\sum_i E_{z,i}^{CM} = \sqrt{s} \iff \gamma = \frac{\sum_i E_i^{LAB}}{\sqrt{s}}, \tag{5.7}$$

where $P_{z,i}^{LAB}$ is the z-momentum of the secondary particle i in the laboratory reference frame, E_i^{LAB} is its energy also in the laboratory reference frame and $\sqrt{s}$ is given by:

$$s = (\sum_i E_i^{LAB})^2 - (\sum_i P_{x,i}^{LAB})^2 - (\sum_i P_{y,i}^{LAB})^2 - (\sum_i P_{z,i}^{LAB})^2, \tag{5.8}$$

with $P_{y,i}^{LAB}$ and $P_{x,i}^{LAB}$ being the the x- and y-momenta of the secondary particle i in the laboratory reference frame. Equations 5.2 and 5.3 are thus rewritten as:

$$E^{CM} = \frac{1}{\sqrt{s}} \left[E^{LAB} \sum_i E_i^{LAB} - P_z^{LAB} \sum_i p_{z,i}^{LAB} \right], \tag{5.9}$$

$$P_z^{CM} = \frac{1}{\sqrt{s}} \left[P_z^{LAB} \sum_i E_i^{LAB} - E^{LAB} \sum_i p_{z,i}^{LAB} \right]. \tag{5.10}$$

From Figure 5.6, which shows the distribution of the sum of the z-momentum of the secondary particles normalized by the number of simulated showers, we see that the z-momentum is conserved in the center-of-mass frame. Since the parent particles have equal but opposite momenta in this frame, the sum of the secondary particles momentum along each direction should be zero. In fact, the distribution peaks at zero and reaches values compatible with zero (of the order of 10^{-52} GeV/c), for all models. The precision of this result was made possible by the use of the data type *cpp_dec_float_50* from the *Boost.Multiprecision* library, which was required because of how dangerously close the velocity ratio β was to 1.

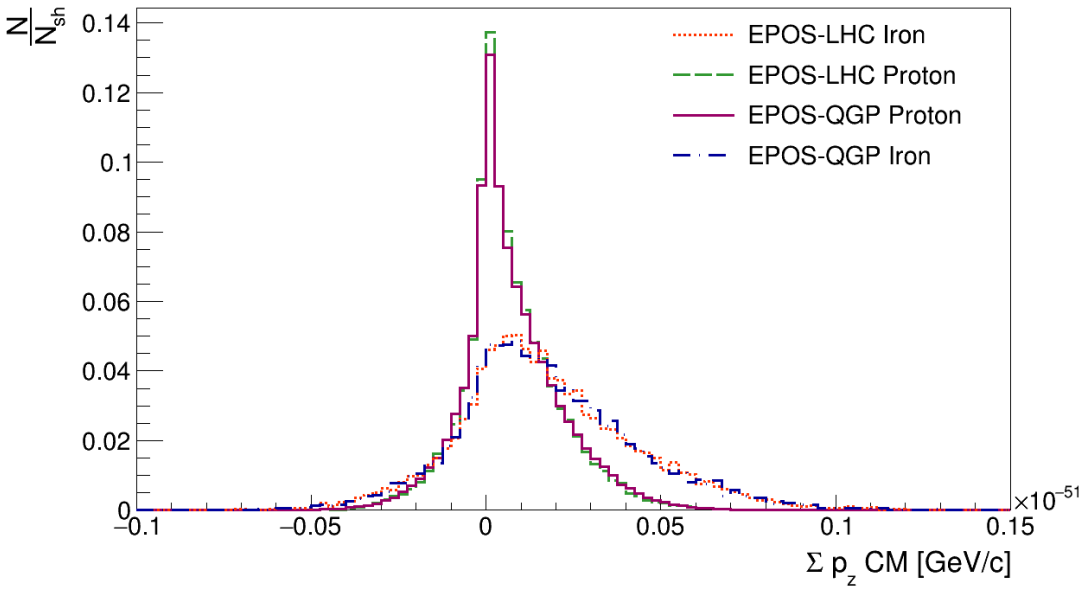

Figure 5.6: Distribution of the sum of the z-momentum of the secondary particles in the center-of-mass frame, normalized by the number of simulated showers N_{sh} for EPOS-LHC iron (orange, dotted line), EPOS-LHC proton (green, dashed line), EPOS-QGP proton (magenta, full line) and EPOS-QGP iron (blue, mixed line) primaries at fixed energy $\log(E/\mathrm{eV}) = 19$.

The distribution of the z-momentum of the secondary particles of the first interaction, calculated using equation 5.10 and normalized by the total number of secondary particles from all simulated showers is exhibited in Figure 5.7. The distribution is asymmetrical for the proton-induced showers, since the colliding system (p-A) is itself asymmetrical. Considering that heavier primaries produce more secondary particles that must share among themselves the energy of the parent particles, the z-momentum of the secondary particles for the iron-induced showers should be lower. Indeed, the iron-induced showers show a more symmetrical distribution and less particles with higher values of p_z than the proton-induced ones. In both cases, the EPOS-QGP curve behaves similarly to the EPOS-LHC one. Hence, EPOS-QGP does not seem to alter the z-momentum of the secondary particles in the center-of-mass frame significantly.

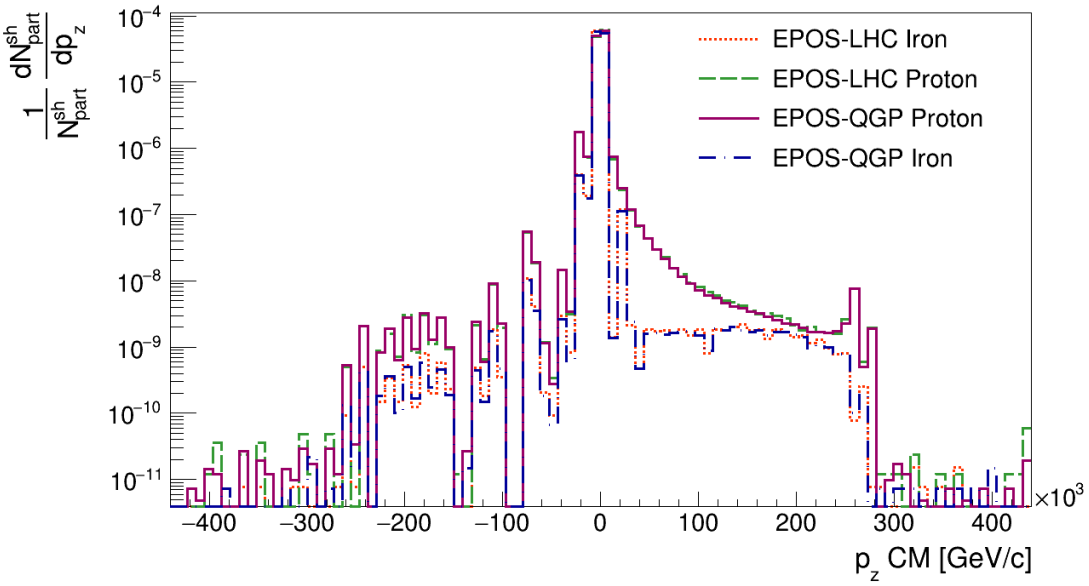

Figure 5.7: Distribution of the z-momentum of the secondary particles in the center-of-mass frame, normalized by the total number of secondary particles from all simulated showers N^{sh}_{part} for EPOS-LHC iron (orange, dotted line), EPOS-LHC proton (green, dashed line), EPOS-QGP proton (magenta, full line) and EPOS-QGP iron (blue, mixed line) primaries at fixed energy $\log(E/\mathrm{eV}) = 19$.

In order to compare our findings with the existing accelerator data, especially with LHC data, we looked at the p_T distributions of the secondary particles and at their pseudo-rapidities. Figure 5.8 displays the distribution of the transverse momentum of the secondary particles of the first interaction in the center-of-mass frame, normalized by the total number of secondary particles from all simulated showers. The transverse momentum is calculated through the following equation:

$$p_T = \sqrt{p_x^2 + p_y^2}. \tag{5.11}$$

Despite the fact that all models peak at zero and then attenuate as p_T grows, which means all models have more low-p_T particles than high-p_T ones, the iron-induced showers show a narrower and lower-valued distribution. This makes sense, since, once more, heavier primaries produce more secondary particles that must share among themselves the energy of the parent particles, hence presenting lower

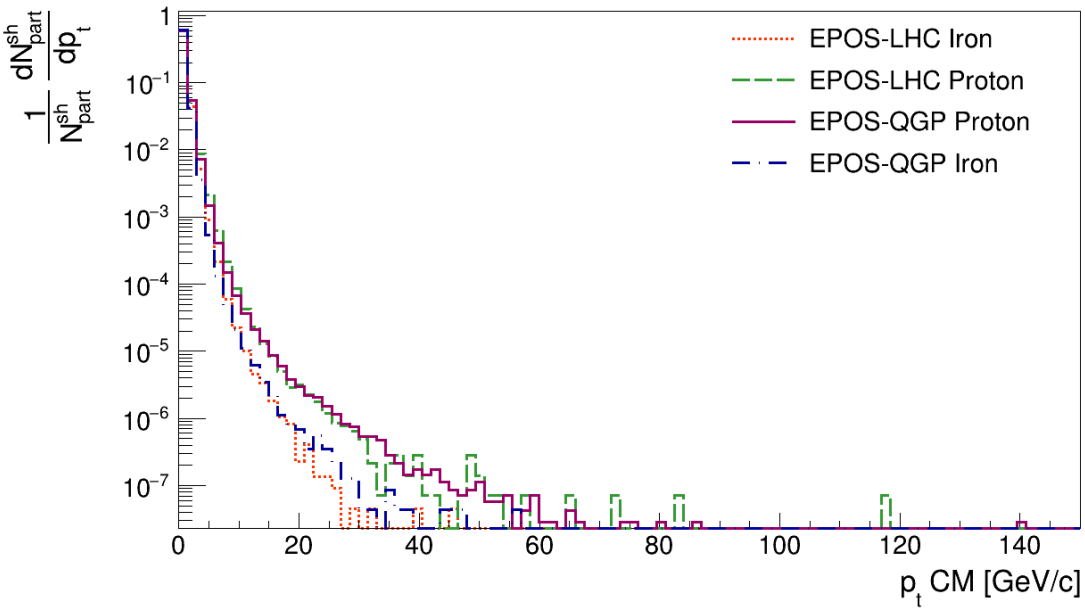

Figure 5.8: Distribution of the transverse momentum of the secondary particles, according to equation 5.11, in the center-of-mass frame, normalized by the total number of secondary particles from all simulated showers N^{sh}_{part} for EPOS-LHC iron (orange, dotted line), EPOS-LHC proton (green, dashed line), EPOS-QGP proton (magenta, full line) and EPOS-QGP iron (blue, mixed line) primaries at fixed energy $\log(E/\mathrm{eV}) = 19$.

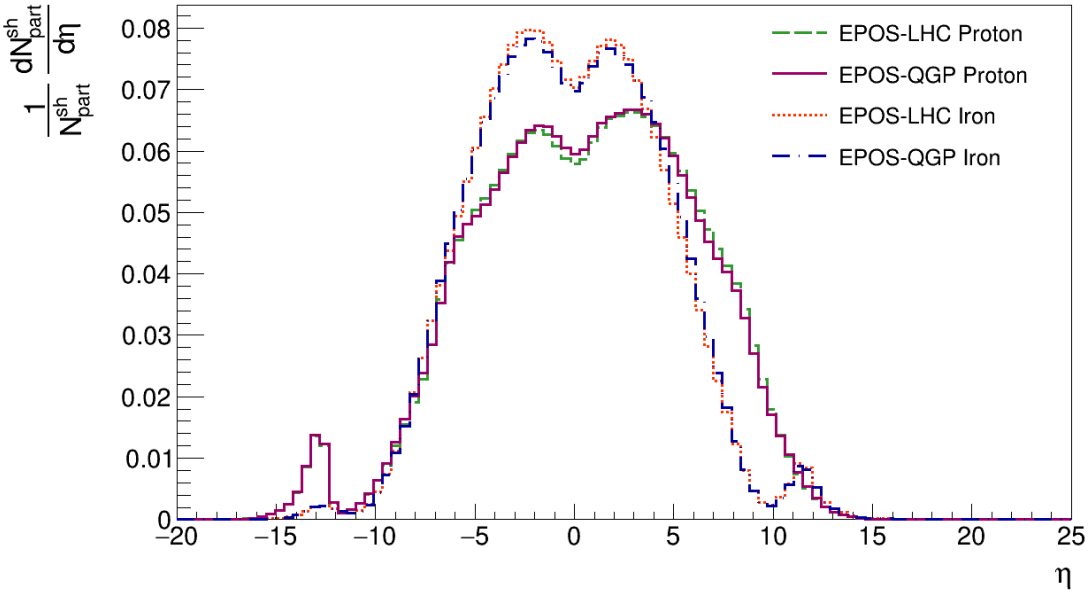

Figure 5.9: Distribution of the pseudo-rapidity of the secondary particles in the center-of-mass frame, normalized by the total number of secondary particles from all simulated showers N^{sh}_{part} for EPOS-LHC iron (orange, dotted line), EPOS-LHC proton (green, dashed line), EPOS-QGP proton (magenta, full line) and EPOS-QGP iron (blue, mixed line) primaries at fixed energy $\log(E/\mathrm{eV}) = 19$.

energy values. Both for the proton- and iron-induced showers, the EPOS-QGP curve follows the EPOS-LHC one very closely. Figure 5.9 presents the distribution of the pseudo-rapidity of each secondary particle calculated through the following equation:

$$\eta = -\ln\left[tan\left(\frac{\theta}{2}\right)\right], \tag{5.12}$$

with θ being the angle of each secondary particle in relation to the beam axis in the center-of-mass frame calculated through the following expression:

$$\theta = \arctan\left(\frac{p_T}{p_z}\right), \tag{5.13}$$

where p_T and p_z are the transverse and z-momenta of each secondary particle in the center-of-mass frame. As expected, all models present the majority of the secondary particles in the $-5 < \eta < 5$ region. Both for proton- and iron-induced showers, EPOS-QGP shows nearly identical behaviour to EPOS-LHC. The peaks in the end of both tails are produced by the most forward particles that interact diffractively. We performed pseudo-rapidity cuts in momentum, multiplicity and particle type distributions, focusing on the $-2 < \eta < 2$ and $-0.5 < \eta < 0.5$ regions, where the bulk of the produced particles is concentrated. We also studied the nuclear modification factor dependence on transverse momentum in the regions of the cuts.

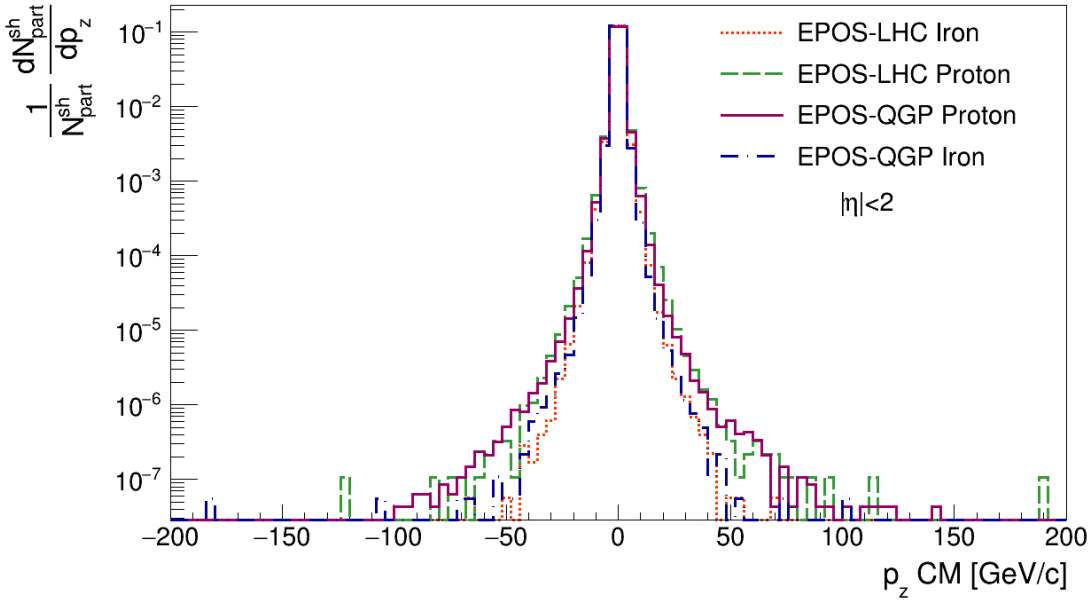

Figure 5.10: Distribution of the z-momentum of the secondary particles in the center-of-mass frame and in the pseudo-rapidity range $-2 < \eta < 2$ for EPOS-LHC iron (orange, dotted line), EPOS-LHC proton (green, dashed line), EPOS-QGP proton (magenta, full line) and EPOS-QGP iron (blue, mixed line) primaries at fixed energy $\log(E/\mathrm{eV}) = 19$. The distribution is normalized by the total number of secondary particles from all simulated showers N^{sh}_{part} in the same pseudo-rapidity region.

Beginning with the $-2 < \eta < 2$ pseudo-rapidity cut, we looked at the distributions of the z- and transverse momenta in the centre-of-mass frame, both normalized by the total number of secondary particles from all simulated showers and presented in Figures 5.10 and 5.11, respectively. We can see that, for the momentum along z, all models present a somewhat symmetric distribution centered and peaked at zero, contrary to what was seen in Figure 5.7. The iron-induced showers have a slightly narrower

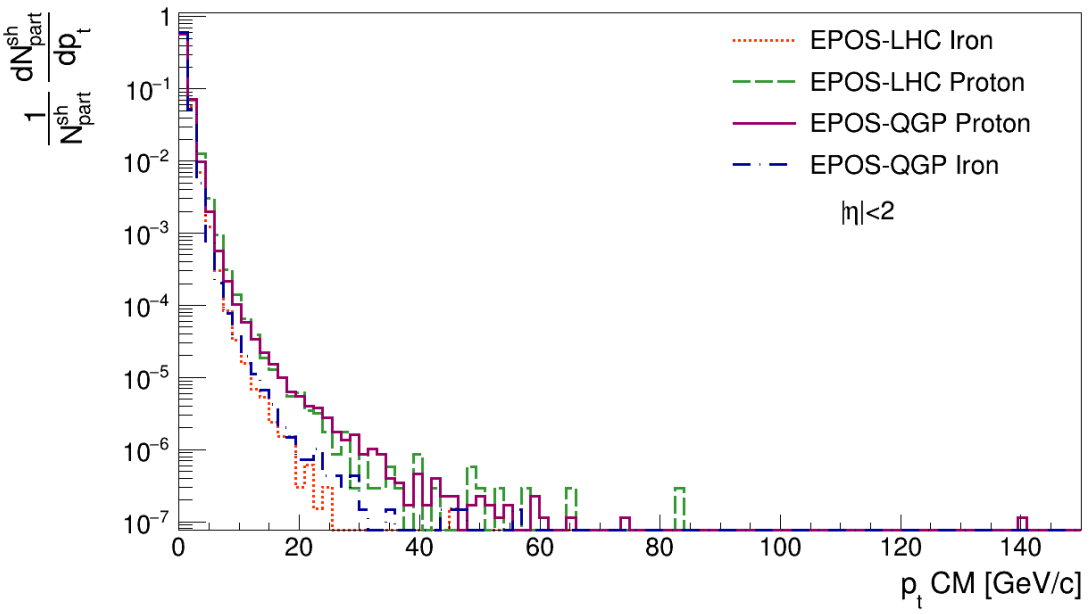

Figure 5.11: Distribution of the transverse momentum of the secondary particles in the center-of-mass frame and in the pseudo-rapidity range $-2 < \eta < 2$ for EPOS-LHC iron (orange, dotted line), EPOS-LHC proton (green, dashed line), EPOS-QGP proton (magenta, full line) and EPOS-QGP iron (blue, mixed line) primaries at fixed energy $\log(E/\mathrm{eV}) = 19$. The distribution is normalized by the total number of secondary particles from all simulated showers N_{part}^{sh} in the same pseudo-rapidity region.

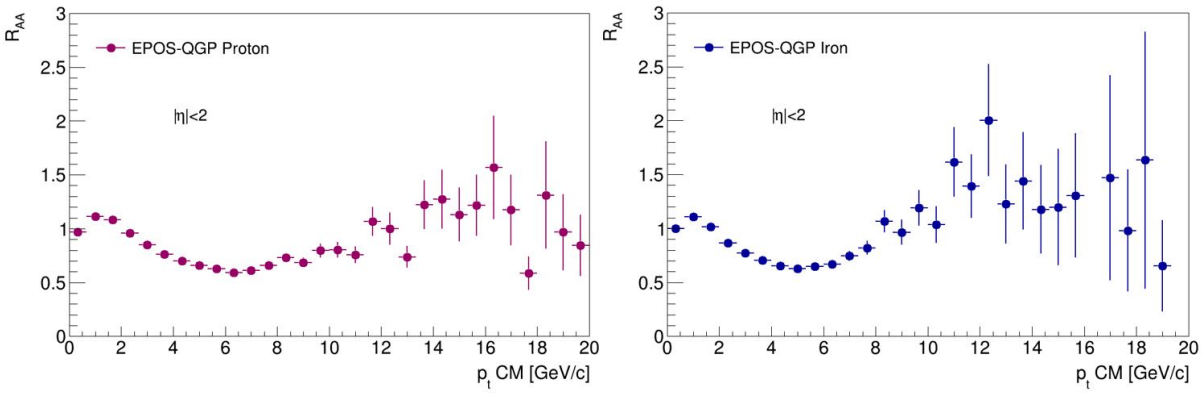

Figure 5.12: Nuclear modification factor dependence on the center-of-mass transverse momentum of the secondary particles, calculated for EPOS-QGP proton with respect to EPOS-LHC proton (**left**) and for EPOS-QGP iron with respect to EPOS-LHC iron (**right**), in the pseudo-rapidity region $-2 < \eta < 2$, for primaries with fixed energy $\log(E/\mathrm{eV}) = 19$.

distribution compared to the proton-induced ones, but in both cases the EPOS-QGP curve shows a similar behaviour to the EPOS-LHC one. As for the transverse momentum, the models exhibit the same behaviour they did without the pseudo-rapidity cut (see Figure 5.8), except that now the distributions are narrower and more concentrated in the lower-p_T region. Figure 5.12 presents the nuclear modification factor dependence on the transverse momentum, calculated for EPOS-QGP proton with respect to EPOS-LHC proton (left), and for EPOS-QGP iron with respect to EPOS-LHC iron (right). For both cases, the procedure was the following: both EPOS-QGP and EPOS-LHC p_T distributions were scaled

by their respective number of simulated showers and then the ratio of these quantities was performed. Compared to Figure 3.5, our nuclear modification factors present the expected behaviour, with an initial growth followed by a descending curve that afterwards grows again. However, its values are different since our colliding systems are less dense and thus QGP-like effects are expected to be smaller. In fact, the low-p_T particles have an R_{AA} equal or a bit higher than 1 and the high-p_T particles have an R_{AA} smaller than one, apart from the fluctuations in the tail, for both the iron- and the proton-induced showers. We can thus conclude that in both cases EPOS-QGP presents more particles with a low-p_T than with a higher p_T, when compared to EPOS-LHC, which might be aligned with the energy loss caused by jet-quenching, associated with the presence of a QGP medium, although the effects are very light.

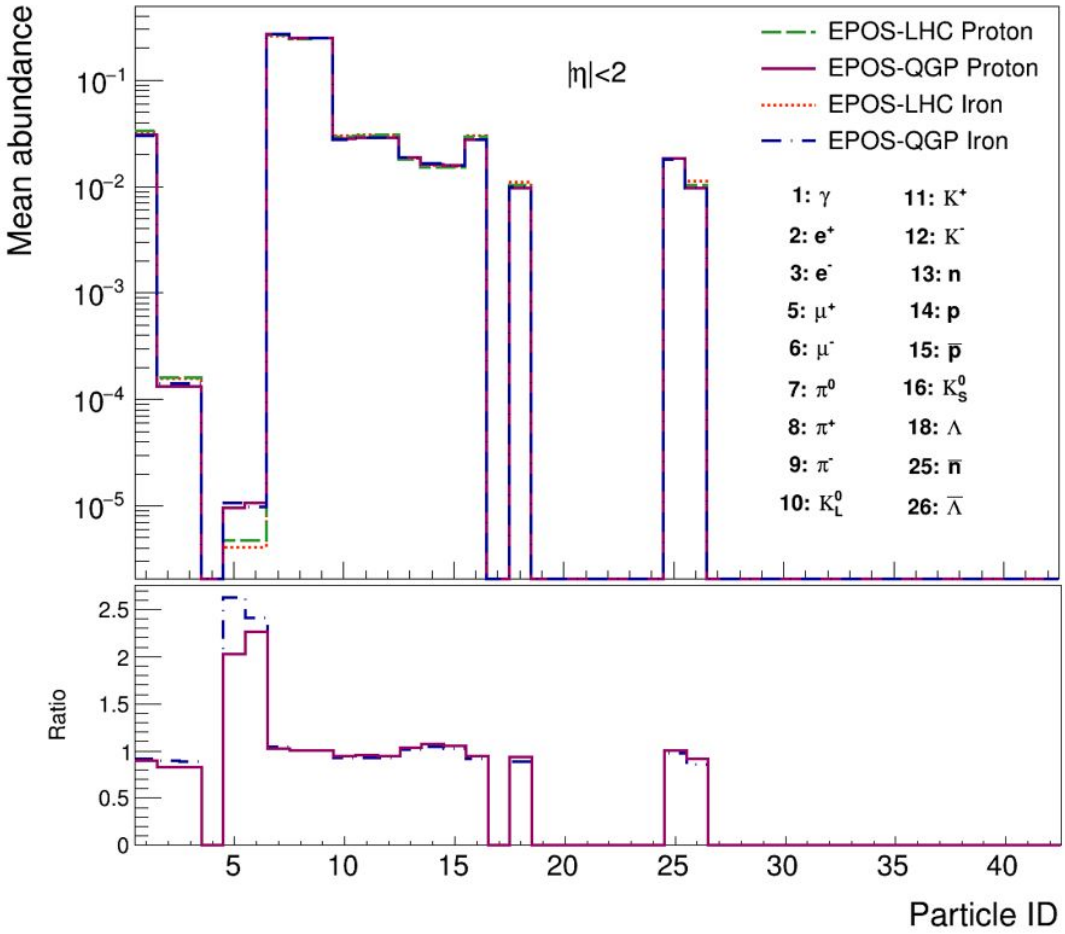

Figure 5.13: Mean abundance of the particles produced in the first interaction in the pseudo-rapidity region $-2 < \eta < 2$, for EPOS-LHC iron (orange, dotted line), EPOS-LHC proton (green, dashed line), EPOS-QGP proton (magenta, full line) and EPOS-QGP iron (blue, mixed line) primaries at fixed energy $\log(E/\mathrm{eV}) = 19$. The CORSIKA numbering system is presented for an easier reading. The lower plot presents the ratios of EPOS-QGP proton (magenta, full line) with respect to EPOS-LHC proton and of EPOS-QGP iron (blue, mixed line) with respect to EPOS-LHC iron.

Figure 5.13 presents the mean abundance of the different types of particles produced in the first interaction, within the pseudo-rapidity cut $-2 < \eta < 2$, for all models. All the particle types that were present in the no pseudo-rapidity cut distribution (see Figure 5.2) are also present here. As seen in

the ratios shown in the lower plot, EPOS-QGP presents similar values to EPOS-LHC, for both iron- and proton-induced showers. However, EPOS-QGP proton does produce approximately 10% more protons and antiprotons and about 80% more muons than EPOS-LHC proton. As for the iron case, EPOS-QGP iron produces around 10% more π^0 and protons and approximately 3.3 times more muons. Thus, the conclusion withdrawn from the results of Figure 5.2 still holds for the pseudo-rapidity region $-2 < \eta < 2$: EPOS-QGP produces more baryons and already more muons in the first interaction than EPOS-LHC, which is aligned with the baryon enhancement effect of QGP and with a possible solution to the Muon Puzzle.

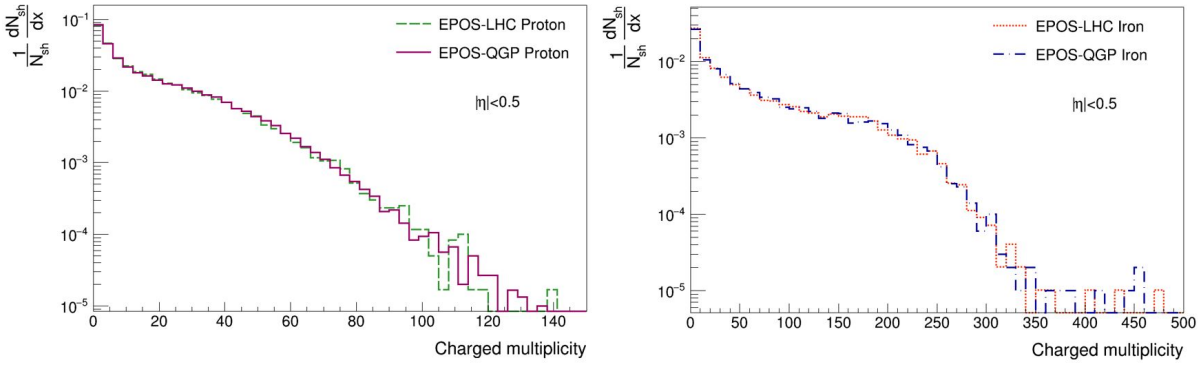

Figure 5.14: Distribution of the charged-particle multiplicity of the first interaction in the pseudo-rapidity region $-0.5 < \eta < 0.5$, normalized by the number of simulated showers N_{sh} for EPOS-LHC proton (green, dashed line) and EPOS-QGP proton (magenta, full line) (**left**), and for EPOS-LHC iron (orange, dotted line) and EPOS-QGP iron (blue, mixed line) (**right**) primaries at fixed energy $\log(E/\mathrm{eV}) = 19$.

We now turn to the results obtained within the pseudo-rapidity cut of $-0.5 < \eta < 0.5$, which were performed for proton- and iron-induced showers separately, in order to directly compare the results of the two hadronic interaction models with the same colliding system. In this case, we want to assess how EPOS-QGP deals with the charged and strange particles produced in the collision.

Figure 5.14 displays the distribution of the multiplicity of the charged secondary particles normalized by the the number of simulated showers, for the proton- (left) and the iron-induced showers (right). The iron-induced showers present a higher charged-particle multiplicity and its distribution has a similar shape to the one found in Figure 5.1. In both proton- and iron-induced showers, EPOS-QGP shows a similar behaviour to EPOS-LHC, presenting more first interactions with a lower number of produced charged particles than with a higher number. Figure 5.15 shows, on the left side, the distribution of the centre-of-mass transverse momentum of the secondary $\pi^{\pm}$ normalized by the number of simulated showers and, on the right side, the corresponding R_{AA} values as a function of the transverse momentum, for the proton-induced showers. Figure 5.16 does the same, but for the iron-induced showers. These nuclear modification factors were calculated through the same procedure described for Figure 5.12. In both the proton and iron cases, EPOS-QGP follows the behaviour of EPOS-LHC closely, presenting slightly lower values for higher-p_T. In fact, the R_{AA} of the charged pions is around one for the region with the highest number of particles, assuming in general, the value one or lower for higher p_T, aside from the final fluctuations, both for the proton- and iron-induced showers. Note that these R_{AA} shapes

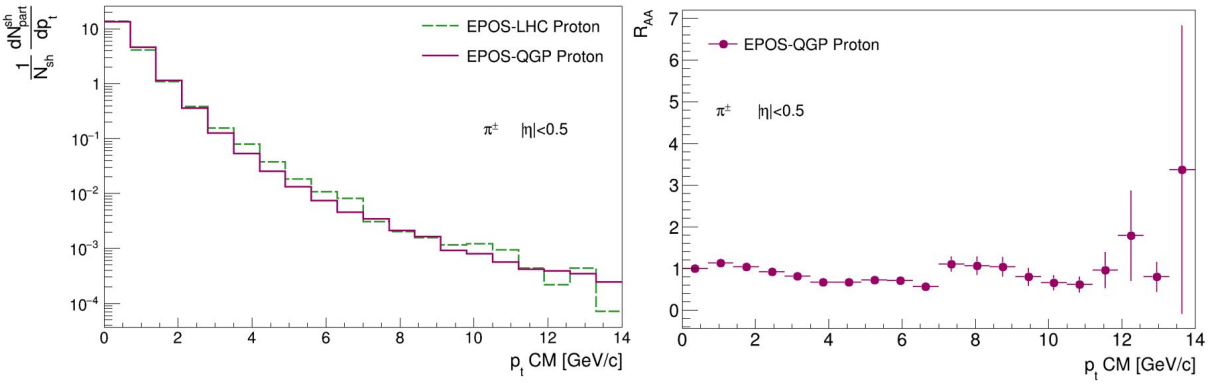

Figure 5.15: **Left**: Distribution of the transverse momentum of the secondary $\pi^{\pm}$ particles in the center-of-mass frame and in the pseudo-rapidity region $-0.5 < \eta < 0.5$, normalized by the number of simulated showers N_{sh} for EPOS-LHC proton (green, dashed line) and EPOS-QGP proton (magenta, full line) primaries at fixed energy $\log(E/\mathrm{eV}) = 19$. **Right**: Nuclear modification factor dependence on the center-of-mass transverse momentum of the secondary $\pi^{\pm}$ particles, calculated for EPOS-QGP proton with respect to EPOS-LHC proton in the same pseudo-rapidity region and for the same energy.

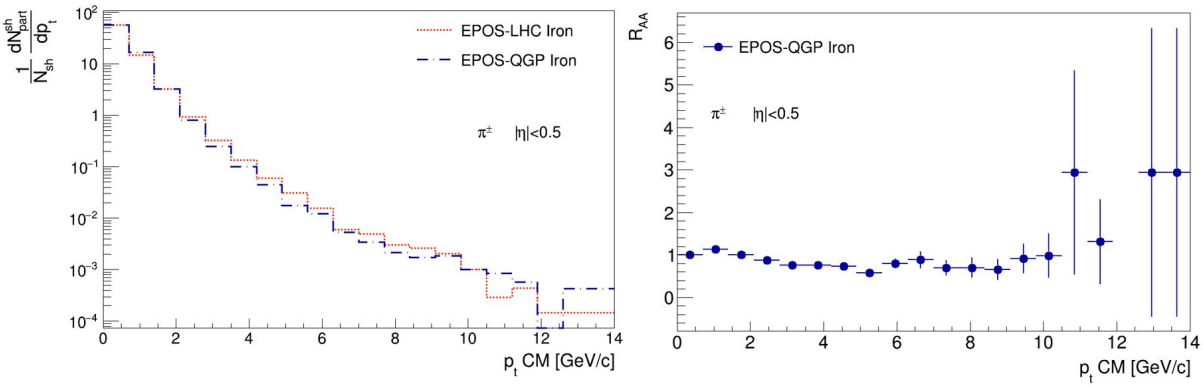

Figure 5.16: **Left**: Distribution of the transverse momentum of the secondary $\pi^{\pm}$ particles in the center-of-mass frame and in the pseudo-rapidity region $-0.5 < \eta < 0.5$, normalized by the number of simulated showers N_{sh} for EPOS-LHC iron (orange, dotted line) and EPOS-QGP iron (blue, mixed line) primaries at fixed energy $\log(E/\mathrm{eV}) = 19$. **Right**: Nuclear modification factor dependence on the center-of-mass transverse momentum of the secondary $\pi^{\pm}$ particles, calculated for EPOS-QGP iron with respect to EPOS-LHC iron in the same pseudo-rapidity region and for the same energy.

are very flat, when compared to the ones from Figure 5.12 or even from Figure 3.5.

Figure 5.17 shows, on the left side, the distribution of the centre-of-mass transverse momentum of the secondary K^0_S normalized by the number of simulated showers and, on the right side, the corresponding R_{AA} values as a function of the transverse momentum, for the proton-induced showers. Figure 5.18 presents the same, but for the iron-induced showers. Once again, these nuclear modification factors were calculated through the same procedure described for Figure 5.12. In both the proton and iron cases, the p_T distribution of EPOS-QGP has the same behavioural trend as EPOS-LHC, but shows slightly lower values for higher-p_T. The R_{AA} behaviour in function of the transverse momentum confirms this: starting at around one, the nuclear modification factors grow, only to decrease again to the previous

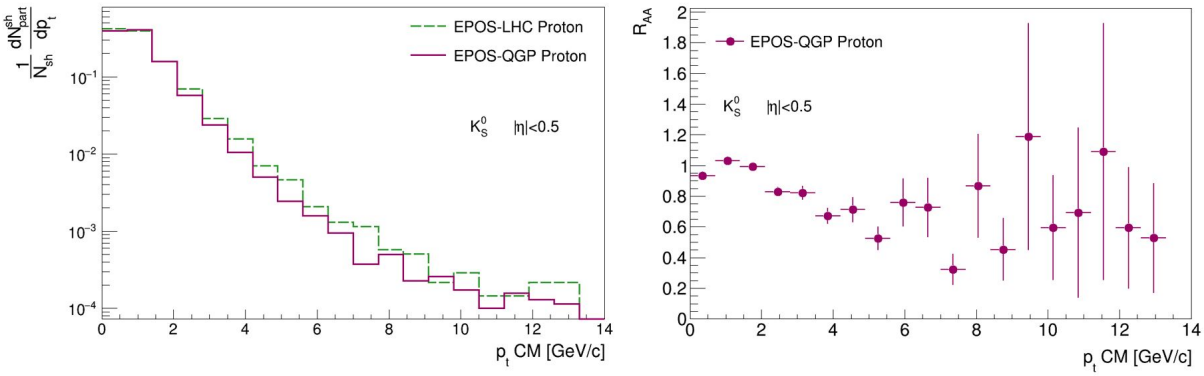

Figure 5.17: **Left**: Distribution of the transverse momentum of the secondary K^0_S particles in the center-of-mass frame and in the pseudo-rapidity region $-0.5 < \eta < 0.5$, normalized by the number of simulated showers N_{sh} for EPOS-LHC proton (green, dashed line) and EPOS-QGP proton (magenta, full line) primaries at fixed energy $\log(E/\mathrm{eV}) = 19$. **Right**: Nuclear modification factor dependence on the center-of-mass transverse momentum of the secondary K^0_S particles, calculated for EPOS-QGP proton with respect to EPOS-LHC proton in the same pseudo-rapidity region and for the same energy.

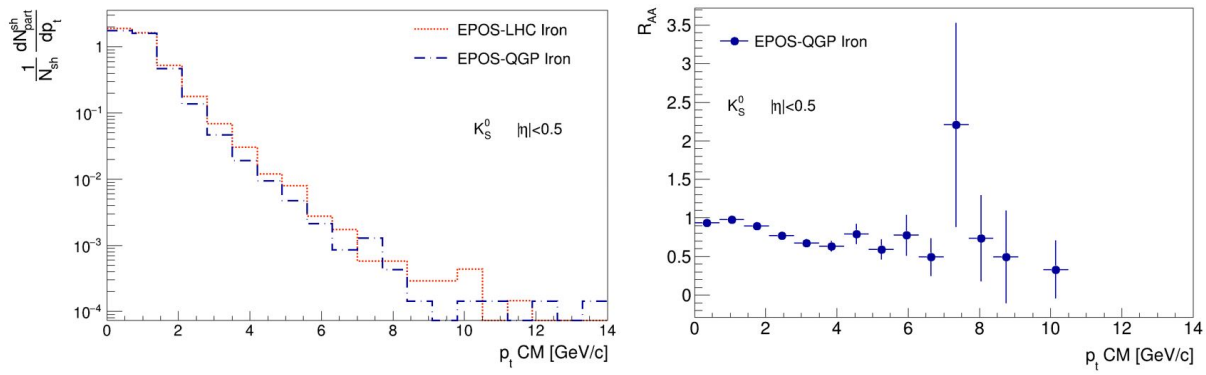

Figure 5.18: **Left**: Distribution of the transverse momentum of the secondary K^0_S particles in the center-of-mass frame and in the pseudo-rapidity region $-0.5 < \eta < 0.5$, normalized by the number of simulated showers N_{sh} for EPOS-LHC iron (orange, dotted line) and EPOS-QGP iron (blue, mixed line) primaries at fixed energy $\log(E/\mathrm{eV}) = 19$. **Right**: Nuclear modification factor dependence on the center-of-mass transverse momentum of the secondary K^0_S particles, calculated for EPOS-QGP iron with respect to EPOS-LHC iron in the same pseudo-rapidity region and for the same energy.

value or below it, aside from the fluctuations in the end. Figure 5.19 exhibits, on the left side, the distribution of the centre-of-mass transverse momentum of the secondary Λ+$\bar{\Lambda}$ baryons normalized by the number of simulated showers and, on the right side, the corresponding R_{AA} values as a function of the transverse momentum, for the proton-induced showers. Figure 5.20 presents the same but for the iron-induced showers. Once again, these nuclear modification factors were calculated through the same procedure described for Figure 5.12. In both the proton and iron cases, the p_T distribution of EPOS-QGP has the same behavioural trend as EPOS-LHC, but shows slightly lower values for higher-p_T. However, the R_{AA} behaviour is a bit different, for the proton- and iron-induced showers. In the former, the R_{AA} shape is the expected one, starting below one, growing slightly pass that value and decreasing again to

much lower values, much like what we saw in the results of Figure 5.12. But for the iron-induced showers, the initial growth is much less accentuated and the decrease is more prominent. In conclusion, for the p_T distribution of the three species of particles and for both the proton and iron cases, EPOS-QGP usually assumes values equal to or lower than EPOS-LHC, especially for the strange particles, only surpassing it in the low-p_T region (usually between 0 and 2 GeV/c) for the proton-induced showers. Hence, EPOS-QGP seems to produce more low-p_T particles and less high-p_T ones than EPOS-LHC, which might be aligned with the particle energy loss caused by jet-quenching in a QGP medium, although this feature is more visible in the proton-induced showers than in the iron ones.

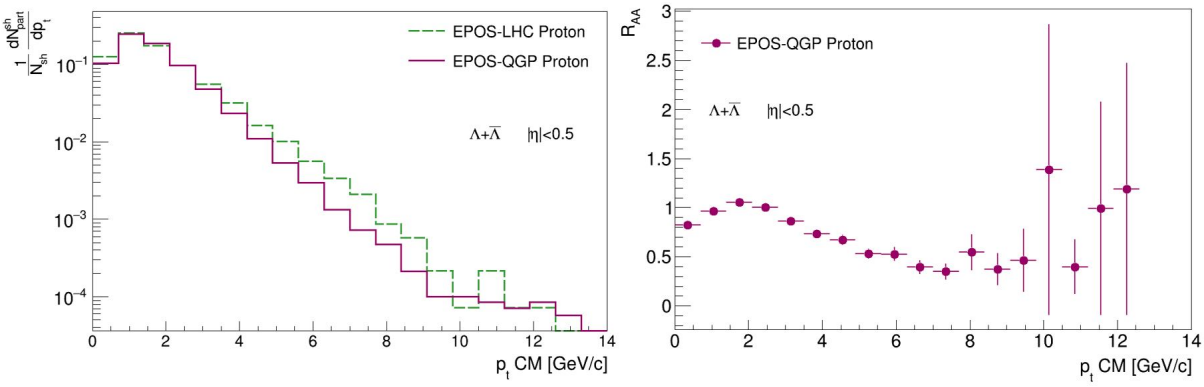

Figure 5.19: **Left**: Distribution of the transverse momentum of the secondary Λ+$\bar{\Lambda}$ particles in the center-of-mass frame and in the pseudo-rapidity region $-0.5 < \eta < 0.5$, normalized by the number of simulated showers N_{sh} for EPOS-LHC proton (green, dashed line) and EPOS-QGP proton (magenta, full line) primaries at fixed energy $\log(E/\mathrm{eV}) = 19$. **Right**: Nuclear modification factor dependence on the center-of-mass transverse momentum of the secondary Λ+$\bar{\Lambda}$ particles, calculated for EPOS-QGP proton with respect to EPOS-LHC proton in the same pseudo-rapidity region and for the same energy.

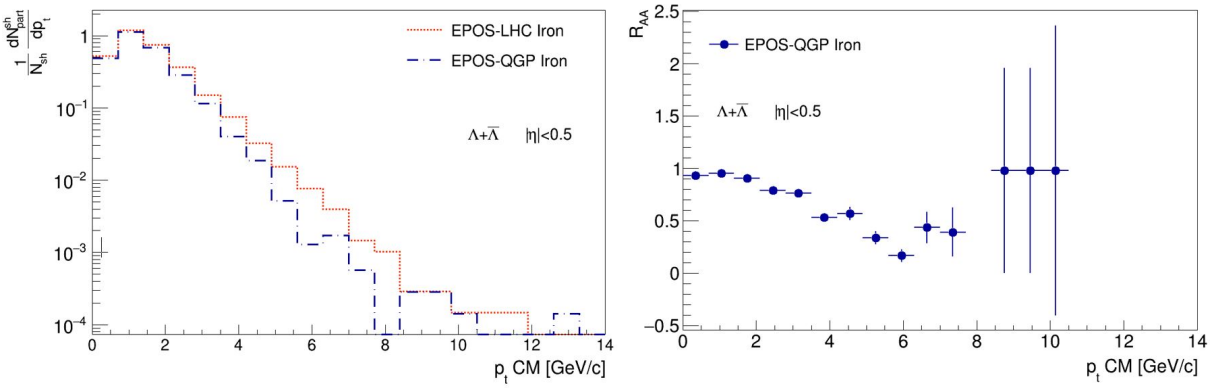

Figure 5.20: **Left**: Distribution of the transverse momentum of the secondary Λ+$\bar{\Lambda}$ particles in the center-of-mass frame and in the pseudo-rapidity region $-0.5 < \eta < 0.5$, normalized by the number of simulated showers N_{sh} for EPOS-LHC iron (orange, dotted line) and EPOS-QGP iron (blue, mixed line) primaries at fixed energy $\log(E/\mathrm{eV}) = 19$. **Right**: Nuclear modification factor dependence on the center-of-mass transverse momentum of the secondary Λ+$\bar{\Lambda}$ particles, calculated for EPOS-QGP iron with respect to EPOS-LHC iron in the same pseudo-rapidity region and for the same energy.

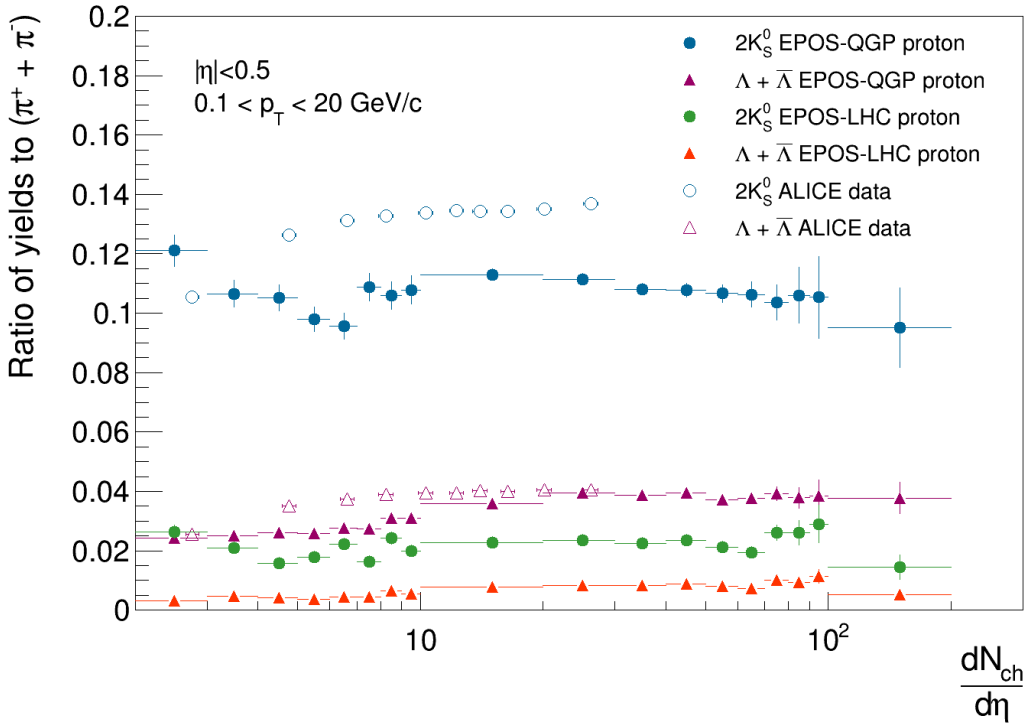

Figure 5.21: Strange hadron-to-pion ratios as a function of the charged-particle multiplicity density in the pseudo-rapidity interval $-0.5 < \eta < 0.5$ and in the p_T interval $0.1 < p_T < 20$, for EPOS-QGP and EPOS-LHC proton primaries at fixed energy $\log(E/\mathrm{eV}) = 19$. Data collected by the ALICE collaboration is shown in open markers [64].

In order to understand the strangeness production, in Figure 5.21 we show the ratio of strange to non-strange particles, namely $\frac{K^0_S}{\pi^\pm}$ and $\frac{\Lambda+\bar{\Lambda}}{\pi^\pm}$, as a function of the charged-particle multiplicity density in the pseudo-rapidity region $-0.5 < \eta < 0.5$ and for the transverse momentum interval $0.1 < p_T < 20$, both for EPOS-LHC proton and for EPOS-QGP proton. These results are also compared to the ALICE findings for pp collisions at $\sqrt{s} = 13$ TeV [64], which showed an universality independent of the colliding system and of the centre-of-mass energy. The ratios were obtained through the following process: through the integral of the equivalent of the distributions of Figures 5.15, 5.17 and 5.19 for the $0.1 < p_T < 20$ region, we got the total multiplicity of the charged pions, of the K^0_S mesons and of the $\Lambda + \bar{\Lambda}$ baryons. We then performed the strange to non-strange ratios by dividing the multiplicity of the K^0_S by that of the charged pions and the multiplicity of $\Lambda + \bar{\Lambda}$ also by that of the charged pions. This ratio was calculated in function of the total number of charged particles also present in the $0.1 < p_T < 20$ and $-0.5 < \eta < 0.5$ intervals, $\frac{dN_{ch}}{d\eta}$. The exact same procedure was performed for EPOS-QGP iron and EPOS-LHC iron, with the results being present in Figure 5.22. Focusing on the proton-induced showers, the EPOS-QGP K^0_S ratio displays values compatible with the ones from the ALICE data, although the behaviour trend is not quite the same. As for the EPOS-QGP Λ+$\bar{\Lambda}$ ratios, both the values and the behavioral trend are similar to the ones presented by the ALICE data. Curiously enough, the EPOS-LHC proton results show the exact same behavioral trend as the EPOS-QGP ones but with much lower values, not reaching the ALICE data at all. However, this discrepancy between the values reached by EPOS-LHC proton and EPOS-QGP proton shows a strangeness enhancement in the later which is compatible with the presence of a QGP

medium. This enhancement is more visible for the strange mesons than for the strange baryons. Finally, for the iron-induced showers, both the K^0_S and the Λ+$\bar{\Lambda}$ ratios are compatible with the ALICE data, but we don't see a significant strangeness enhancement in neither. This is puzzling, since we have already seen that EPOS-QGP iron increases the number of muons at the ground.

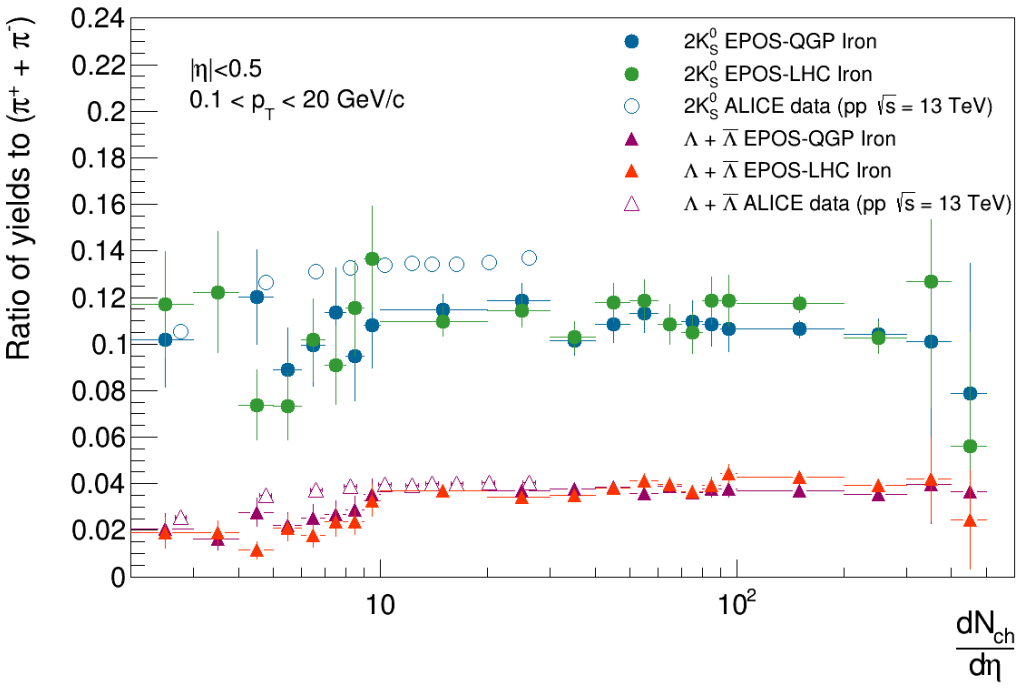

Figure 5.22: Strange hadron-to-pion ratios as a function of the charged-particle multiplicity density in the pseudo-rapidity interval $-0.5 < \eta < 0.5$ and in the p_T interval $0.1 < p_T < 20$, for EPOS-QGP and EPOS-LHC iron primaries at fixed energy $\log(E/\mathrm{eV}) = 19$. Data collected by the ALICE collaboration is shown in open markers [64].

Chapter 6

QGP impact in air shower observables

After having evaluated the impact of EPOS-QGP on the first interaction, we now turn to its effects on the subsequent shower development, evaluating different shower observables, namely the ones presented in section 2.3: the depth of the shower maximum X_{max}, the number of muons at the ground N_μ, the USP shape parameters R and L and the muon production depth maximum X^μ_{max}. The same simulations mentioned in Chapter 5 were used for the distributions of these observables and for their correlations. In addition, we also observed their energy-dependence by simulating showers in the same conditions as before, but now for the following energies: 10^{14}, 10^{15}, 10^{16}, $10^{17.5}$, 10^{18}, $10^{18.5}$, 10^{19} and $10^{19.5}$ eV for EPOS-QGP proton and EPOS-LHC proton, and $10^{17.5}$, 10^{18}, $10^{18.5}$, 10^{19} and $10^{19.5}$ eV for EPOS-LHC iron and EPOS-QGP iron. Note that the study of EPOS-QGP focused only on showers with a pure proton or pure iron composition for the primary, but other compositions are possible.

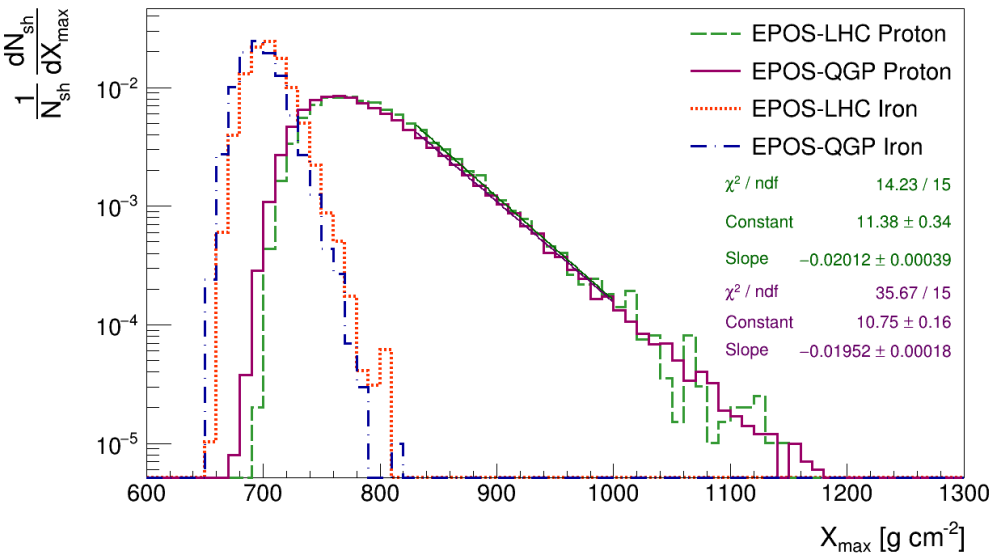

Figure 6.1: Distribution of the depth of the shower maximum normalized by the number of simulated showers N_{sh} for EPOS-LHC iron (orange, dotted line), EPOS-LHC proton (green, dashed line), EPOS-QGP proton (magenta, full line) and EPOS-QGP iron (blue, mixed line) primaries at fixed energy $\log(E/\mathrm{eV}) = 19$.

Starting with the depth of the shower maximum, Figure 6.1 shows its distribution normalized by the number of simulated shower for each model with two fits performed for the ascending region of the curves of EPOS-LHC proton and EPOS-QGP proton. The iron-induced showers have a narrower and lower-valued distribution than the proton-induced ones, which complies with equation 2.7. Both for iron- and proton-induced showers, the EPOS-QGP distribution presents a similar behaviour to the EPOS-LHC one, although it encompass slightly shallower showers. In fact, EPOS-QGP proton starts at around 14 g cm^{-2} earlier than EPOS-LHC proton, with the difference being half this value for the iron-induced showers. Consequently, the EPOS-QGP distribution reaches a maximum about 14 g cm^{-2} and 7 g cm^{-2} earlier than the EPOS-LHC one, for the proton and iron-induced showers, respectively. This would seem to imply that the EPOS-QGP curves are shifted to the left in comparison to the EPOS-LHC ones, if it weren't for the fact that they reach the same maximum values of X_{max} as the EPOS-LHC ones, although with fluctuations. Also worth noting is that the slopes of the exponential tails of EPOS-QGP and EPOS-LHC proton are similar (their difference is of about 3%), indicating an unchanging first interaction cross-section [96, 97].

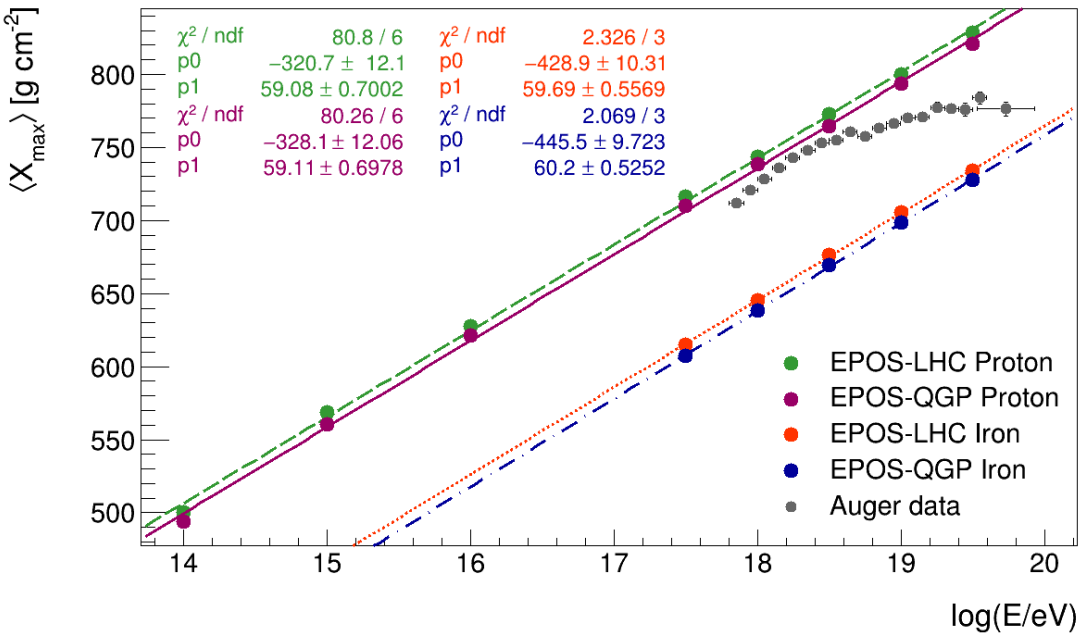

Figure 6.2: The average value of the depth of the shower maximum for EPOS-LHC iron (orange, dotted line), EPOS-LHC proton (green, dashed line), EPOS-QGP proton (magenta, full line) and EPOS-QGP iron (blue, mixed line) rimaries. Each point represents the performed fixed energy simulations. Compared with data obtained by the Pierre Auger Observatory (gray) [7]. The fits follow the line equation $\langle X_{max} \rangle = p0 + p1 \log(E/eV)$.

Furthermore, Figure 6.2 presents the energy dependence of the average X_{max} for all the models, with the corresponding fits following the equation $\langle X_{max} \rangle = p0 + p1 \log(E/eV)$, and compares it to data collected by the Pierre Auger Observatory [17]. For all models, the mean value of the depth of the shower maximum increases linearly with the logarithm of the energy of the primary particle, as would be expected from equation 2.2. The elongation rates obtained from the performed fits of EPOS-QGP and EPOS-LHC are also similar: around 59 g cm^{-2} for the proton-induced showers and about 60 g cm^{-2} for

the iron-induced ones. Moreover, the iron-induced showers present lower mean values of X_{max}, which is in accordance with equation 2.7. EPOS-QGP produces slightly shallower showers with respect to EPOS-LHC: approximately 7 g cm^{-2} earlier both for proton- and iron-induced showers. This can be justified by the fact that EPOS-QGP encompasses slightly lower values of X_{max} than EPOS-LHC, as seen in Figure 6.1. Note that the Pierre Auger Observatory data is well contained by the models predictions, just like in Figure 6.3, which shows the shower-to-shower fluctuations of X_{max}. Although EPOS-QGP and EPOS-LHC present similar behavioural trends both for proton- and iron-induced showers, the average difference between the two models predictions is about 1.5% for the former and 2.1% for the latter. Hence, we can conclude that EPOS-QGP does not alter the behaviour of the depth of the shower maximum significantly.

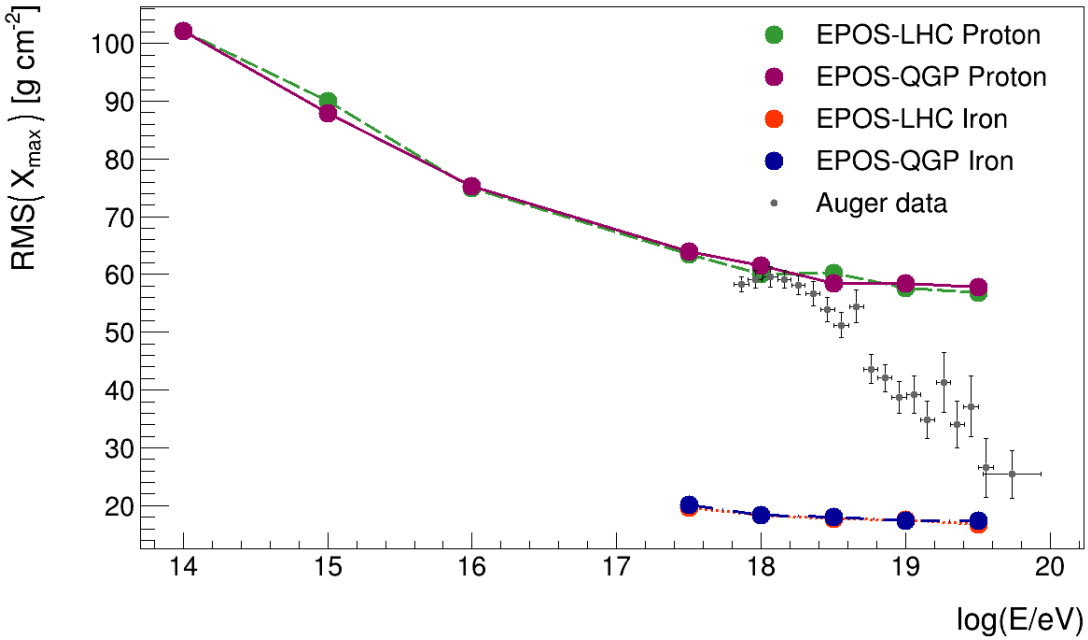

Figure 6.3: Shower-to-shower fluctuations of the depth of the shower maximum for EPOS-LHC iron (orange, dotted line), EPOS-LHC proton (green, dashed line), EPOS-QGP proton (magenta, full line) and EPOS-QGP iron (blue, mixed line) primaries. Each point represents the performed fixed energy simulations. Compared with data obtained by the Pierre Auger Observatory (gray) [7].

As for the number of muons at the ground, Figure 6.4 exhibits the distribution of N_μ with two fits performed for the ascending region of the curves of EPOS-LHC proton and EPOS-QGP proton. According to equation 2.6, heavier primaries imply more muons at the ground, which justifies the narrower but higher-valued curve of the iron-induced showers, in comparison to the proton-induced ones. Nevertheless, while for the former the EPOS-QGP curve starts and ends about 10% after the EPOS-LHC one (with the peak being reached also roughly 10% after), implying a shift towards a higher number of muons at the ground; for the latter, the EPOS-QGP curve starts at around the same value as the EPOS-LHC one, but it ends and reaches its peak about 11% after. We can conclude that EPOS-QGP increases the number of muons at the ground relative to EPOS-LHC, for both proton- and iron-induced showers. Furthermore, the slopes of the exponential tail of the EPOS-LHC proton and EPOS-QGP proton curves are very similar, presenting a difference of about 7.5%. This indicates that the π^0 energy spectrum tails

in the first interaction are essentially the same [98].

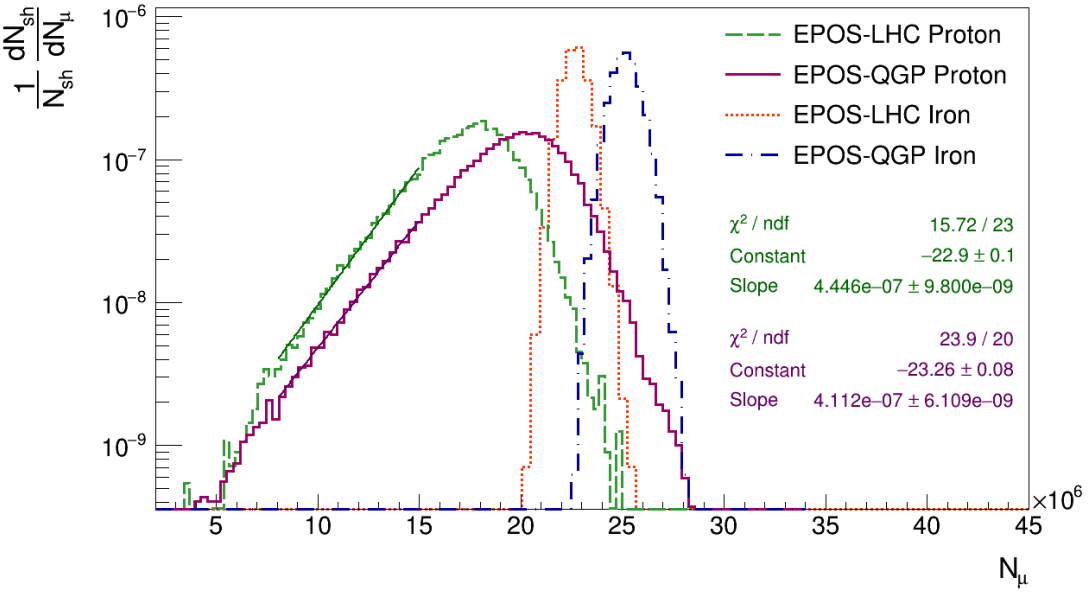

Figure 6.4: Distribution of the number of muons at the ground normalized by the number of simulated showers N_{sh} for EPOS-LHC iron (orange, dotted line), EPOS-LHC proton (green, dashed line), EPOS-QGP proton (magenta, full line) and EPOS-QGP iron (blue, mixed line) primaries at fixed energy $\log(E/\mathrm{eV}) = 19$.

Moreover, Figure 6.5 presents the energy dependence of the mean of the logarithm of the number of muons at the ground for the different models, with the corresponding fits following the equation $\langle \log(N_\mu) \rangle = p0 + p1 \log(E/\mathrm{eV})$. As expected from equation 2.4, $\langle \log(N_\mu) \rangle$ increases linearly with the logarithm of the energy for all models, which present similar slopes (approximately 0.9 for all models). The iron-induced showers display higher values of $\langle \log(N_\mu) \rangle$ than the proton-induced ones, which is in line with equation 2.6. However, from equation 2.4, one would expect the number of muons to increase with the number of charged pions and, since EPOS-QGP should show a baryon enhancement, it should present higher values of $\langle \log(N_\mu) \rangle$ than EPOS-LHC, both in the proton and in the iron cases. This is indeed what we observe, especially for the higher energies. In addition, Figure 6.6 displays the shower-to-shower fluctuations of the number of muons at the ground. They increase linearly with the logarithm of the energy for all models, although the iron-induced showers present lower values (about 25% lower). Nevertheless, within each primary composition case, the EPOS-QGP curve basically overlaps the EPOS-LHC one, especially for the lower energies. Therefore, EPOS-QGP does not seem to alter the shower-to-shower fluctuations of the number of muons at the ground.

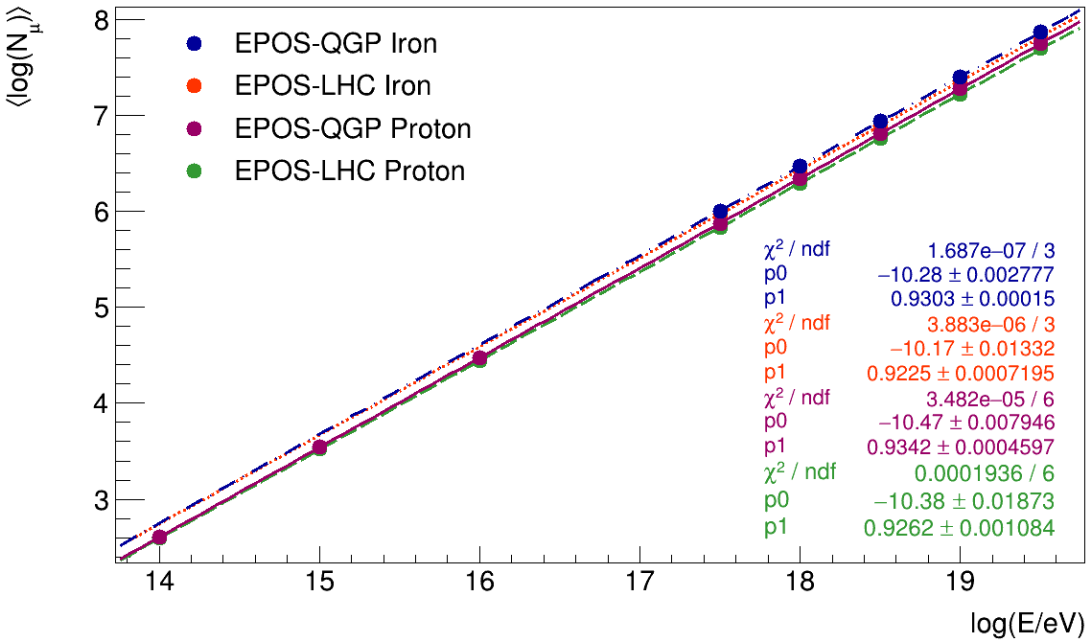

Figure 6.5: The mean value of the logarithm of the number of muons at the ground for EPOS-LHC iron (orange, dotted line), EPOS-LHC proton (green, dashed line), EPOS-QGP proton (magenta, full line) and EPOS-QGP iron (blue, mixed line) primaries. Each point represents the performed fixed energy simulations. The fits follow $\langle \log(N_\mu) \rangle = p0 + p1 \log(E/\mathrm{eV})$.

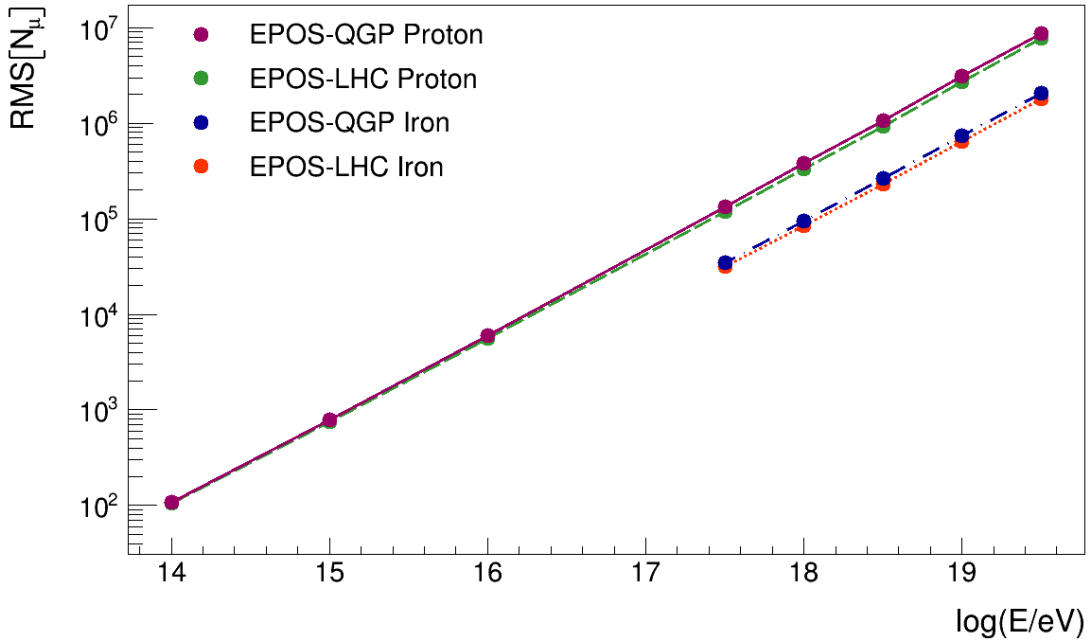

Figure 6.6: Shower-to-shower fluctuations of the number of muons at the ground for EPOS-LHC iron (orange, dotted line), EPOS-LHC proton (green, dashed line), EPOS-QGP proton (magenta, full line) and EPOS-QGP iron (blue, mixed line) primaries. Each point represents the performed fixed energy simulations.

The R_μ parameter introduced in section 2.3 was also studied, in order to allow the comparison with the existing data presented in Figures 2.7 (left) and (right). Indeed, Figure 6.7 shows the energy dependence of the average value of R_μ, as predicted by the different models. They all show a decrease

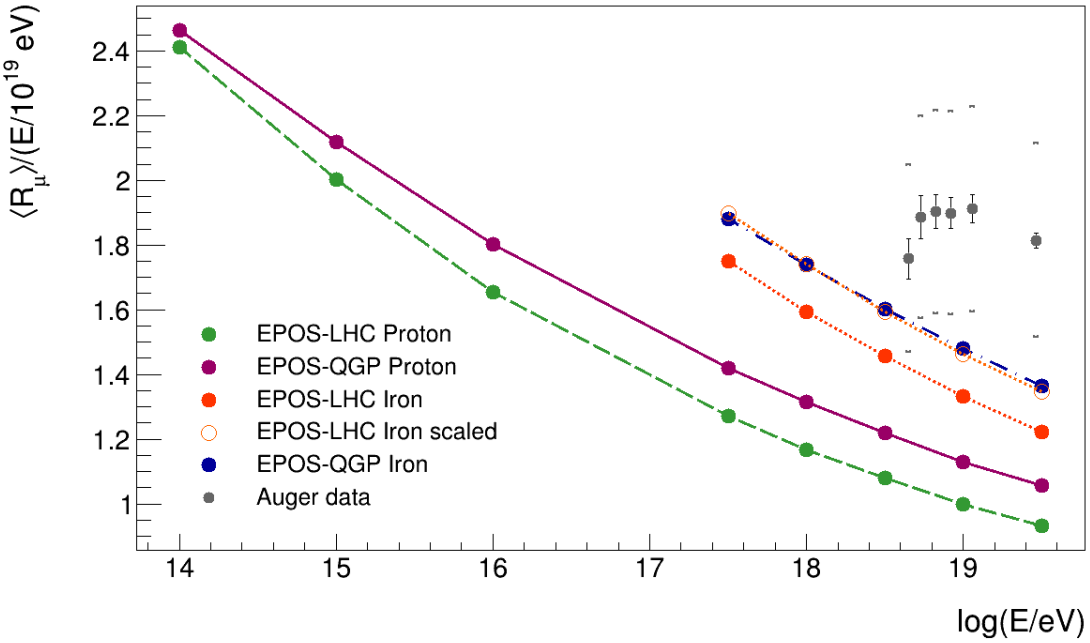

Figure 6.7: The mean value of the ratio $R_\mu = \frac{N_\mu}{\langle N_\mu \rangle_{p,10^{19}}}$, normalized by the energy of the shower divided by the reference energy of 10^{19} eV, in function of the shower energy for EPOS-LHC iron (orange, dotted line), EPOS-LHC proton (green, dashed line), EPOS-QGP proton (magenta, full line) and EPOS-QGP iron (blue, mixed line) primaries. Each point represents the performed fixed energy simulations. A rough estimate for iron-induced showers simulated with EPOS-QGP was calculated through the difference found between EPOS-QGP proton and EPOS-LHC proton (orange, open circles). Compared with data obtained by the Pierre Auger Observatory (gray) [20].

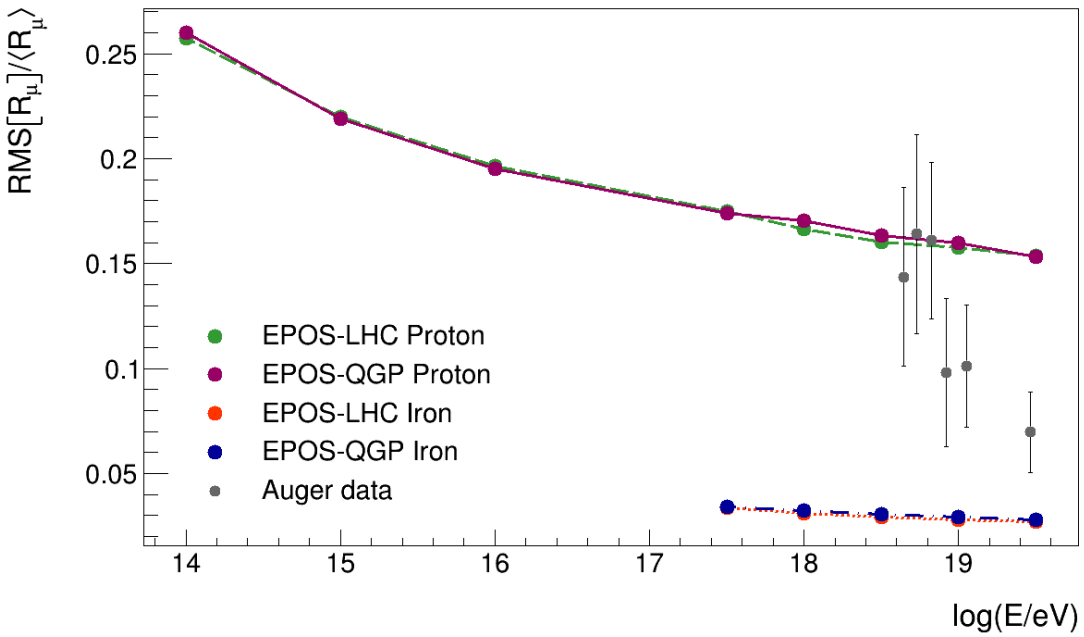

Figure 6.8: Relative fluctuations in the number of muons at the ground for EPOS-LHC iron (orange, dotted line), EPOS-LHC proton (green, dashed line), EPOS-QGP proton (magenta, full line) and EPOS-QGP iron (blue, mixed line) primaries. Each point represents the performed fixed energy simulations. Compared with data obtained by the Pierre Auger Observatory (gray) [20].

with the logarithm of the energy, with the iron-induced showers exhibiting higher values of $\langle R_\mu \rangle$, as would be expected from equation 2.6. Comparing the proton-induced showers, EPOS-QGP exhibits higher values for the mean value of R_μ than EPOS-LHC, especially for the higher energies. For example, for an energy of $\log(E/\mathrm{eV}) = 19.5$ the increase is of about 13.3% and for an energy of $\log(E/\mathrm{eV}) = 14$ it is only 2.2%. The same happens for the iron-induced showers, with an approximate increase of 11.6% for an energy of $\log(E/\mathrm{eV}) = 19.5$ and of 7.6% for an energy of $\log(E/\mathrm{eV}) = 17.5$. This is aligned with the conclusion that EPOS-QGP increases the number of muons at the ground. Also note that the open markers in orange represent a rough estimate for the results of EPOS-QGP iron based on the difference found between EPOS-QGP proton and EPOS-LHC proton. Its curious that this rough estimate overlaps the actual results of EPOS-QGP iron and that these, on their turn, overlap a portion of the region of the data collected by the Pierre Auger Observatory. This means that, when it comes to the number of muons at the ground, the mechanism EPOS-QGP employs to increase it works alike both for proton and iron primaries. Finally, the relative fluctuations in the number of muons at the ground as a function of the energy were also studied and are shown in Figure 6.8. The iron-induced showers present lower values than the proton-induced ones (about 18.3% for EPOS-LHC and about 18.8% for EPOS-QGP) and the data collected by the Pierre Auger Observatory is contained between all the models curves. Both for proton- and iron-induced showers, EPOS-QGP does not seem to alter the relative fluctuations in comparison to EPOS-LHC, which is a condition to solve the Muon Puzzle, as discussed in section 2.4. In fact, in both cases the curves seem to overlap, except for the proton primaries with energies between $\log(E/\mathrm{eV}) = 18$ and $\log(E/\mathrm{eV}) = 18.5$, where the difference between the values reached is of about 2%, which is a very low discrepancy.

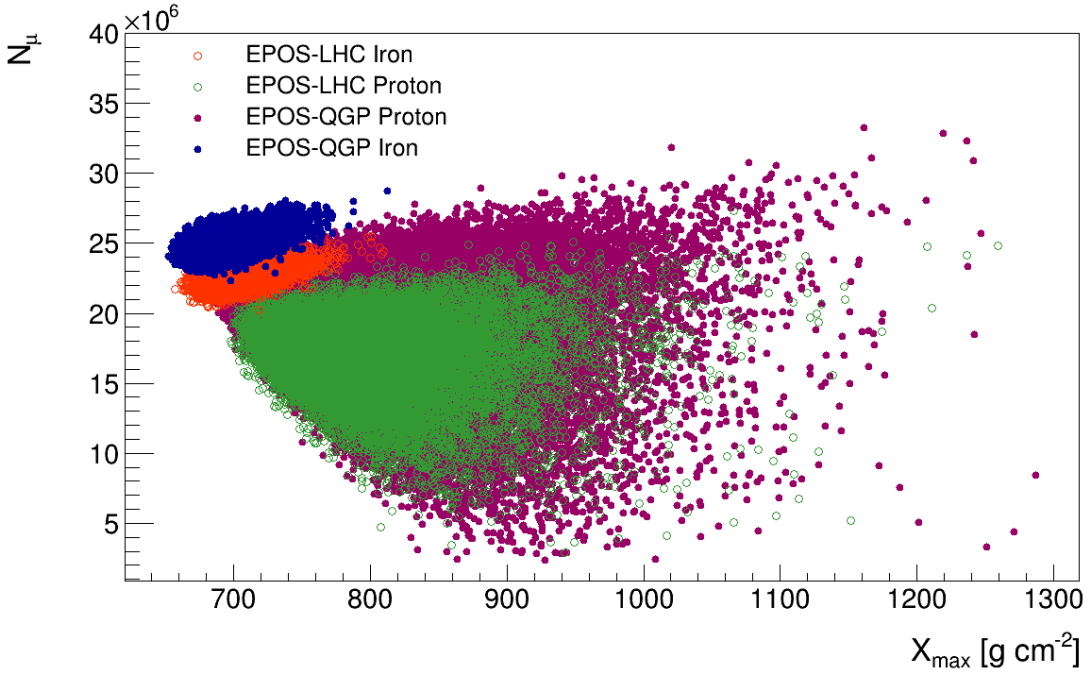

Figure 6.9: Number of muons at the ground in function of the depth of the shower maximum for EPOS-LHC iron (green, dashed line), EPOS-LHC proton (orange, dotted line), EPOS-QGP proton (magenta, full line) and EPOS-QGP iron (blue, mixed line) primaries at fixed energy $\log(E/\mathrm{eV}) = 19$.

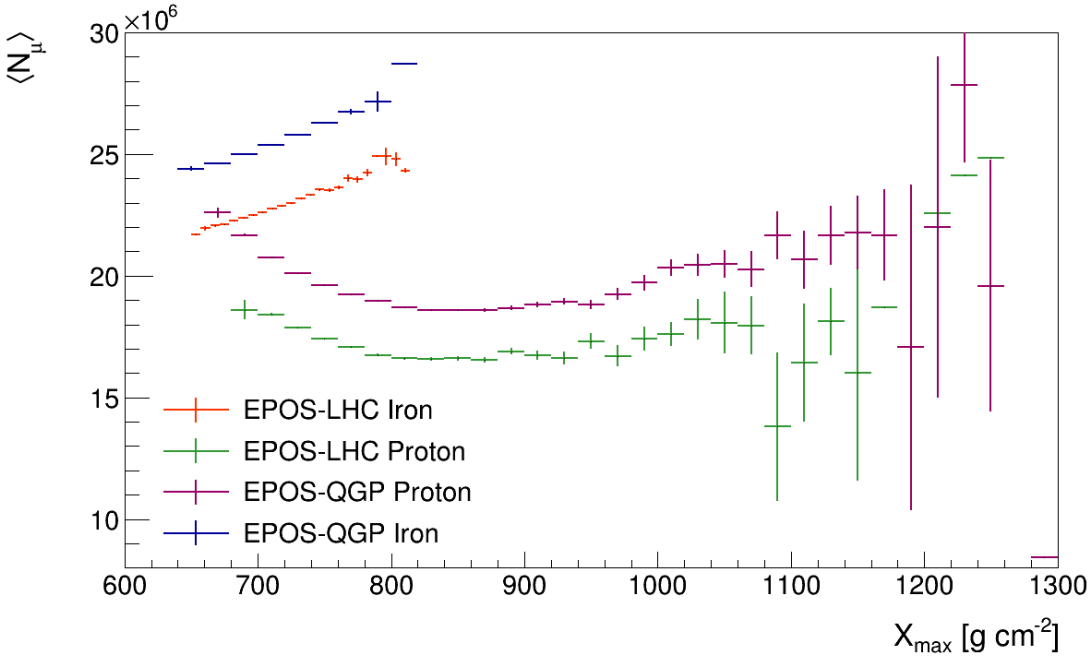

Figure 6.10: Mean of the number of muons at the ground for each bin of the depth of the shower maximum for EPOS-LHC iron (orange, dotted line), EPOS-LHC proton (green, dashed line), EPOS-QGP proton (magenta, full line) and EPOS-QGP iron (blue, mixed line) primaries at fixed energy $\log(E/\mathrm{eV}) = 19$.

Having the distributions of two of the most important shower observables, X_{max} and N_μ, it became imperative to study the correlation between them, which is shown in Figure 6.9. Heavier primaries indicate smaller X_{max} but higher N_μ, which is what we observe in the iron-induced showers when compared to the proton-induced ones. In both cases, the EPOS-QGP results span approximately the same values of X_{max} but for a higher number of muons, which is aligned with the conclusion that EPOS-QGP increases the number of muons at the ground without changing X_{max} significantly. However, note that for the iron-induced showers the correlation area seems to be shifted about 11% towards a higher number of muons, whereas for the proton-induced showers there is not a shift: the EPOS-QGP correlation area encompasses the EPOS-LHC one and expands it even further, by reaching higher values of N_μ. This means that EPOS-QGP iron can not reach the lower values of muons reached by the EPOS-LHC iron, but EPOS-QGP proton can reach the same values of muons as EPOS-LHC proton and even more, which is in line with the results presented in Figures 6.1 and 6.4. Figure 6.10 is the profile of the mentioned scatter plot, depicting the average number of muons in function of X_{max} for all models. The conclusions already withdrawn become even clearer here: both for iron- and proton-induced showers, the EPOS-QGP curve exhibits the same trend as the EPOS-LHC one, but for higher values of N_μ, exhibiting a shift of around 11% for the iron case and of around 13% for the proton case.

The electromagnetic longitudinal profiles of the simulated showers are displayed in Figure 6.11 and follow equation 2.9, exhibiting the characteristic universal shape discussed in section 2.3. All models show an identical behaviour, with the exception that the iron-induced showers present slightly lower values of N' in the ascending region of the curve. Thus, EPOS-QGP does not alter the electromagnetic longitudinal profile of the simulated showers. The USP shape parameters R and L were also studied

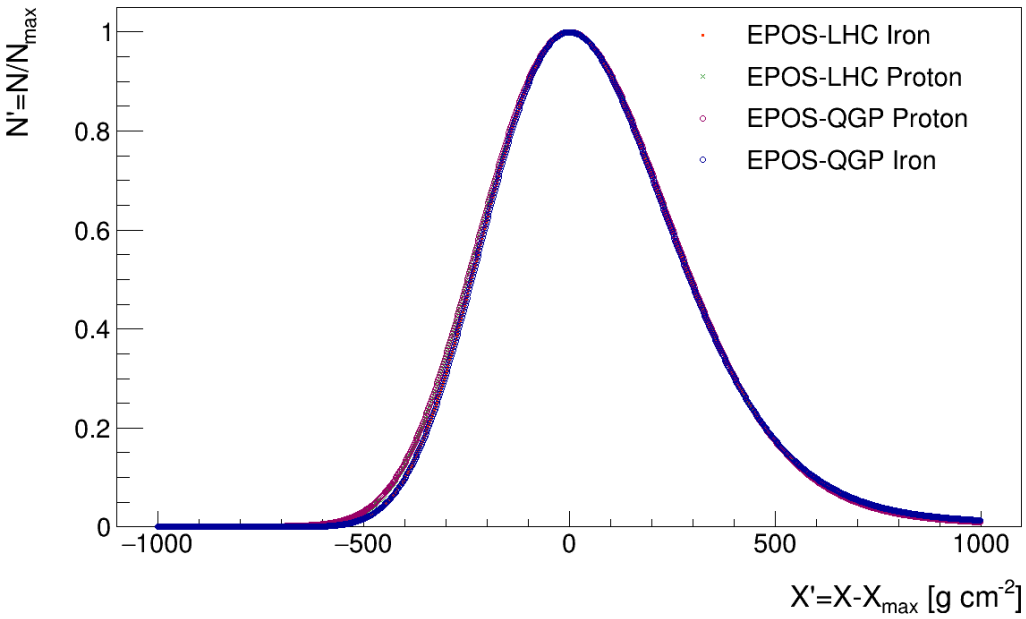

Figure 6.11: Single electromagnetic longitudinal profile as a function of $X' \equiv X - X_{max}$ (and, thus, centered at zero) and normalized to its maximum N_{max}, for EPOS-LHC iron (orange, dotted line), EPOS-LHC proton (green, dashed line), EPOS-QGP proton (magenta, full line) and EPOS-QGP iron (blue, mixed line) primaries at fixed energy $\log(E/\mathrm{eV}) = 19$.

and their distributions are presented in Figures 6.12 and 6.13, respectively. R has a narrower but higher-valued distribution for the iron-induced showers, which is line with the results of Figure 2.10 (left). Both for proton- and iron-induced showers, the curves of EPOS-QGP follow the trend of the ones from EPOS-LHC, encompassing the same values of R. We observe the same behaviour in the L distribution, where the iron-induced showers have slightly narrower and lower-valued distributions, as expected from Figure 2.10 (right). Thus, EPOS-QGP does not alter the distributions of the USP shape parameters R and L significantly. The energy dependence of the mean values of R and L are presented in Figures 6.14 and 6.15, respectively. As expected from Figure 2.10 (left), the mean value of R decreases with energy and the iron-induced showers present higher values of it. Overall, the EPOS-QGP curves basically overlap the EPOS-LHC ones, both for the iron- and proton-induced showers. Indeed, the difference between the EPOS-QGP iron values and the EPOS-LHC iron ones is approximately 0.85$\%$, while the difference found between EPOS-QGP proton and EPOS-LHC proton varies more with energy: for $\log(E/\mathrm{eV}) = 14, 16$ and 19.5 it is about 1.5$\%$, 0.3$\%$ and 2$\%$, respectively. Thus, EPOS-QGP does not alter the energy dependence of R significantly. As for the USP shape parameter L, its mean value increases with energy and assumes lower values for the iron-induced showers, especially for the higher energies, which is aligned with the results from Figure 2.10 (right). The EPOS-QGP curve follows the EPOS-LHC one closely, both for the proton- and iron-induced showers. In fact, the discrepancy found between these two models for the iron case is about 0.2$\%$ and 0.8$\%$ for the energies $\log(E/\mathrm{eV}) = 19.5$ and 17.5, respectively. For the proton case, the discrepancy takes on the approximate values of 0.07$\%$, 0.4$\%$ and 0.2$\%$ for the energies $\log(E/\mathrm{eV}) = 19.5, 17.5$ and 14, respectively. Hence, we can conclude that EPOS-QGP does not vary the energy dependence of the USP shape parameter L significantly.

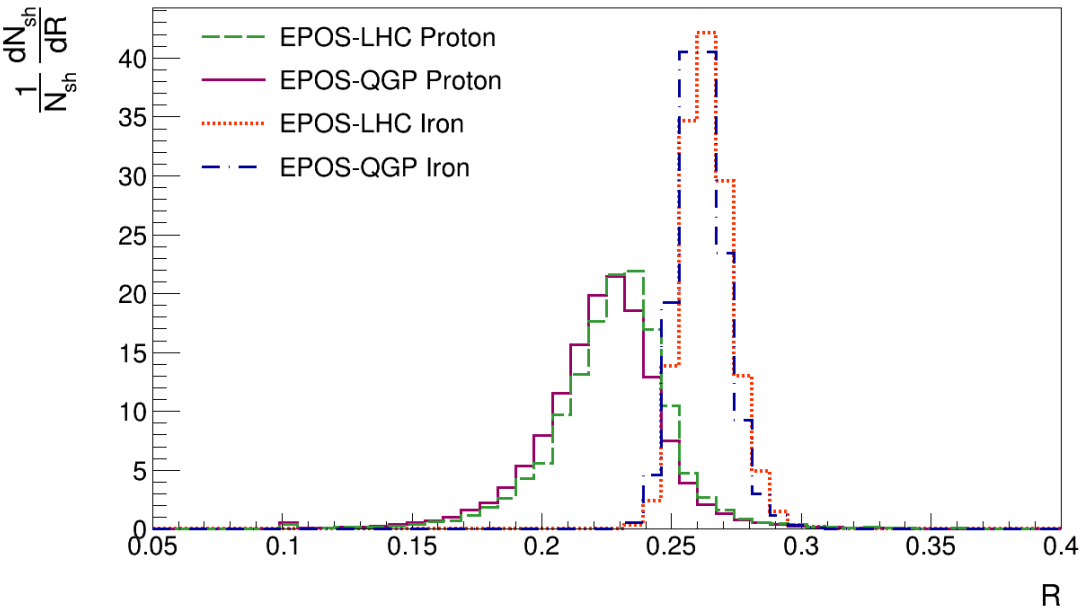

Figure 6.12: Distribution of the USP shape parameter R normalized by the number of simulated showers N_{sh} for EPOS-LHC iron (orange, dotted line), EPOS-LHC proton (green, dashed line), EPOS-QGP proton (magenta, full line) and EPOS-QGP iron (blue, mixed line) primaries at fixed energy $\log(E/\mathrm{eV}) = 19$.

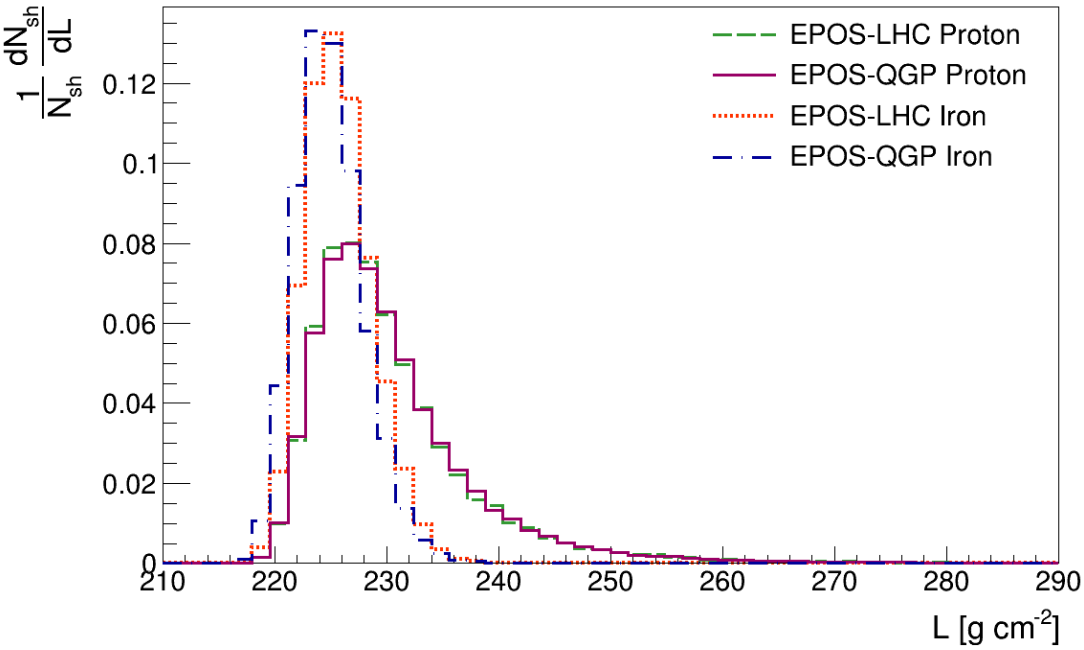

Figure 6.13: Distribution of the USP shape parameter L normalized by the number of simulated showers N_{sh} for EPOS-LHC iron (orange, dotted line), EPOS-LHC proton (green, dashed line), EPOS-QGP proton (magenta, full line) and EPOS-QGP iron (blue, mixed line) primaries at fixed energy $\log(E/\mathrm{eV}) = 19$.

Figure 6.16 shows the average values of L as a function of the average values of R, for all models with primaries of $10^{17.5}$, 10^{18}, $10^{18.5}$ and 10^{19} eV. The corresponding fits are also presented and they follow the equation $\langle L \rangle = p0 + p1\langle R \rangle$. Although the mean value of L decreases with increasing mean

value of R for all models, the decrease is more accentuated for the proton-induced showers. As a matter of fact, while the slopes of the corresponding fits are on average -390 g cm^{-2} for the proton-induced showers, they are approximately -188 g cm^{-2} for the iron-induced ones.

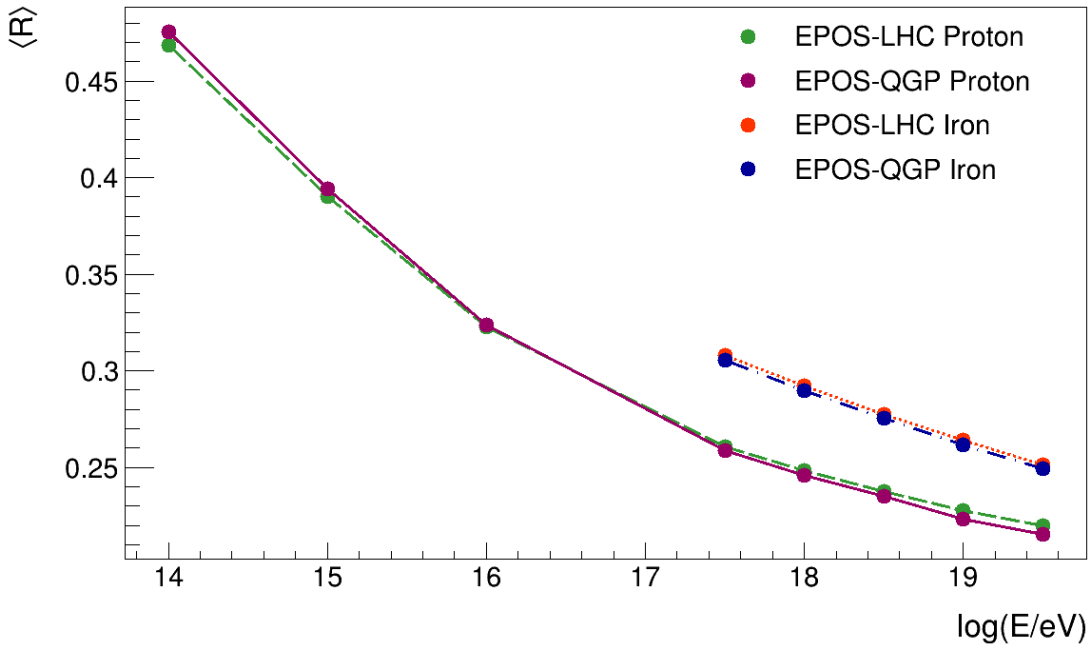

Figure 6.14: The average value of the USP shape parameter R for EPOS-LHC iron (orange, dotted line), EPOS-LHC proton (green, dashed line), EPOS-QGP proton (magenta, full line) and EPOS-QGP iron (blue, mixed line) primaries. Each point represents the performed fixed energy simulations. Compared with data obtained by the Pierre Auger Observatory (gray) [20].

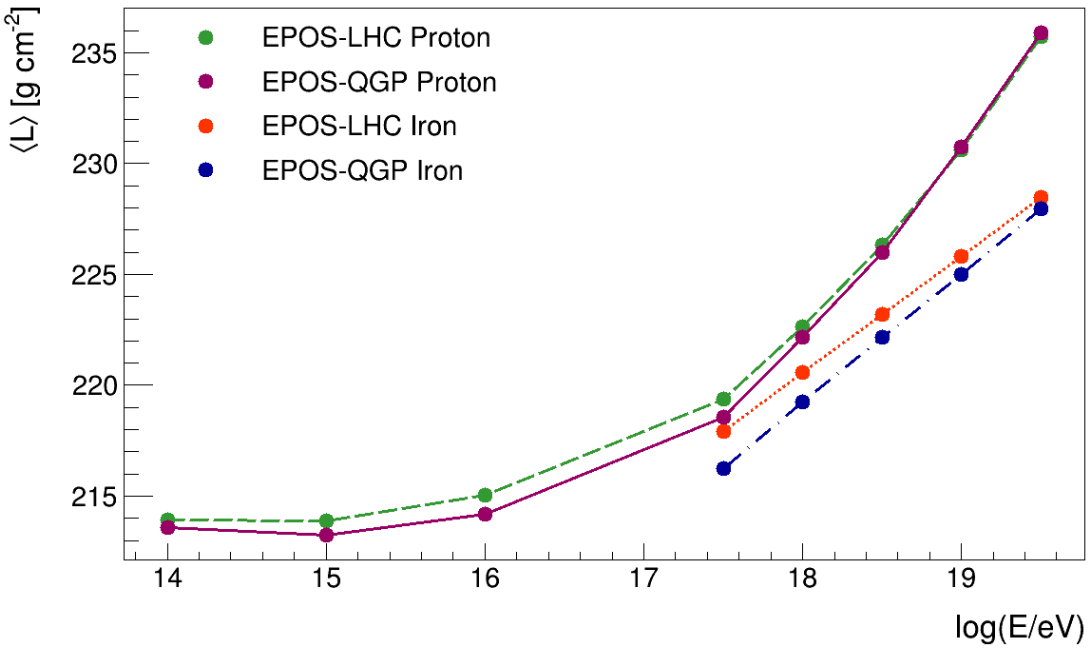

Figure 6.15: The average value of the USP shape parameter L for EPOS-LHC iron (orange, dotted line), EPOS-LHC proton (green, dashed line), EPOS-QGP proton (magenta, full line) and EPOS-QGP iron (blue, mixed line) primaries. Each point represents the performed fixed energy simulations.

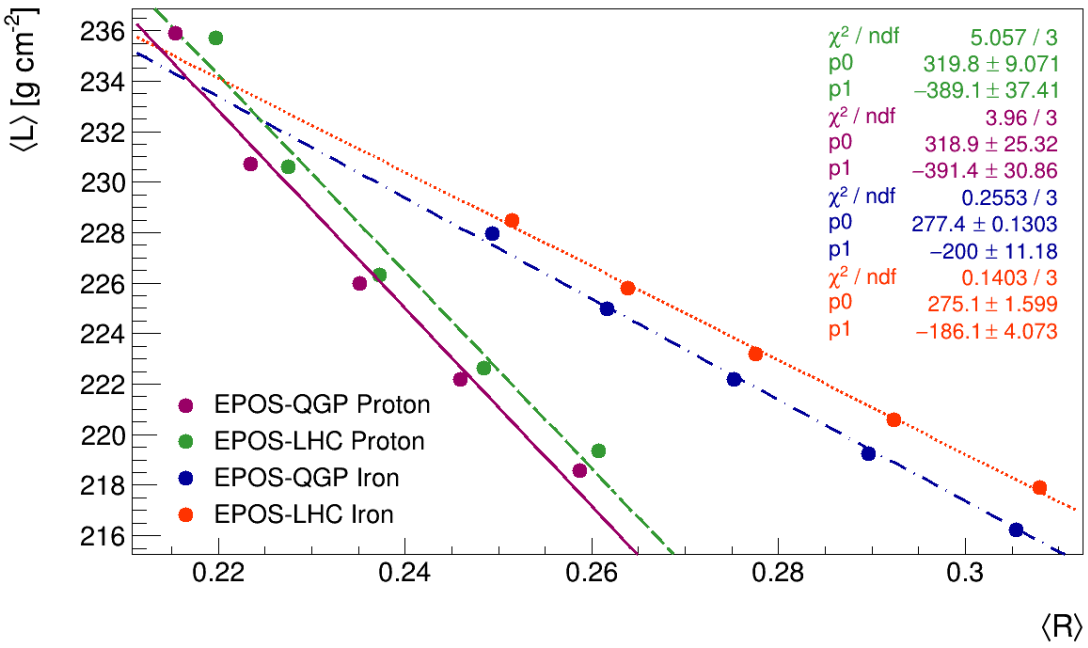

Figure 6.16: The average value of the USP shape parameter L in function of the average value of the USP shape parameter R for EPOS-LHC iron (orange, dotted line), EPOS-LHC proton (green, dashed line), EPOS-QGP proton (magenta, full line) and EPOS-QGP iron (blue, mixed line) primaries. Each point represents the performed fixed energy simulations for $\log(E/\mathrm{eV}) = 19.5, 19, 18, 18.5, 17.5$, starting from the upper left. The fits follow the equation $\langle L \rangle = p0 + p1\langle R \rangle$.

The muon production depth maximum was also simulated for all models and the obtained distribution is presented in Figure 6.17. The iron-induced showers show a narrower and lower-valued distribution, compared to the proton-induced ones, much like what was observed in the distribution of X_{max} (see Figure 6.1). This makes sense since, as already discussed in section 2.3, X^{μ}_{max} is usually reached around 200 g cm^{-2} before X_{max}. For the iron-induced showers, the EPOS-QGP curve starts and reaches its peak about 28 g cm^{-2} earlier than the EPOS-LHC one, but ends only about 14 cm^{-2} earlier. As for the proton case, the EPOS-QGP curve starts about 35 g cm^{-2} earlier than the EPOS-LHC one, reaches its peak approximately 21 g cm^{-2} earlier, but ends at about the same value, apart the final fluctuations. The slopes of the exponential tails of EPOS-LHC proton and EPOS-QGP proton are similar (their difference is of about 1%), indicating that the first interaction cross-section does not change from one model to the other [96, 97]. Therefore, EPOS-QGP encompasses shallower muon production depth maximums than EPOS-LHC, both for proton- and iron-induced showers. Figure 6.18 shows the energy dependency of the average value of X^{μ}_{max} for the different models. Its increase with the logarithm of the energy is universal, although, as expected from Figure 6.17, the iron-induced showers present a lower value of X^{μ}_{max} than the proton ones. Once again, we see that EPOS-QGP produces shallower muon production depth maximums than EPOS-LHC, both for proton- and iron-induced showers. In fact, the average difference between EPOS-QGP iron and EPOS-LHC iron is about 24.6 g cm^{-2}, while the difference between EPOS-QGP proton and EPOS-LHC proton is more energy dependent: it is about 30.2 g cm^{-2} for an energy of $\log(E/\mathrm{eV}) = 19.5$ and around 13.5 g cm^{-2} for an energy of $\log(E/\mathrm{eV}) = 14$. This is aligned with the need for shallower muon production depths, as seen in section 2.4. Note

that these results are not directly comparable with the Pierre Auger Observatory data of Figure 2.12, since those refer to the apparent muon production depth maximum, that is, the X^{μ}_{max} inferred from the measurements at the ground. Thus, we can conclude that EPOS-QGP increases the number of muons at the ground and makes the muon production depth maximum happen sooner in the shower development, both for proton- and iron-induced showers.

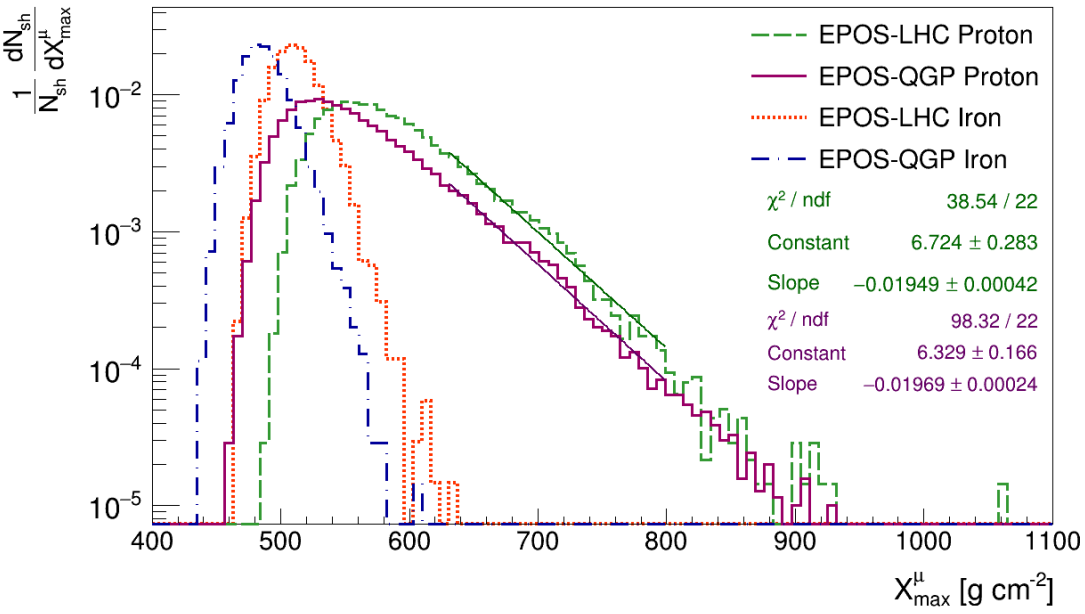

Figure 6.17: Distribution of the muon production depth maximum normalized by the number of simulated showers N_{sh} for EPOS-LHC iron (orange, dotted line), EPOS-LHC proton (green, dashed line), EPOS-QGP proton (magenta, full line) and EPOS-QGP iron (blue, mixed line) primaries at fixed energy $\log(E/\mathrm{eV}) = 19$.

Finally, we also simulated an observable that has not been published yet, but that might be in the future: the difference between the mean of the depth of the shower maximum and the mean of the muon production depth maximum. The energy dependence of this observable is presented in Figure 6.19 for the different models. All simulations show a similar behaviour, with a decreasing trend for lower energies and an increasing trend for higher energies, always in the positive range. This means that the muon production depth is on average shallower than the depth of the shower maximum. The EPOS-QGP curves appear to be shifted towards higher values of $\langle X_{max}\rangle - \langle X^{\mu}_{max}\rangle$, with respect to the EPOS-LHC ones, both for proton- and iron-induced showers, and especially at higher energies. Indeed, the average difference found between EPOS-QGP iron and EPOS-LHC iron is about 18 g cm^{-2}, while for the proton case the difference is more energy dependent: approximately 22.8 g cm^{-2} for an energy of $\log(E/\mathrm{eV}) = 19.5$ and around 7 g cm^{-2} for an energy of $\log(E/\mathrm{eV}) = 14$. Note that both X^{μ}_{max} and X_{max} depend on the depth of the first interaction X_1, hence their difference is only sensitive to the subsequent development of the shower. This means that this observable can give us information about the history of pion production.

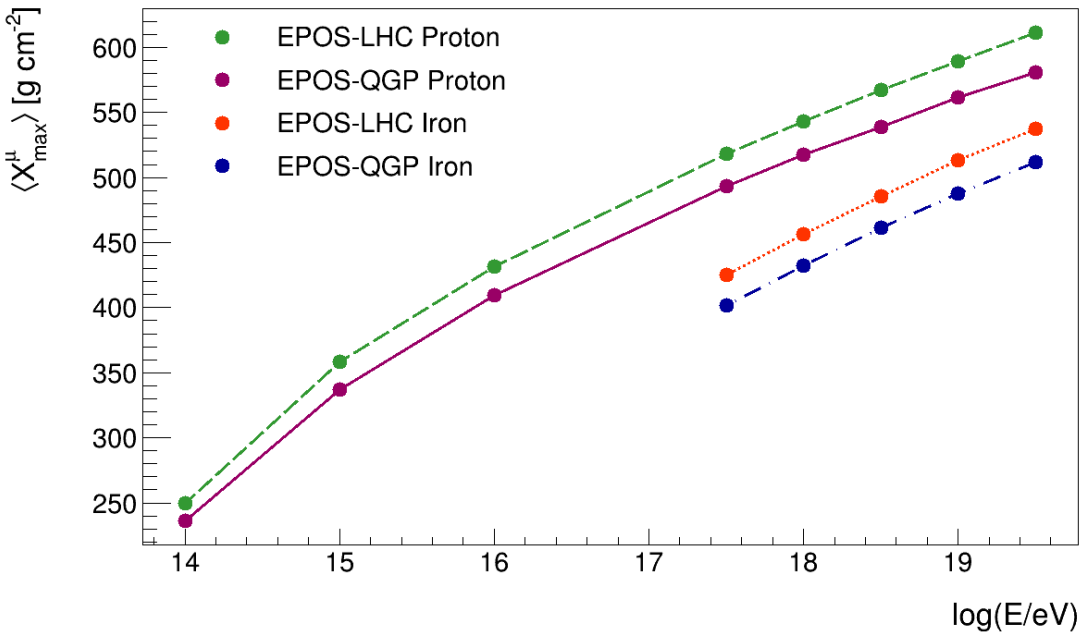

Figure 6.18: The average value of the depth of the muonic shower maximum for EPOS-LHC iron (orange, dotted line), EPOS-LHC proton (green, dashed line), EPOS-QGP proton (magenta, full line) and EPOS-QGP iron (blue, mixed line) primaries. Each point represents the performed fixed energy simulations.

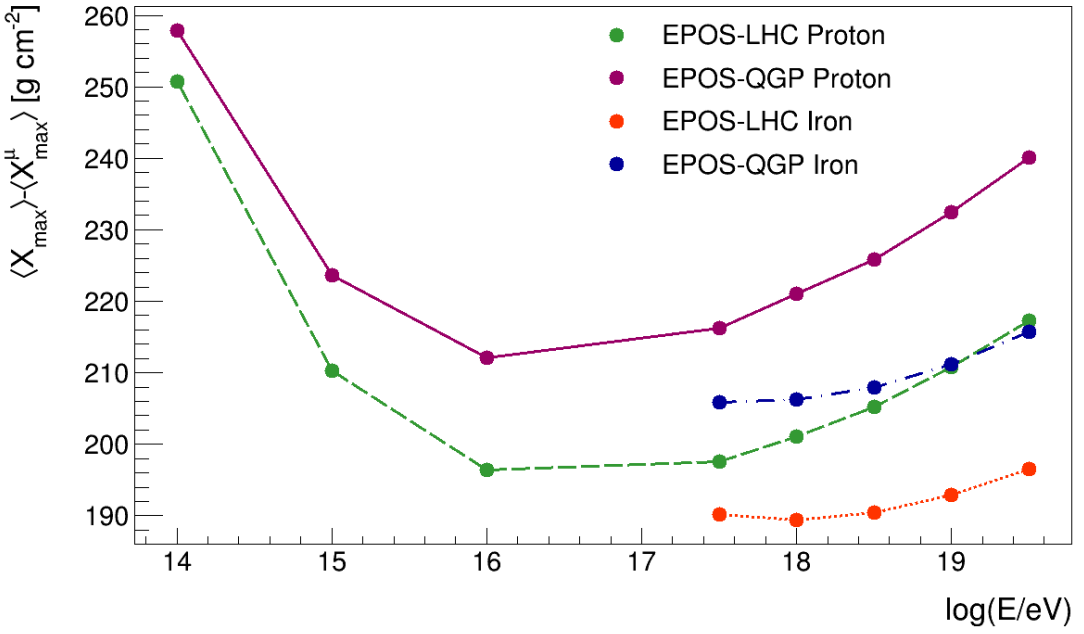

Figure 6.19: The difference between the mean of the muon production depth maximum and the mean of the depth of the shower maximum for EPOS-LHC iron (orange, dotted line), EPOS-LHC proton (green, dashed line), EPOS-QGP proton (magenta, full line) and EPOS-QGP iron (blue, mixed line) primaries. Each point represents the performed fixed energy simulations.

6.1 Summary

Table 6.1 summarizes the discrepancy values between EPOS-QGP proton and EPOS-LHC proton for the mean and for the fluctuations of the studied shower observables, for showers with a 10^{19} eV primary. Table 6.2 does the same for the iron-induced showers. We can see that in both cases, EPOS-QGP produces slightly less deep electromagnetic showers, with the EPOS-QGP iron ones being the most shallow (approximately 7 g cm^{-2} shallower). Meanwhile, EPOS-QGP increases the average number of muons at the ground by about 13$\%$ for the proton-induced showers and by around about 11$\%$ for the iron-induced ones, while producing shallower muon production depth maximums, namely about 30 g cm^{-2} shallower in both cases. The mean values of the USP shape parameters R and L are left almost unchanged, with the largest change being the EPOS-QGP iron variation of the L value by nearly 1 g cm^{-2}. The changes in the $X_{max} - X^{\mu}_{max}$ observable are a direct consequence of the shallower depth of the shower maximums and muon production depth maximums produced by EPOS-QGP. In addition, in both proton- and iron-induced showers, the fluctuations of the studied observables don't change significantly, although EPOS-QGP proton does show larger variations than EPOS-QGP iron, in general. The exception are the relative fluctuations in the number of muons at the ground, which are varied by about 1$\%$ for EPOS-QGP proton and by about 3.5$\%$ for EPOS-QGP iron, although both values are still low. Finally, the slopes in the distributions of X_{max}, N_{μ} and X^{μ}_{max} simulated with EPOS-QGP proton are also similar to the ones simulated with EPOS-LHC proton. In the case of N_{μ}, this is related to the fact that EPOS-QGP proton does not change the π^0 energy spectrum tails in the first interaction. Indeed, we saw that this model did not change the momentum distribution of the secondary particles significantly. For X_{max} and X^{μ}_{max}, the similar slopes indicate that EPOS-QGP proton does not alter the cross-section of the first interaction.

	EPOS-QGP proton with respect to EPOS-LHC proton (E $\sim 10^{19}$ eV)		
	Mean	**Fluctuations**	**Comment**
X_{max}	-6.0 g cm^{-2}	+0.9 g cm^{-2}	Similar slope in the exponential tail
R	-0.004	+0.0009	-
L	+0.1 g cm^{-2}	+0.1 g cm^{-2}	-
N_μ	+13.1%	+1.3%*	Similar slope in the exponential tail
X^μ_{max}	-27.6 g cm^{-2}	+0.7 g cm^{-2}	Similar slope in the exponential tail
$X_{max} - X^\mu_{max}$	+21.6 g cm^{-2}	-	-

*Relative fluctuations.

Table 6.1: Systematization of the obtained results for the mean value and the fluctuations (when applicable) of each air shower observable, when comparing the performance of hadronic interaction models EPOS-QGP and EPOS-LHC for proton-induced showers at 10^{19} eV.

	EPOS-QGP iron with respect to EPOS-LHC iron (E $\sim 10^{19}$ eV)	
	Mean	**Fluctuations**
X_{max}	-7.3 g cm^{-2}	-0.2 g cm^{-2}
R	-0.002	-0.00004
L	-0.8 g cm^{-2}	-0.01 g cm^{-2}
N_μ	+11%	+3.5%*
X^μ_{max}	-25.5 g cm^{-2}	-0.2 g cm^{-2}
$X_{max} - X^\mu_{max}$	+18.2 g cm^{-2}	-

*Relative fluctuations.

Table 6.2: Systematization of the obtained results for the mean value and the fluctuations (when applicable) of each air shower observable, when comparing the performance of hadronic interaction models EPOS-QGP and EPOS-LHC for iron-induced showers at 10^{19} eV.

Chapter 7

Final Remarks and Conclusions

The goal of this dissertation was to assess the behaviour of the hadronic interaction model EPOS-QGP, comparing it with its predecessor EPOS-LHC. In fact, EPOS-QGP was based on EPOS-LHC but was modified in a phenomenological way to show more visible QGP effects, like a baryon and strangeness enhancement. When combined with air shower simulations, like CONEX, the stronger QGP effects of EPOS-QGP should have a direct consequence: the enhancement of the number of muons produced during the shower development while maintaining the remaining shower observables intact, hence solving the infamous Muon Puzzle.

In fact, the results of the simulations performed for this work showed that EPOS-QGP is able to increase the number of muons produced during the shower development by a factor of 13.1$\%$ with respect to EPOS-LHC proton, and of 11.6$\%$ with respect to EPOS-LHC iron, with a primary of 10^{19} eV, without changing the depth of the shower maximum significantly. The remaining shower observables, such as the electromagnetic longitudinal profile, the USP shape parameters R and L and most importantly the relative fluctuations of the number of muons at the ground are also pretty much unchanged. Even the slopes of the exponential tails of the distributions of the depth of the shower maximum, of the number of muons at the ground and of the muon production depth maximum are similar to the ones exhibited by the showers simulated with EPOS-LHC, for the proton-induced showers. The only significantly modified shower observable is the muon production depth maximum, which happens sooner in the shower development.

However, is this muon enhancement related to the formation of QGP along the EAS? To answer this question, we turned to the center-of-mass frame of the interaction and confirmed a baryon and strangeness enhancement compatible with the presence of a QGP medium, but only for the proton-induced showers. We also noticed that EPOS-QGP has a tendency to produce more low-p_T particles and less high-p_T particles than EPOS-LHC, which might be a signature of the jet-quenching phenomenon typical of QGP, but the observed effects were very reduced. Nevertheless, during the transformation of the kinematical quantities from the laboratory reference frame to the centre-of-mass frame of the interaction, we encountered difficulties connected to small energy conservation violations. Although this discrepancy is not relevant for ultra-high energy particles in the laboratory reference frame,

it becomes significant in the center-of-mass frame, since this energy violation is all concentrated in the boost direction. We were able to find a way to work around this by rewritting the Lorentz factor γ and the velocity ratio β in function of the secondary particles rather than of the parent particles, thus forcing energy conservation.

7.1 Achievements and outlook

The work performed for this dissertation is relevant and bears significant importance not only for the cosmic rays field, but also for the heavy-ion one. On one hand, testing the EPOS-QGP model and understanding what its limitations are is an important step in the resolution of the Muon Puzzle, an open question since the beginning of the century. We were able to confirm that this promising hadronic interaction model is in fact able to increase the number of muons in the shower development, while satisfying all the other conditions necessary to solve the Muon Puzzle, and to understand how this was performed. On the other hand, we were able to verify that this muon increase seems to be connected to the presence of a QGP state, namely, through the baryon and strangeness enhancement observed in the first interaction and the transverse momentum characteristics of the secondary particles, at least for proton-induced showers. The quark-gluon plasma is still surrounded by a number of unanswered questions and it is still unclear if it forms in small or even in intermediate systems. The fact that a model which deals with p-A collisions reproduces some of the most visible experimental signatures of this state of matter is another step forward in this field.

Despite the achievements of this work, there are always further steps to take. We decided to focus the study of EPOS-QGP only on showers with a pure proton or pure iron primary composition, but it would be interesting to assess the performance of EPOS-QGP for primaries of intermediate compositions. This would be especially appealing to asses if intermediate compositions would still produce a strangeness enhancement or not. It would also be possible to use, in addition to the EAS simulator CONEX, the Monte Carlo code CORSIKA in order to perform a three-dimensional study of the EAS. Furthermore, in this work, we used a specific version of EPOS-QGP, with a certain parameter tuning, namely with fixed E_{th}, E_{scale} and f_ω (see section 4.2). It would be interesting to assess the model's impact in air shower observables and in hadron interaction quantities for different parameter tunings. Finally, the future data from Run 3 of LHC, namely of p-O and O-O collisions at $\sqrt{s} = 10$ and 7 TeV, respectively, and from the upgrades of Auger Prime will also be imperative to constraint this new hadronic interaction model.

Bibliography

[1] J. Albrecht et al. The Muon Puzzle in cosmic-ray induced air showers and its connection to the Large Hadron Collider. *Astrophys. Space Sci.*, 367(3):27, 2022. doi: 10.1007/s10509-022-04054-5.

[2] T. Pierog, S. Baur, H. P. Dembinski, R. Ulrich, and K. Werner. Collective Hadronization and Air Showers: Can LHC Data Solve the Muon Puzzle ? *PoS*, ICRC2019:387, 2020. doi: 10.22323/1.358.0387.

[3] J. Blumer, R. Engel, and J. R. Horandel. Cosmic Rays from the Knee to the Highest Energies. *Prog. Part. Nucl. Phys.*, 63:293–338, 2009. doi: 10.1016/j.ppnp.2009.05.002.

[4] R. Engel, D. Heck, and T. Pierog. Extensive air showers and hadronic interactions at high energy. *Annual Review of Nuclear and Particle Science*, 61(1):467–489, 2011. doi: 10.1146/annurev.nucl.012809.104544.

[5] P. Blasi. Cosmic Ray Acceleration in Supernova Remnants. In *ICATPP Conference on Cosmic Rays for Particle and Astroparticle Physics*, pages 493–506, 2011. doi: 10.1142/9789814329033_0061.

[6] D. Caprioli. Cosmic-ray acceleration in supernova remnants: non-linear theory revised. *JCAP*, 07:038, 2012. doi: 10.1088/1475-7516/2012/07/038.

[7] P. Abreu et al. Combined fit of the energy spectrum and mass composition across the ankle with the data measured at the Pierre Auger Observatory. *PoS*, ICRC2021:311, 2021. doi: 10.22323/1.395.0311.

[8] L. A. Anchordoqui. Ultra-High-Energy Cosmic Rays. *Phys. Rept.*, 801:1–93, 2019. doi: 10.1016/j.physrep.2019.01.002.

[9] A. Kounine. The Alpha Magnetic Spectrometer on the International Space Station. *Int. J. Mod. Phys. E*, 21(08):1230005, 2012. doi: 10.1142/S0218301312300056.

[10] Y. S. Yoon et al. Cosmic-Ray Proton and Helium Spectra from the First CREAM Flight. *Astrophys. J.*, 728:122, 2011. doi: 10.1088/0004-637X/728/2/122.

[11] A. Aab et al. The Pierre Auger Cosmic Ray Observatory. *Nucl. Instrum. Meth. A*, 798:172–213, 2015. doi: 10.1016/j.nima.2015.06.058.

[12] T. Abu-Zayyad et al. The surface detector array of the Telescope Array experiment. *Nucl. Instrum. Meth. A*, 689:87–97, 2013. doi: 10.1016/j.nima.2012.05.079.

[13] F. Blanco, P. Rocca, and F. Riggi. Cosmic rays with portable geiger counters: From sea level to airplane cruise altitudes. *EUROPEAN JOURNAL OF PHYSICS Eur. J. Phys*, 30:685–695, 07 2009. doi: 10.1088/0143-0807/30/4/003.

[14] M. Risse. Properties of extensive air showers. *Acta Phys. Polon. B*, 35:1787–1798, 2004.

[15] W. Heitler. *The Quantum Theory of Radiation*. Dover Books on Physics. Dover Publications, 1984. ISBN 9780486645582. URL `https://books.google.pt/books?id=L7w7UpecbKYC`.

[16] J. Matthews. A heitler model of extensive air showers. *Astroparticle Physics*, 22(5):387–397, 2005. ISSN 0927-6505. doi: https://doi.org/10.1016/j.astropartphys.2004.09.003. URL `https://www.sciencedirect.com/science/article/pii/S0927650504001598`.

[17] A. Aab et al. Depth of maximum of air-shower profiles at the Pierre Auger Observatory. II. Composition implications. *Phys. Rev. D*, 90(12):122006, 2014. doi: 10.1103/PhysRevD.90.122006.

[18] J. Abraham et al. Properties and performance of the prototype instrument for the Pierre Auger Observatory. *Nucl. Instrum. Meth. A*, 523:50–95, 2004. doi: 10.1016/j.nima.2003.12.012.

[19] J. Bellido. Depth of maximum of air-shower profiles at the Pierre Auger Observatory: Measurements above $10^{17.2}$ eV and Composition Implications. *PoS*, ICRC2017:506, 2018. doi: 10.22323/1.301.0506.

[20] A. Aab et al. Measurement of the Fluctuations in the Number of Muons in Extensive Air Showers with the Pierre Auger Observatory. *Phys. Rev. Lett.*, 126(15):152002, 2021. doi: 10.1103/PhysRevLett.126.152002.

[21] S. Andringa, R. Conceicao, and M. Pimenta. Mass composition and cross-section from the shape of cosmic ray shower longitudinal profiles. *Astropart. Phys.*, 34:360–367, 2011. doi: 10.1016/j.astropartphys.2010.10.002.

[22] T. Gaisser and A. M. Hillas. Reliability of the method of constant intensity cuts for reconstructing the average development of vertical showers. In *Proc. 15th ICRC **8** 353*, 1977.

[23] A. Aab et al. Measurement of the average shape of longitudinal profiles of cosmic-ray air showers at the Pierre Auger Observatory. *JCAP*, 03:018, 2019. doi: 10.1088/1475-7516/2019/03/018.

[24] R. Conceição, S. Andringa, F. Diogo, and M. Pimenta. The average longitudinal air shower profile: exploring the shape information. *J. Phys. Conf. Ser.*, 632(1):012087, 2015. doi: 10.1088/1742-6596/632/1/012087.

[25] J. A. J. Matthews, R. Mesler, B. R. Becker, M. S. Gold, and J. D. Hague. A Parametrization of Cosmic Ray Shower Profiles Based on Shower Width. *J. Phys. G*, 37:025202, 2010. doi: 10.1088/0954-3899/37/2/025202.

[26] A. Aab et al. Muons in Air Showers at the Pierre Auger Observatory: Measurement of Atmospheric Production Depth. *Phys. Rev. D*, 90(1):012012, 2014. doi: 10.1103/PhysRevD.90.012012. [Addendum: Phys.Rev.D 90, 039904 (2014), Erratum: Phys.Rev.D 92, 019903 (2015)].

[27] T. Abu-Zayyad et al. Evidence for Changing of Cosmic Ray Composition between 10**17-eV and 10**18-eV from Multicomponent Measurements. *Phys. Rev. Lett.*, 84:4276–4279, 2000. doi: 10.1103/PhysRevLett.84.4276.

[28] A. G. Bogdanov, D. M. Gromushkin, R. P. Kokoulin, G. Mannocchi, A. A. Petrukhin, O. Saavedra, G. Trinchero, D. V. Chernov, V. V. Shutenko, and I. I. Yashin. Investigation of the properties of the flux and interaction of ultrahigh-energy cosmic rays by the method of local-muon-density spectra. *Phys. Atom. Nucl.*, 73:1852–1869, 2010. doi: 10.1134/S1063778810110074.

[29] A. G. Bogdanov, R. P. Kokoulin, G. Mannocchi, A. A. Petrukhin, O. Saavedra, V. V. Shutenko, G. Trinchero, and I. I. Yashin. Investigation of very high energy cosmic rays by means of inclined muon bundles. *Astropart. Phys.*, 98:13–20, 2018. doi: 10.1016/j.astropartphys.2018.01.003.

[30] W. D. Apel et al. Probing the evolution of the EAS muon content in the atmosphere with KASCADE-Grande. *Astropart. Phys.*, 95:25–43, 2017. doi: 10.1016/j.astropartphys.2017.07.001.

[31] L. Cazon. Working Group Report on the Combined Analysis of Muon Density Measurements from Eight Air Shower Experiments. *PoS*, ICRC2019:214, 2020. doi: 10.22323/1.358.0214.

[32] J. G. Gonzalez. Measuring the Muon Content of Air Showers with IceTop. *EPJ Web Conf.*, 99: 06002, 2015. doi: 10.1051/epjconf/20159906002.

[33] J. A. Bellido, R. W. Clay, N. N. Kalmykov, I. S. Karpikov, G. I. Rubtsov, S. V. Troitsky, and J. Ulrichs. Muon content of extensive air showers: comparison of the energy spectra obtained by the Sydney University Giant Air-shower Recorder and by the Pierre Auger Observatory. *Phys. Rev. D*, 98(2): 023014, 2018. doi: 10.1103/PhysRevD.98.023014.

[34] A. Aab et al. Direct measurement of the muonic content of extensive air showers between $\mathbf{2 \times 10^{17}}$ and $\mathbf{2 \times 10^{18}}$ eV at the Pierre Auger Observatory. *Eur. Phys. J. C*, 80(8):751, 2020. doi: 10.1140/epjc/s10052-020-8055-y.

[35] A. Aab et al. Direct measurement of the muonic content of extensive air showers between $\mathbf{2 \times 10^{17}}$ and $\mathbf{2 \times 10^{18}}$ eV at the Pierre Auger Observatory. *Eur. Phys. J. C*, 80(8):751, 2020. doi: 10.1140/epjc/s10052-020-8055-y.

[36] R. U. Abbasi et al. Study of muons from ultrahigh energy cosmic ray air showers measured with the Telescope Array experiment. *Phys. Rev. D*, 98(2):022002, 2018. doi: 10.1103/PhysRevD.98.022002.

[37] H. P. Dembinski et al. Report on Tests and Measurements of Hadronic Interaction Properties with Air Showers. *EPJ Web Conf.*, 210:02004, 2019. doi: 10.1051/epjconf/201921002004.

[38] G. R. Farrar and J. D. Allen. A new physical phenomenon in ultra-high energy collisions. *EPJ Web Conf.*, 53:07007, 2013. doi: 10.1051/epjconf/20135307007.

[39] J. R. Horandel. On total inelastic cross-sections and the average depth of the maximum of extensive air showers. *J. Phys. G*, 29:2439–2464, 2003. doi: 10.1088/0954-3899/29/11/001.

[40] A. Capella, U. Sukhatme, C.-I. Tan, and J. Tran Thanh Van. Dual parton model. *Phys. Rept.*, 236: 225–329, 1994. doi: 10.1016/0370-1573(94)90064-7.

[41] M. A. Braun and C. Pajares. Implications of percolation of color strings on multiplicities, correlations and the transverse momentum. *Eur. Phys. J. C*, 16:349–359, 2000. doi: 10.1007/s100520050027.

[42] M. A. Braun and C. Pajares. Transverse momentum distributions and their forward backward correlations in the percolating color string approach. *Phys. Rev. Lett.*, 85:4864–4867, 2000. doi: 10.1103/PhysRevLett.85.4864.

[43] J. Alvarez-Muniz, L. Cazon, R. Conceicao, J. D. de Deus, C. Pajares, and M. Pimenta. Muon production and string percolation effects in cosmic rays at the highest energies. 9 2012.

[44] T. Pierog and K. Werner. Muon Production in Extended Air Shower Simulations. *Phys. Rev. Lett.*, 101:171101, 2008. doi: 10.1103/PhysRevLett.101.171101.

[45] D. LaHurd and C. E. Covault. Exploring Potential Signatures of QGP in UHECR Ground Profiles. *JCAP*, 11:007, 2018. doi: 10.1088/1475-7516/2018/11/007.

[46] L. Apolinário, Y.-J. Lee, and M. Winn. Heavy quarks and jets as probes of the QGP. 3 2022. doi: 10.1016/j.ppnp.2022.103990.

[47] W. Busza, K. Rajagopal, and W. van der Schee. Heavy Ion Collisions: The Big Picture, and the Big Questions. *Ann. Rev. Nucl. Part. Sci.*, 68:339–376, 2018. doi: 10.1146/annurev-nucl-101917-020852.

[48] I. Arsene et al. Quark gluon plasma and color glass condensate at RHIC? The Perspective from the BRAHMS experiment. *Nucl. Phys. A*, 757:1–27, 2005. doi: 10.1016/j.nuclphysa.2005.02.130.

[49] B. B. Back et al. The PHOBOS perspective on discoveries at RHIC. *Nucl. Phys. A*, 757:28–101, 2005. doi: 10.1016/j.nuclphysa.2005.03.084.

[50] J. Adams et al. Experimental and theoretical challenges in the search for the quark gluon plasma: The STAR Collaboration's critical assessment of the evidence from RHIC collisions. *Nucl. Phys. A*, 757:102–183, 2005. doi: 10.1016/j.nuclphysa.2005.03.085.

[51] K. Adcox et al. Formation of dense partonic matter in relativistic nucleus-nucleus collisions at RHIC: Experimental evaluation by the PHENIX collaboration. *Nucl. Phys. A*, 757:184–283, 2005. doi: 10.1016/j.nuclphysa.2005.03.086.

[52] N. Armesto and E. Scomparin. Heavy-ion collisions at the Large Hadron Collider: a review of the results from Run 1. *Eur. Phys. J. Plus*, 131(3):52, 2016. doi: 10.1140/epjp/i2016-16052-4.

[53] P. Foka and M. A. Janik. An overview of experimental results from ultra-relativistic heavy-ion collisions at the CERN LHC: Hard probes. *Rev. Phys.*, 1:172–194, 2016. doi: 10.1016/j.revip.2016.11.001.

[54] P. Foka and M. A. Janik. An overview of experimental results from ultra-relativistic heavy-ion collisions at the CERN LHC: Bulk properties and dynamical evolution. *Rev. Phys.*, 1:154–171, 2016. doi: 10.1016/j.revip.2016.11.002.

[55] R. Bala, I. Bautista, J. Bielcikova, and A. Ortiz. Heavy-ion physics at the LHC: Review of Run I results. *Int. J. Mod. Phys. E*, 25(07):1642006, 2016. doi: 10.1142/S0218301316420064.

[56] M. E. Tejeda-Yeomans. Heavy-ion physics: freedom to do hot, dense, exciting QCD. *CERN Yellow Rep. School Proc.*, 2:137, 2021. doi: 10.23730/CYRSP-2021-002.137.

[57] M. L. Miller, K. Reygers, S. J. Sanders, and P. Steinberg. Glauber modeling in high energy nuclear collisions. *Ann. Rev. Nucl. Part. Sci.*, 57:205–243, 2007. doi: 10.1146/annurev.nucl.57.090506.123020.

[58] The ALICE experiment - A journey through QCD. 11 2022.

[59] D. Enstrom. Astrophysical aspects of quark gluon plasma. Other thesis, 2 1998.

[60] J. Adam et al. Enhanced production of multi-strange hadrons in high-multiplicity proton-proton collisions. *Nature Phys.*, 13:535–539, 2017. doi: 10.1038/nphys4111.

[61] B. Müller. Diagnosing the Quark-Gluon Plasma. 6 2021.

[62] F. Becattini and J. Manninen. Strangeness production from SPS to LHC. *J. Phys. G*, 35:104013, 2008. doi: 10.1088/0954-3899/35/10/104013.

[63] S. Baur, H. Dembinski, M. Perlin, T. Pierog, R. Ulrich, and K. Werner. Core-corona effect in hadron collisions and muon production in air showers. 2 2019.

[64] S. Acharya et al. Multiplicity dependence of π, K, and p production in pp collisions at $\sqrt{s} = 13$ TeV. *Eur. Phys. J. C*, 80(8):693, 2020. doi: 10.1140/epjc/s10052-020-8125-1.

[65] W. van der Schee, P. Romatschke, and S. Pratt. Fully Dynamical Simulation of Central Nuclear Collisions. *Phys. Rev. Lett.*, 111(22):222302, 2013. doi: 10.1103/PhysRevLett.111.222302.

[66] K. H. Ackermann et al. Elliptic flow in Au + Au collisions at (S(NN))**(1/2) = 130 GeV. *Phys. Rev. Lett.*, 86:402–407, 2001. doi: 10.1103/PhysRevLett.86.402.

[67] J. L. Nagle and W. A. Zajc. Small System Collectivity in Relativistic Hadronic and Nuclear Collisions. *Ann. Rev. Nucl. Part. Sci.*, 68:211–235, 2018. doi: 10.1146/annurev-nucl-101916-123209.

[68] S. Chatrchyan et al. Jet momentum dependence of jet quenching in PbPb collisions at $\sqrt{s_{NN}} = 2.76$ TeV. *Phys. Lett. B*, 712:176–197, 2012. doi: 10.1016/j.physletb.2012.04.058.

[69] K. Adcox et al. Suppression of hadrons with large transverse momentum in central Au+Au collisions at $\sqrt{s_{NN}}$ = 130-GeV. *Phys. Rev. Lett.*, 88:022301, 2002. doi: 10.1103/PhysRevLett.88.022301.

[70] C. Adler et al. Centrality dependence of high p_T hadron suppression in Au+Au collisions at $\sqrt{s}_{NN}$ = 130-GeV. *Phys. Rev. Lett.*, 89:202301, 2002. doi: 10.1103/PhysRevLett.89.202301.

[71] K. Aamodt et al. Suppression of Charged Particle Production at Large Transverse Momentum in Central Pb-Pb Collisions at $\sqrt{s_{NN}} = 2.76$ TeV. *Phys. Lett. B*, 696:30–39, 2011. doi: 10.1016/j.physletb.2010.12.020.

[72] B. Abelev et al. Centrality Dependence of Charged Particle Production at Large Transverse Momentum in Pb–Pb Collisions at $\sqrt{s_{\mathrm{NN}}} = 2.76$ TeV. *Phys. Lett. B*, 720:52–62, 2013. doi: 10.1016/j.physletb.2013.01.051.

[73] S. Chatrchyan et al. Study of high-pT charged particle suppression in PbPb compared to pp collisions at $\sqrt{s_{NN}} = 2.76$ TeV. *Eur. Phys. J. C*, 72:1945, 2012. doi: 10.1140/epjc/s10052-012-1945-x.

[74] G. Aad et al. Measurement of charged-particle spectra in Pb+Pb collisions at $\sqrt{s_{\mathrm{NN}}} = 2.76$ TeV with the ATLAS detector at the LHC. *JHEP*, 09:050, 2015. doi: 10.1007/JHEP09(2015)050.

[75] S. Acharya et al. Transverse momentum spectra and nuclear modification factors of charged particles in pp, p-Pb and Pb-Pb collisions at the LHC. *JHEP*, 11:013, 2018. doi: 10.1007/JHEP11(2018)013.

[76] P. Bozek and W. Broniowski. Collective dynamics in high-energy proton-nucleus collisions. *Phys. Rev. C*, 88(1):014903, 2013. doi: 10.1103/PhysRevC.88.014903.

[77] W. Busza. Structure and fine structure in multiparticle production data at high energies. *Acta Phys. Polon. B*, 35:2873–2894, 2004.

[78] J. Adam et al. Multiplicity dependence of charged pion, kaon, and (anti)proton production at large transverse momentum in p-Pb collisions at $\sqrt{s_{\mathrm{NN}}}$ = 5.02 TeV. *Phys. Lett. B*, 760:720–735, 2016. doi: 10.1016/j.physletb.2016.07.050.

[79] M. Aaboud et al. Measurements of long-range azimuthal anisotropies and associated Fourier coefficients for pp collisions at $\sqrt{s} = 5.02$ and 13 TeV and p+Pb collisions at $\sqrt{s_{\mathrm{NN}}} = 5.02$ TeV with the ATLAS detector. *Phys. Rev. C*, 96(2):024908, 2017. doi: 10.1103/PhysRevC.96.024908.

[80] P. M. Chesler. Colliding shock waves and hydrodynamics in small systems. *Phys. Rev. Lett.*, 115 (24):241602, 2015. doi: 10.1103/PhysRevLett.115.241602.

[81] M. D. Sievert and J. Noronha-Hostler. CERN Large Hadron Collider system size scan predictions for PbPb, XeXe, ArAr, and OO with relativistic hydrodynamics. *Phys. Rev. C*, 100(2):024904, 2019. doi: 10.1103/PhysRevC.100.024904.

[82] S. Chatrchyan et al. Observation of Long-Range Near-Side Angular Correlations in Proton-Lead Collisions at the LHC. *Phys. Lett. B*, 718:795–814, 2013. doi: 10.1016/j.physletb.2012.11.025.

[83] V. Khachatryan et al. Evidence for Collective Multiparticle Correlations in p-Pb Collisions. *Phys. Rev. Lett.*, 115(1):012301, 2015. doi: 10.1103/PhysRevLett.115.012301.

[84] A. Adare et al. Measurements of elliptic and triangular flow in high-multiplicity ^{3}He+Au collisions at $\sqrt{s_{_{NN}}} = 200$ GeV. *Phys. Rev. Lett.*, 115(14):142301, 2015. doi: 10.1103/PhysRevLett.115.142301.

[85] L. A. Anchordoqui, H. Goldberg, and T. J. Weiler. Strange fireball as an explanation of the muon excess in Auger data. *Phys. Rev. D*, 95(6):063005, 2017. doi: 10.1103/PhysRevD.95.063005.

[86] D. d'Enterria, R. Engel, T. McCauley, and T. Pierog. Cosmic-ray Monte Carlo predictions for forward particle production in p-p, p-Pb, and Pb-Pb collisions at the LHC. *Indian J. Phys.*, 84:1837–1842, 2010. doi: 10.1007/s12648-010-0182-0.

[87] T. Pierog, I. Karpenko, J. M. Katzy, E. Yatsenko, and K. Werner. EPOS LHC: Test of collective hadronization with data measured at the CERN Large Hadron Collider. *Phys. Rev. C*, 92(3):034906, 2015. doi: 10.1103/PhysRevC.92.034906.

[88] S. Ostapchenko. QGSJET-II: physics, recent improvements, and results for air showers. *EPJ Web Conf.*, 52:02001, 2013. doi: 10.1051/epjconf/20125202001.

[89] F. Riehn, H. P. Dembinski, R. Engel, A. Fedynitch, T. K. Gaisser, and T. Stanev. The hadronic interaction model SIBYLL 2.3c and Feynman scaling. *PoS*, ICRC2017:301, 2018. doi: 10.22323/1.301.0301.

[90] T. Bergmann, R. Engel, D. Heck, N. N. Kalmykov, S. Ostapchenko, T. Pierog, T. Thouw, and K. Werner. One-dimensional Hybrid Approach to Extensive Air Shower Simulation. *Astropart. Phys.*, 26:420–432, 2007. doi: 10.1016/j.astropartphys.2006.08.005.

[91] T. Pierog et al. First results of fast one-dimensional hybrid simulation of EAS using CONEX. *Nucl. Phys. B Proc. Suppl.*, 151:159–162, 2006. doi: 10.1016/j.nuclphysbps.2005.07.029.

[92] T. Pierog. Modelling hadronic interactions in cosmic ray Monte Carlo generators. *EPJ Web Conf.*, 99:09002, 2015. doi: 10.1051/epjconf/20159909002.

[93] V. N. Gribov. A reggeon diagram technique. *Sov. Phys. JETP*, 26:414–422, 1968.

[94] K. Werner, A. G. Knospe, C. Markert, B. Guiot, I. Karpenko, T. Pierog, G. Sophys, M. Stefaniak, M. Bleicher, and J. Steinheimer. Resonance production in high energy collisions from small to big systems. *EPJ Web Conf.*, 171:09002, 2018. doi: 10.1051/epjconf/201817109002.

[95] M. Perlin. *Core-corona hadronization model and its impact on muon content of extensive air showers*. PhD thesis, KIT, Karlsruhe, Karlsruher Institut für Technologie, KIT, Karlsruhe, IAP, 2022.

[96] R. Ulrich, J. Blumer, R. Engel, F. Schussler, and M. Unger. On the measurement of the proton-air cross section using air shower data. *New J. Phys.*, 11:065018, 2009. doi: 10.1088/1367-2630/11/6/065018.

[97] R. Ulrich, R. Engel, S. Muller, F. Schussler, and M. Unger. Proton-Air Cross Section and Extensive Air Showers. *Nucl. Phys. B Proc. Suppl.*, 196:335–340, 2009. doi: 10.1016/j.nuclphysbps.2009.09.064.

[98] L. Cazon, R. Conceição, and F. Riehn. Probing the energy spectrum of hadrons in proton air interactions at ultrahigh energies through the fluctuations of the muon content of extensive air showers. *Phys. Lett. B*, 784:68–76, 2018. doi: 10.1016/j.physletb.2018.07.026.